Adipic Acid Sonocrystallization in Continuous Flow Microchannels

Damiano Rossi

Department of Chemical Engineering
University College London

A thesis submitted for the degree of
Doctor of Philosophy of University College London

I, Damiano Rossi, confirm that the work presented in this thesis is my own. Where information has been derived from other sources, I confirm that this has been indicated in the thesis.

Signature

Date

Abstract

Crystallization is widely employed in the manufacture of pharmaceuticals during the intermediate and final stages of purification and separation. The process defines drug chemical purity and physical properties: crystal morphology, size distribution, habit and degree of perfection. Particulate pharmaceuticals are typically manufactured in conventional batch stirred tank crystallizers that are still inadequate with regard to process controllability and reproducibility of the final crystalline product. Variations in crystal characteristics are responsible for a wide range of pharmaceutical formulation problems, related for instance to bioavailability and the chemical and physical stability of drugs in their final dosage forms.

This thesis explores the design of a novel crystallization approach which combines in an integrated unit continuous flow, microreactor technology, and ultrasound engineering. By exploiting the various benefits deriving from each technology, the thesis focuses on the experimental characterization of two different nucleation systems: a droplet-based system and a single-phase system. In the former, channel fouling is avoided using a carrier fluid to segment the crystallizing solution in droplets, thus avoiding the contact with the walls. In the latter channel blockage is prevented using larger channel geometries and employing higher flow rates. The flexibility of the developed setup also allows performing stochastic nucleation studies to estimate the nucleation kinetics under silent and sonicated conditions.

The experiments reveal that very high nucleation rates, small crystal sizes, narrow size distributions and high crystal yields can be obtained with both setups when the crystallizing solution is exposed to high pressure field as compared to silent condition. It is concluded that transient cavitation of bubbles and its consequences are a significant mechanism for enhancing nucleation of crystals among several proposed in the literature.

A preliminary study towards the development and design of a growth stage is finally performed. Flow pulsation is identified as a potential method to enhance radial mixing and narrow residence time distribution therefore achieving optimal conditions for uniform crystal growth. The results suggest that increasing values of Strouhal number as well as amplitude ratio improve axial dispersion. Helically coiled tubes are identified as potential structures to further improve fluid dynamic dispersion.

Table of contents

Figure List

Table List

1. General introduction

In this chapter, we give a brief introduction to the research work background together with the project overview, we summarize the main objectives of this work and we present an outline of the thesis.

1.1 Research background

Crystallization is the oldest separation process within chemical engineering that involves the formation of an ordered solid phase (crystals) from a homogeneous gas, liquid or amorphous phase. The low level of energy consumption and the relatively mild process conditions make crystallization more attractive than other traditional separation processes for the production and purification or recovery of solid materials[1]. For this reason, crystallization is particularly employed in the manufacture of pharmaceuticals and over 90% of all active pharmaceutical ingredients (API) contain drugs usually in crystalline form[2].

The development of the crystallization process plays a crucial role in defining the stability and drug release properties of the final dosage forms. As a result, process controllability becomes an important factor to be addressed in order to achieve the following conditions[3]:

1) Sufficient product purity and high quality standards.
2) Isolation of the particular polymorphic crystal form, which is typically the most thermodynamically stable.
3) A specific target of crystal size distribution (CSD), crystal mean size and crystal habit that affect both bioavailability and processability.
4) A high yield and a high volume productivity with a final slurry concentration generally target around 5 - 10 wt %.
5) A reasonable cycle time (generally 24 h) for the crystallization, as well as for the associated filtration and drying processes.

The first three points are absolutely critical as their achievement ensures drug's efficacy and patient safety, while the last two are more important for the control of the operating costs. Unfortunately, these factors are not independent, and achieving one may render it impossible to achieve the others. In fact, crystallization is a very complex process involving, multi-phases equilibrium, polymorphism transformation and nucleation and growth kinetics that are difficult to quantify. This makes the prediction, design and control of crystallization processes very challenging.

Due to the relatively low quantity produced, pharmaceuticals are normally manufactured batchwise either as a cooling, antisolvent, or reactive crystallization in short campaigns using crystallizers that are typically standard agitated vessels. Moreover, the advantages of batch crystallization over continuous crystallization make the former still the most common crystallization process adopted in the chemical industry[4]. Major challenges still persist, however, in conventional batch stirred tank crystallizers with regard to process controllability and reproducibility, owing to the rapidity of the involved processes of mixing, nucleation, growth and agglomeration and their complex interactions when they take place concurrently. Often nucleation is rapid compared with mixing and starts when the components are still inhomogeneously distributed, resulting in broad crystal size distributions and substantial batch-to-batch product variability[5]. Continuous flow reactors offer a technology with the potential to form particles with excellent homogeneity and control the critical process parameters in a way that is difficult to achieve in batch reactors. Owing to the continuous nature of the process and better controlled fluid dynamic conditions, these systems offer improved controllability and reproducibility and therefore a precise control over the particle size, shape and crystallinity[2].

Intentional seeding is a common technique used in industrial crystallization processes as a method to control the CSD, narrowing the metastable zone width and shortening the induction times. Such technique requires operator intervention which entails additional engineering to control the seed addition. If the seeds are added immediately after the desired supersaturation is reached, they will dissolve with no effect, while if they are added too late, they will not be able to influence the crystallization process, since the high supersaturation levels will have rendered it poorly controllable. Post-crystallization processes such as milling, crushing and grinding can be alternatively used to control the desired CSD and crystal mean size. Unfortunately these methods compromise the stability and properties of the drug material reducing the quality of the final product[1,5]. Sonication, the application of power ultrasound to process fluids, is an intensification technology that, when applied to crystallization, permits to significantly tailor and improve both process and product quality[6,7]. The additional degrees of freedom that ultrasound introduces render the process more flexible, offering the potential to selectively promote the different processes of crystallization (nucleation, growth, etc.). This technology is called sonocrystallization (SC) and has been rapidly developed over the last 20 years. It has been reported that crystallization assisted by ultrasound presents lower induction times, higher nucleation and growth rates also improving crystal habit and crystal size distribution[8,9,10,11,12,13,14]. Furthermore, ultrasound is an interesting method in selecting a specific desired polymorphic form[15]. A relevant advantage offered by the application of ultrasound combined with crystallization is that seeding is no longer needed to induce primary nucleation, because sonication attains the same result more effectively and with better control[16,17,18]. This is particularly welcome in pharmaceutical processes. Ultrasound generators operate remotely and therefore are suitable for contained, sterile environments. Issues such as seeds choice and contamination are eliminated. Moreover, the supersaturation level where nucleation should be induced can be easily controlled at the flick of a switch. Finally, the use of ultrasound is also expected to overcome problems associated with channel clogging and the pumping of suspensions. This has been demonstrated for the flow of particle suspensions in small channel heat exchangers, where fouling is drastically reduced in the presence of ultrasound[19,20]. *Cavitation* occurring during the ultrasonic irradiation is commonly regarded as the principal mechanism that promotes crystal nucleation[21,22]. However, the link between the two phenomena is still a subject of research, and various mechanisms have been proposed[23,24,25,26].

The past two decades have seen a remarkable progress in the development and fabrication of microfluidic systems for use in the chemical and biological sciences[27,28]. Nowadays, microfluidics offers a wide range of new tools that can be employed into crystallization study, particularly for the screening of crystallization mechanisms, as well as for investigating crystal nucleation kinetics. In fact, in specific channels geometries, a two-phase flow can produce monodisperse droplets that can be stored under static conditions and observed in order to get nucleation statistics and crystal growth rates[29,30]. Microfluidic reactor technology is also adopted in the production of micro and nanoparticles. Smaller characteristic lengths and greater surface-to-volume ratios intensify mass and heat transfer, leading to much higher efficiencies than in batch reactors. Operation temperatures can be precisely manipulated, improving control of the nucleation stage for cooling or high temperature reactive crystallization; for antisolvent crystallization, the fast and well controlled mixing conditions can have a similar impact. Scale-up by increasing the number of units instead of their size (numbering up) can be implemented to increase throughput. Despite the various advantages, channel clogging is still the main issue to be addressed when dealing with particles in narrow channel and preventing the synthesized particles or crystals from adhering to the microchannel walls and blocking the reactor is still a subject of research[31,32].

In conclusion we identified three different strategies (continuous flow crystallization, microfluidics and ultrasound technology) which offer an opportunity to further enhance the crystallization performance. Their use allows one to increase product quality, consistency of product characteristics, controllability and reproducibility of the crystallization process.

1.2 Overall aim of the sonocrystallization project

The present work is part of a broader multidisciplinary study that aims to develop a novel system for crystal production of relevance to the pharmaceutical industries. The overall aim is to combine continuous flow processing, in microchannel devices with sonication technologies for addressing key challenges in pharmaceuticals manufacture. Continuous processes can lead to higher reproducibility so that the various crystallization stages can be controlled separately. Small dimensions of microfluidic devices offer better mixing and improved temperature and concentration control leading to narrower crystal size distributions than large stirred tank crystallizer. Finally, ultrasound reduces the mean crystal size also narrowing the crystal size distribution. The application of ultrasound reduces considerably the induction times triggering nucleation as soon as the desired supersaturation is reached. This allows a greater control of the crystallization process.

Figure 1.1 gives a brief overview of the sonocrystallization process to be designed for the continuous production of crystals.

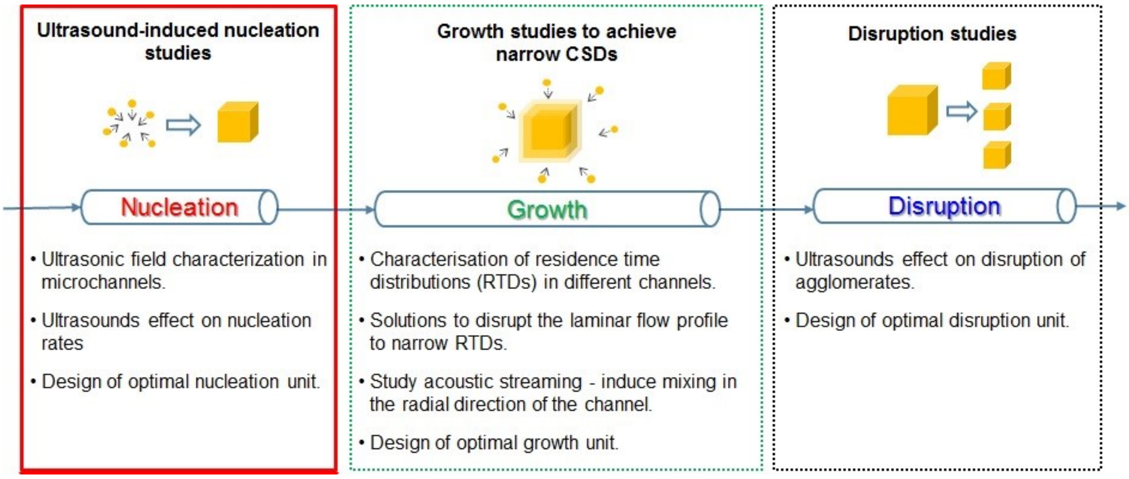

Figure 1.1. Sonocrystallization process overview.

Since the process is no longer restricted to a single unit, it offers the possibility to decouple its various stages and to select for each one the optimal operating conditions. The first and most important step in the crystallization process is *nucleation* which is the formation of stable nuclei that successively can grow into crystals. The use of sonication will allow separation of the nucleation unit in two sections. The first is a supersaturator, designed to achieve the necessary supersaturation, and the second the nucleation initiation unit, where ultrasound will be used to induce nucleation. Crystal growth is another key part of the synthesis process that strongly affects the end product crystal size distribution. Here the aim is narrowing the CSD as much as possible about the desired mean crystal size. To achieve this, we must let the nuclei grow under similar fluid dynamic conditions for similar times. The supersaturation and concentration gradients around the nuclei must be similar, while the residence time distribution (RTD) of the growth unit must be narrow. It would be ideal if agglomeration can be avoided or minimized, but if this is not the case, a crystal disruption section can help to obtain a narrow CSD. Ultrasound has been reported to break aggregated and agglomerated crystals through mechanical effects.

The three main stages of the sonocrystallization process are studied separately. For each unit particular challenges and objectives are identified and addressed. After studying all the subunits, we will integrate them in a complete system. This will contain the nucleation, growth and disruption subunits, which will have separate optimized sonication assemblies, as well as separate controls for temperature. The current thesis will be mainly focused on the study and design of the first stage (nucleation unit). The development and design of the other units will be carried out by separate team of researchers working at the same sonocrystallization project.

We select adipic acid (AA) *cooling crystallization* as model system. Adipic acid is the adopted compound for this study due the physicochemical data available in the literature and the presence of similar sonocrystallization analysis developed in larger crystallizers[1,9,33]. Adipic acid primary application is in the production of nylon 66 polyamide but it also has many other commercial uses such as excipient in drugs and in food industry as flavoring and pH control agent[34].

1.3 Thesis objectives

In this work we focus mainly on the nucleation stage, which is the first step of the entire sonocrystallization process presented in Figure 1.1. In this regard, the specific objectives of the proposed research are:

- To design improved nucleation unit by combining continuous flow, small channel reactor technology and ultrasound engineering.
- To advance the knowledge of the nucleation mechanisms by studying the sonication phenomena affecting the nucleation process.
- To study the production rate and the crystal size distributions of the crystals generated by the developed nucleation unit.
- To compare the nucleation rate of the sonicated nucleation unit with the nucleation rate measured in silent conditions.
- To develop a preliminary design of the growth stage.

1.4 Thesis outline

Following this introduction, in Chapter 2 we give an extensive description of the three main technologies that we aim to combine in order to design the nucleation unit. To this end, after presenting the fundamental theory of crystallization, we discuss continuous flow crystallization, microfluidics and power ultrasound technologies. Particular attention is given to the description of the Classical Nucleation Theory (CNT) and the stochastic approach to measure nucleation rates resorting to droplet-based methods.

Chapter 3 describes the materials examined and details of analytical techniques utilized in this research project.

In Chapter 4, we present a novel and flexible droplet-based microfluidic approach that allows performing nucleation studies under different silent fluid dynamic conditions. Adipic acid primary nucleation rates and nucleation kinetic parameters are determined by using liquid/liquid segmented flow in capillary tubes in which the crystallizing medium is partitioned into small droplets. We do so by measuring the probability of crystal presence within individual droplets. The results of silent conditions are useful for comparison with the ones obtained with the following sonicated setups to measure the improvement of the crystallization performance.

The first design of a continuous flow nucleation unit is presented and investigated experimentally in chapter 5. We present a successful anti-clogging technique which involves performing sonocrystallization in droplets that travel through the microchannel inside a carrier phase. The effect of supersaturation and ultrasound power on crystal size distribution and crystal production is studied. To elucidate the relationship between crystallization and cavitation, sonochemiluminescence and sonoemulsification experiments are performed and numerical investigation of the wave propagation in aqueous solution is used to predict the probability of cavitation.

In chapter 6, we present a second continuous flow sonocrystallizer in which the carrier phase is removed. To avoid the problem of channel occlusion, large capillary diameters are employed. The system is studied experimentally. We investigate the time during which the crystallizing solution is exposed to ultrasound on crystal size distribution and crystal production.

In chapter 7, we focus on the growth stage which is the second fundamental step of the sonocrystallization process. In this regard, we represent a preliminary study towards the development and design of the growth stage in which flow pulsation is employed to reduce axial dispersion and improve residence time distribution. Helically coiled tube structures are identified as high-performance and compact systems to reduce axial dispersion for continuous processes involving particle formation and particle growth.

A list of references and publications is included at the end of the thesis.

2. Literature review

In this chapter, we introduce the fundamental theory of crystallization with a particular attention to nucleation and we discuss the principal technologies that are employed in the design of the nucleation unit: continuous flow crystallization, microfluidics and power ultrasound.

2.1 Fundamental theory of crystallization

The process of phase transformation and the resulting creation of crystalline materials from liquid-phase precursors are central to the science and process engineering of materials. The outcome of synthetic procedures for crystalline organic materials strongly depends on the first steps along the molecular self-assembly pathway, a process we know as crystal nucleation. In this thesis the attention is focused on the nucleation part that represents the first crucial step of crystallization where the solute molecules dispersed in the solvent start to gather into clusters arranging themselves in a pattern characteristic of a crystalline solid. Nucleation is followed by crystal growth which is the second stage of a crystallization process, and consists in the addition of new molecules into the characteristic arrangement of a crystalline lattice that reaches a macroscopic size. Finally, crystal agglomeration and crystal disruption can also occur during the crystallization process. This happens particularly in agitated vessels where high mixing conditions and shear forces generate particle collisions and particle breakup, therefore affecting the final particle size distributions.

The current knowledge relating to molecular self-assembly in nucleating systems is still unclear and different theories have been proposed in the last decades to describe the nucleation mechanism[35]. Nowadays, the *Classical Nucleation Theory (CNT)* developed by Gibbs, Volmer, Weber, Becker, Döring, Turnbull and Fishers is the most widely accepted theory to model the nucleating systems and quantify their kinetics. Therefore, in this work we decide to adopt the CNT to characterize the performance of the nucleation stage designed. To this end, the following paragraphs are dedicated to review in details the CNT and its implementation. The thermodynamics of the process is considered and expressions are given for the supersaturation, the nucleation rate, the nucleation work and the size of the nucleus in homogeneous and heterogeneous nucleation. Finally, we give a brief overview on crystal growth, crystal breakage and crystal agglomeration.

2.1.1 Classical nucleation theory (CNT)

To describe nucleation we refer to the simple binary solution system, i.e. a single-component (solute) dissolved in a liquid solution which is also the case of study of the present research. With some modification, the Classical Nucleation Theory is also applicable to all the other phase change processes such as gas bubbles formation or melting and can be extended to multi-component systems as well[36].

Molecules of solute move randomly in the solution and hit each other, presumably inelastically. This process is described as the fluctuational appearance of nanoscopically small molecular clusters of the new crystalline phase. The dimension of a cluster can be characterized by the number n of molecules constituting the cluster. To form a cluster of size n where n = 1,2,3,… a specific work $W(n)$ is therefore required. The work $W(n)$ associated with an n-sized cluster formation is thermodynamically defined as the difference between the free energy of the system in its final and initial states, i.e. after and before the cluster appearance. To write an expression for $W(n)$ we need to consider that a cluster n experiences two main forces, they are volume force and surface force. Volume force is a cohesion force which tends to maintain the cluster by keeping all its n molecules assembled together. This force depends on the number of shared bonds between molecules inside the volume of the cluster. By contrast, surface force is an opposite force that depends on the number of unshared extra-molecular bonds (facing towards solution), free surface of cluster in contact with the ambient solution, and tends to break the cluster up. Thus, $W(n)$ is composed by a "negative" volume term and a positive "surface" term as follows[37]:

$$W(n) = -W_V(n) + W_S(n) \qquad \text{Eq. 2.1}$$

where $W_V(n)$ accounts for the free energy gain related to the cluster volume and $W_S(n)$ for the free energy loss due to the creation of an interface between the cluster and the medium. The volume term $W_V(n)$ is expressed as the difference between the chemical potentials of a molecule in the solution (μ_S), and in the bulk of solid crystal phase (μ_C):

$$W_V(n) = -n(\mu_S - \mu_C) = -n\Delta\mu \qquad \text{Eq. 2.2}$$

Using the expressions for μ_S and μ_C at constant pressure, one can write $\Delta\mu$ in the form:

$$\Delta\mu = KTlnS \qquad \text{Eq. 2.3}$$

where K is the Boltzmann constant $(1.38 \cdot 10^{-20}\ \mathrm{mJK^{-1}})$, T the absolute temperature and S the *supersaturation* defined as:

$$S = a/a_e \qquad \text{Eq. 2.4}$$

where a and a_e are the actual and the equilibrium activities of molecules in solution, respectively. For sufficiently dilute solutions the activity terms can be replaced by the actual and equilibrium concentrations of molecules in solution C $(\mathrm{m^{-3}})$ and C_e $(\mathrm{m^{-3}})$:

$$S = C/C_e \qquad \text{Eq. 2.5}$$

C_e is also known as *solubility* and is a function of the solution temperature T. Nucleation is thermodynamically possible only if $\Delta\mu > 0$. According to Eq. 2.3, this condition corresponds to S >1 where the solution is defined as supersaturated. Similarly, $\Delta\mu = 0$ and $\Delta\mu < 0$ correspond to the equilibrium and undersaturated conditions that can be translated as S =1 and $S < 1$, respectively. To conclude, supersaturation is the driving force of the nucleation process and a supersaturation S larger than one is required to nucleate.

The definition of the surface energy term $W_S(n)$ in Eq. 2.1 is one of the hardest problems in nucleation theory and its determination requires model considerations. To this end, we need to distinguish between two different types on nucleation; they are HOmogeneous Nucleation (HON) and HEterogeneous Nucleation (HEN). HON occurs ideally in the bulk of a solution which is ideally constituted of solvent and solute molecules only. HEN takes place on substrates that are always present in solutions such as impurity or foreign particles. These objects are a sort of active centers for nucleation. Let us consider first homogeneous nucleation. The surface energy term $W_S(n)$ in HON is given by:

$$W_S(n) = A_C(n)\gamma \qquad \text{Eq. 2.6}$$

where γ, in $\mathrm{J/m^2}$, is the specific crystal-liquid surface energy of the cluster-solution interface and $A_c(n)$, in $\mathrm{m^2}$, is the total area of the cluster surface. In case of HON the surface area of nuclei is:

$$A_C(n) = cV(n)^{2/3} \qquad \text{Eq. 2.7}$$

where c is the shape factor and $V(n)$ is the total volume of a cluster n. For an incompressible cluster, the volume $V(n)$ can be simply written as the product of the molecular volume of the solid crystal v_0 $(\mathrm{m^{-3}/mol})$ and the number of molecules n that constitute the cluster:

$$V(n) = nv_0 \qquad \text{Eq. 2.8}$$

In principle v_0 should be calculated at nanoscopically cluster scale. However, the CNT assumes that v_0 can be approximated by that corresponding to a large macroscopic crystal. Thus v_0 is given by:

$$v_0 = \frac{M_W}{\rho N_A} \qquad \text{Eq. 2.9}$$

where M_W $(\mathrm{g/mol})$ is the molecular weight of the crystal, ρ is the density of the crystal $(\mathrm{g/m^3})$ and N_A is the Avogadro's number. Assuming that clusters are spherical, the shape factor is equal to:

$$c = (36\pi)^{1/3} \qquad \text{Eq. 2.10}$$

By using these equations, the general work required for homogeneous nucleation expressed by Eq. 2.1 can be rewritten as:

$$W(n) = -\,n\Delta\mu + A_C(n)\gamma = -\,n\Delta\mu + (36\pi)^{1/3}(nv_0)^{2/3}\,\gamma \qquad \text{Eq. 2.11}$$

$W(n)$ is a polynomial function of n composed by a "negative" volume term and a positive "surface" term. Hence, there is a critical nucleus size n^* for which volume forces balance surface forces. This results in a maximum of $W(n)$ that defines the energy barrier to nucleation providing the parameters n^* and $W(n^*)$. These quantities are readily obtained by solving the following equation for maximum:

$$\left(\frac{dW(n)}{dn}\right)_{n\,=\,n^*} = 0 \qquad \text{Eq. 2.12}$$

Thus:

$$n^* = \frac{32\pi v_0^2\gamma^3}{3(KTlnS)^3} \qquad \text{Eq. 2.13}$$

and

$$W(n^*) = \frac{16\pi v_0^2\gamma^3}{3(KTlnS)^2} = \frac{1}{2}n^*KTlnS \qquad \text{Eq. 2.14}$$

From Eq. 2.11 it follows that:

$$\frac{dW(n^*)}{d\Delta\mu} = -\,n^* \qquad \text{Eq. 2.15}$$

This is the nucleation theorem which has been proven to be valid for both HON and HEN in any kind of one-component (one solute) nucleation systems[37].

In the Classical Nucleation Theory, the mechanism of nucleation is considered to be a consecutive series of molecules, or monomers, attachments and detachments to form different clusters. This model has been proposed by Szilard and outlined in Figure 2.1:

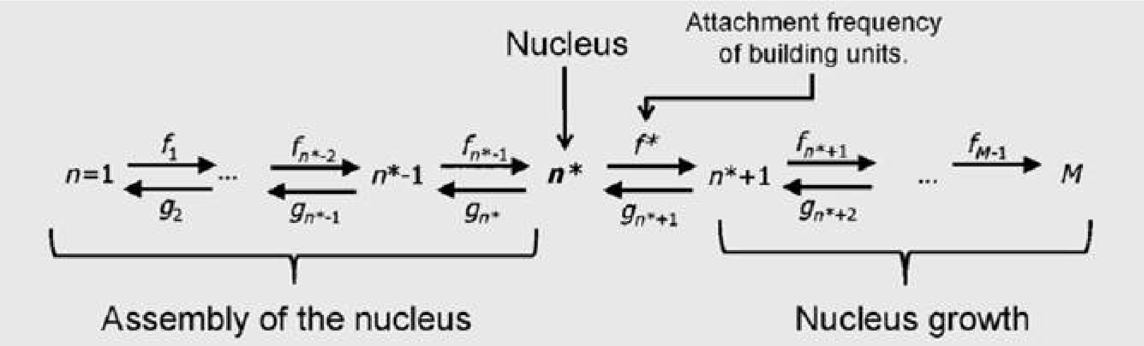

Figure 2.1. Szilard model of nucleation.

The model is based on two main assumptions:

- Only single monomers can leave a cluster.
- There are many more monomers than clusters in normal solutions, so collisions between two clusters are very rare compared to cluster-monomer collisions.

The f terms correspond to the attachment frequency (s^{-1}) and express the rate at which the monomers stick on a cluster surface. Similarly, the g terms refer to the detachment frequency (s^{-1}) which is the rate at which the monomers break apart from a cluster surface. Considering that temperature and supersaturation are constant over time, these frequencies will be time-independent. Constant supersaturation is an assumption, that derives from the fact that the size of a nucleus is negligible compared to the overall number of solute molecules in the liquid phase. The process is then characterized by the stationary *nucleation rate* J which is the number of nuclei produced by unit of time and volume $(\mathrm{m}^{-3}s^{-1})$. The nucleation rate is modeled as the net flux of forming critical nuclei n^* which can grow giving stable crystals. Therefore, in conformity with the above “reaction” scheme, J can be determined as the difference between the rate of building or attaching units $n^* \rightarrow n^* + 1$ and the opposite rate of detaching units $n^* + 1 \ \rightarrow n^*$:

$$J = f(n^*)C(n^*) - \ g(n^* + 1)C(n^* + 1) \qquad \text{Eq. 2.16}$$

where $C(n^*)$ and $C(n^* + 1)$, in (m^{-3}), denote the time-independent stationary concentration of clusters with n^* and $n^* + 1$ monomers, respectively. This equation can be simplified as follows using the Zeldovich factor z:

$$J = \mathrm{z} f^* C^* \qquad \text{Eq. 2.17}$$

where the term $g(n^* + 1)C(n^* + 1)$ is ignored and the factor z is introduced to compensate for the effect of detachments of monomers from cluster. $f^* \equiv f(n^*)$ and the stationary concentration of clusters $C(n^*)$ is replaced by their equilibrium concentration $C^*(\mathrm{m}^{-3})$. Considering an ideal mixture of clusters of all n sizes in a solution, the equilibrium concentration $C(n)$ can be expressed by the following Boltzmann-type formula:

$$C(n) = C_0 \mathrm{e}^{\left(-\frac{W(n)}{KT}\right)} \qquad \text{Eq. 2.18}$$

Accordingly, the equilibrium concentration $C^* = C(n^*)$ of nuclei is given by:

$$C^* = C_0 \mathrm{e}^{\left(-\frac{W(n^*)}{KT}\right)} \qquad \text{Eq. 2.19}$$

where C_0, in m^{-3}, is the concentration of active nucleation sites in the solution. In HON, C_0 can be approximated considering that each molecule of solute provides a nucleation site for the process. Therefore, a good estimation for C_0 is:

$$C_0 = \frac{1}{v_0} \cong 10^{28} \div 10^{29}\ \mathrm{m}^{-3} \qquad \text{Eq. 2.20}$$

The Zeldovich factor z is approximated by[37]:

$$z = \left[\frac{\left(-\frac{d^2 W(n)}{dn^2} \right)_{n\,=\,n^*}}{2\pi KT} \right]^{0.5} \qquad \text{Eq. 2.21}$$

And for the case of HON:

$$z = \left[\frac{W(n^*)}{3\pi KT n^{*2}} \right]^{0.5} \qquad \text{Eq. 2.22}$$

Typical experiments give $1 < \frac{W(n^*)}{KT} < 80$ and $1 < n^* < 100$. It follows that z is $0.01 < z < 1$. Geometrically, z characterizes the curvature of the $W(n)$ curve at $n = n^*$: a greater z value corresponds to a sharper maximum of $W(n)$ at the nucleus size.

Considering Eq. 2.17 the equations above, the only missing parameter we need to determine in order to calculate the nucleation rate J is the attachment frequency. f^* represents the important molecular-level kinetic contribution to the nucleation rate, since not only it reflects how the building units attach to the nucleus, but it can also be assumed that for crystal nucleation from solution this step is the rate-limiting step. Monomer attachment usually occurs by two different mechanisms:

- *Attachment controlled by volume diffusion.* In this first case, the attachment of new molecules to the cluster surface is governed by diffusion. Therefore, f^* is the product of the incoming diffusion flux $j^*$of monomers towards the nucleus surface and the area of this surface A^*. For a spherical nucleus of critical radius $R^* = (3v_0n^*/4\pi)^{1/3}$, j^* is equal to $j^* = DC/R^*$. Since $A^* = 4\pi R^{*2}$, the resulting formula for the attachment frequency reads[37]:

  $$f^* = (48\pi^2 v_0)^{1/3} DCn^{*1/3} \qquad \text{Eq. 2.23}$$

  Substituting Eq. 2.5 we obtain:

  $$f^* = (48\pi^2 v_0)^{1/3} DSC_\mathrm{e}n^{*1/3} \qquad \text{Eq. 2.24}$$

  Here D $(\mathrm{m^2s^{-1}})$ is the monomer diffusion coefficient.

- *Attachment controlled by interface transfer.* In this second case, the molecule to be attached is in immediate contact with the condensed phase and can join the cluster by making a random jump over a distance comparable with the molecule diameter $d_0 = (6v_0/\pi)^{1/3}$. Assuming that the probability of a random jump is proportional to D and that all the monomers that jump on a cluster surface stick on it, $j^* = DC/d_0$. As before $f^* = j^*A^*$, so that:

  $$f^* = (6\pi^2 v_0)^{1/3} DCn^{*2/3} \qquad \text{Eq. 2.25}$$

  and:

  $$f^* = (6\pi^2 v_0)^{1/3} DSC_\mathrm{e}n^{*2/3} \qquad \text{Eq. 2.26}$$

Substituting the above expressions for f^*, z and C^* in the general formula Eq. 2.17 we obtain the following nucleation rate equations.

Nucleation controlled by volume diffusion:

$$\begin{aligned} J_d &= SlnS\left(\frac{KT}{\gamma}\right)^{1/2} DC_{\mathrm{e}}C_0 \exp\left(-\frac{16\pi v_0^2\gamma^3}{3(KT)^3(lnS)^2}\right) \\ &= SlnSA\exp\left(-\frac{B}{(lnS)^2}\right) \end{aligned} \tag{Eq. 2.27}$$

with the pre-exponential factor A $(m^{-3}s^{-1})$:

$$A = \left(\frac{KT}{\gamma}\right)^{1/2} DC_{\mathrm{e}}C_0 \tag{Eq. 2.28}$$

and the dimensionless exponential factor B:

$$B = \frac{16\pi v_0^2\gamma^3}{3(KT)^3} \tag{Eq. 2.29}$$

Nucleation controlled by interface transfer:

$$\begin{aligned} J_t &= S\left(\frac{4}{3}\right)^{1/3}\left(\frac{KT}{\gamma}\right)^{-1/2} \pi^{1/3}{v_0}^{2/3}DC_{\mathrm{e}}C_0 \exp\left(-\frac{16\pi v_0^2\gamma^3}{3(KT)^3(lnS)^2}\right) \\ &= SA'\exp\left(-\frac{B}{(lnS)^2}\right) \end{aligned} \tag{Eq. 2.30}$$

with:

$$A' = \left(\frac{4}{3}\right)^{1/3}\left(\frac{KT}{\gamma}\right)^{-1/2} \pi^{1/3}{v_0}^{2/3}DC_{\mathrm{e}}C_0 \tag{Eq. 2.31}$$

Eq. 2.27 and Eq. 2.30 provide a significant relationship to characterize the nucleation process based on CNT. This is only valid for HON, for the case of HEN the following adjustments are necessary:

- The approximation $C_0 = {}^{1}\!/_{v_0}$ is no longer valid. For HEN on N_a nucleation-active centers in the volume V of the solution $C_0 = N_a/V$. The determination of the available active centers for nucleation is a very hard problem which depends on the concentration of microscopic impurity that is normally present in a crystallizing solution.

- The determination of $W(n)$ for HEN is again done with the aid of Eq. 2.11. The only difference is that in HEN the surface energy term $W_S(n)$ is lower than HON. This is because part of the surface nucleus is "covered" by the foreign particle which shields the nucleus and therefore reduces the area facing the ambient liquid solution. Hence, γ is replaced by the effective specific crystal-liquid surface energy $\gamma_{\mathrm{CL}} = \gamma_{\mathrm{ef}}$ that takes into account the changed nucleation substrate and is defined as:

  $$\gamma_{\mathrm{ef}} = \psi(\theta)^{\frac{1}{3}}\gamma \qquad \text{Eq. 2.32}$$

  The factor $\psi(\theta)$ is given by Volmer equation as a function of the contact angle θ[37]:

  $$\psi(\theta) = \frac{(2 + cos\theta)(1 - cos\theta)^2}{4} \leq 1 \qquad \text{Eq. 2.33}$$

  The wetting contact angle is defined by the Young equation:

  $$cos\theta = \frac{(\gamma_{\mathrm{SL}} - \gamma_{\mathrm{CS}})}{\gamma_{\mathrm{CL}}} \qquad \text{Eq. 2.34}$$

  where γ_{SL} and γ_{CS} are the specific surface energies of the substrate-liquid and crystal-substrate interfaces, respectively (Figure 2.2).

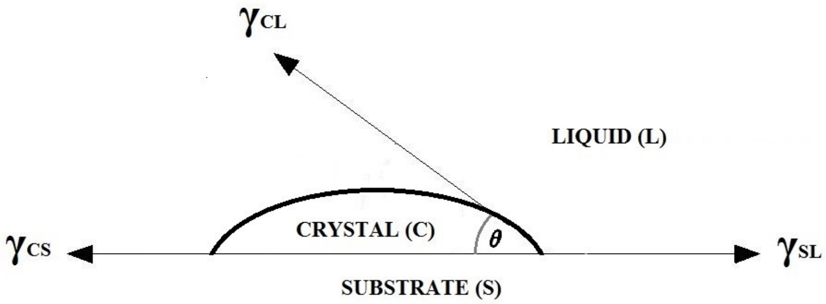

Figure 2.2. Specific surface interfacial energies at the boundaries between three phases.

θ is the angle between the crystalline deposit and the foreign solid surface where the HEN occurs. $\psi(\theta)$ increases monotonically with the contact angle from $\psi(\theta) = 0$ when $\theta = 0°$ (complete wetting condition) to $\psi(\theta) = 1$ when $\theta = 180°$ (non-wetting condition equivalent to HON).

Therefore, by simply replacing γ with γ_{ef}, the CNT leads to the following expressions for n^* and $W(n^*)$ for HEN:

$$n^* = \frac{32\pi v_0^2 \gamma_{ef}^3}{3(KTlnS)^3} \qquad \text{Eq. 2.35}$$

$$W(n^*) = \frac{16\pi v_0^2 \gamma_{ef}^3}{3(KTlnS)^2} = \frac{1}{2} n^* KTlnS \qquad \text{Eq. 2.36}$$

The theoretical determination of f^* is a hard problem for HEN in solution. For instance, if we consider the nucleation controlled by volume diffusion, the concentration field around the nucleus is no longer spherical and the lack of symmetry complicates the calculation of the flux j^* as well as the attachment area A^*. Nonetheless, with some numerical correction of geometrical nature, Eq. 2.25 and Eq. 2.26 can also be used for HON with a sufficiently large contact angle ($\theta > 180°$)[37]. Mersmann et al. recently proposed an equation for f^* which predicts a proportionality of f^* to $C^{4/3}$ [38]. This equation has been questioned by Kashiev et al. as it violates the law of mass action which states that f should be proportional to the monomer concentration C[37].

By accounting for the modifications reported above, the commonly accepted expression for nucleation rate which is valid for HEN can be generally written as follows:

$$J_{HEN} = \mathrm{z} f^* C^* = A_{HEN} S \exp\left(-\frac{B_{HEN}}{(lnS)^2}\right) \qquad \text{Eq. 2.37}$$

where B_{HEN} has the same form of Eq. 2.29 with the only difference that $\gamma = \gamma_{\mathrm{ef}}$:

$$B_{HEN} = \frac{16\pi v_0^2 {\gamma_{\mathrm{ef}}}^3}{3(KT)^3} \qquad \text{Eq. 2.38}$$

The pre-exponential factor A_{HEN} is defined by:

$$A_{HEN} S = \mathrm{z} f^* C_0 \qquad \text{Eq. 2.39}$$

with the Zeldovich factor z from Eq. 2.22. Clearly, finding explicit expression for A_{HEN} requires determination of f^* by means of model considerations for the attachment of monomers to the nucleus. The appearance of S reflects the fact that, in conformity with the law of mass action, the attachment frequency is also proportional to the supersaturation ratio. A theoretical formulation for f^* does not exist for HEN due to the difficulty of accounting for an irregular and unpredictable amount of heterogeneous particles in solution. In addition, HON homogeneous nucleation has not yet been observed to our knowledge for crystallization of solutes, due to the unavoidable presence of these impurities. Moreover, it seems nowadays that the CNT is probably too much simplified: for instance, we do not know whether HON occurs entirely via volume diffusion, interface transfer mechanisms or other steps such as desolvation or two-step nucleation are involved in the nucleation process[39]. In the two-step mechanism, crystalline order is preceded by the separation of a dense, disordered liquid phase. The experimental visualization of kinetic pathways is still a subject of research due to the extremely short time and length scales of the process[35]. In conclusion, due to lack of knowledge in the determination of the attachment frequency, Eq. 2.37 and Eq. 2.39 hold for both homogeneous and heterogeneous nucleation and only the values of A and B differ. To summarize, the expressions for nucleation rates in HON and HEN are the following:

$$J_{HON} = A_{HON} S \exp\left(-\frac{B_{HON}}{(lnS)^2}\right) \qquad \text{Eq. 2.40}$$

$$A_{HON} S = z f^* C_0 \qquad \text{Eq. 2.41}$$

$$J_{HEN} = A_{HEN} S \exp\left(-\frac{B_{HEN}}{(lnS)^2}\right) \qquad \text{Eq. 2.42}$$

$$A_{HEN} S = z f^* C_0 \qquad \text{Eq. 2.43}$$

The A factor appears with the supersaturation S in the pre-exponential term of the equation and accounts for the kinetics of the process, whereas the B factor appears in the exponential term and accounts for the thermodynamic of the process or energy barrier.

Let us now consider the typical solubility curve of Figure 2.3 for a solute dissolved in water. The continuous line defines the equilibrium concentration of the solute at different temperatures. The area on the right side of the curve is called *stable zone*. Here nucleation is not possible, $S < 1$ and the solute is completely dissolved. Let us consider a, for instance, a point within this area at temperature T_3 and concentration C_2. By cooling the solution we approach the solubility curve when $T = T_2$ (a') reaching the equilibrium condition $S = 1$. If we keep cooling our solution we get into the left side of the chart which is called *labile zone* where nucleation is thermodynamically possible and $S > 1$. For relatively low values of S, close to the solubility curve $\left(a^{''}\right)$, the nucleation rate is still very low. J increases by decreasing the temperature and in b the supersaturation reaches a specific value $S = \frac{C_2}{C_1}$ at which J increases rapidly as the exponential factor governs the nucleation rate. This supersaturation level corresponds to a threshold so that in the solubility chart we can define another region which is called *metastable zone* (MSZ) and is bounded by two curves: the solubility curve and the metastable zone limit curve (dashed curve). Within the MSZ nucleation is very unlikely even though crystal growth is still possible due to the presence of a certain driving force. Conversely, the nucleation rises quickly with S beyond the MSZ. Here the exponential term becomes dominant and a small increment of S leads to a large increment of J. Thus, the value of change reaches an experimentally observable one. An important concept to highlight is that the metastable zone width (MSZW) can not be univocally determined. In fact, while the thermodynamic solubility curve is fixed for each solute-solvent system, this is not valid for the MSZ limit which is affected by the particular experimental conditions. In fact, the supersaturation threshold at which J increases rapidly is a function of A and B factors that, in turn, depend on the concentration and the nature of the impurities as well as on the level of turbulence, viscosity of the solution and cooling rate. These parameters, particularly the kinetic parameter A, are difficult to determine and consequently the MSZW results difficult to calculate and reproduce experimentally.

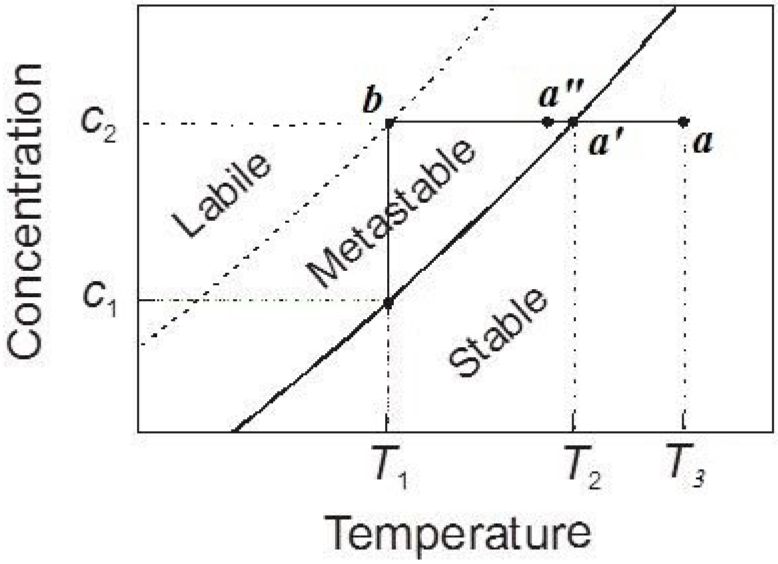

Figure 2.3. Typical solubility curve of a solute in a solvent.

It is important to note that the same supersaturation level in b can be also obtained by concentrating the solution keeping the temperature constant according to a different crystallization technique known as *evaporative crystallization*.

A classical method to estimate the nucleation rate J consists in the determination of the induction time τ which is defined as the time elapsed between the creation of supersaturation (*e.g.* obtained after a temperature quench) and the formation of nuclei of critical size. τ is not easy to measure experimentally and can be considered as the sum of two factors:

$$\tau = \tau_n + \tau_g \qquad \text{Eq. 2.44}$$

τ_n is the time required to reach nuclei of critical size n^* while τ_g accounts for the necessary time needed for those nuclei to grow till a detectable size. The latter relies on the particular detection system, and is strongly related to its sensitivity representing the greater quantity that constitutes τ[40]. According to this definition, the nucleus does not have a clear physical identity and therefore it is hard to distinguish nucleation from growth. In fact, before a stable nucleus n^* reaches an observable size it is still called "nucleus", while after that detectable size it is then considered a growing crystal. As, this limit depends on the particular detection technique adopted, therefore the separation between nucleation and growth is then ambiguous. For a given volume V of solution, the induction time τ is inversely proportional to the frequency of formation of a critical nucleus J. The procedure to determine the nucleation rate J by indirect measurement of induction time τ is commonly used in large perfectly stirred reactors[40,41]. However, the determination of J from τ is challenging since τ does not only depend on the sensitivity of the detection device (growth kinetics of the crystals has to be known) but also, in this type of experiments, usually carried out in macroscopic volumes, impurities play a significant role, a rapid temperature quench is difficult to achieve, and mixing can have an effect[42]. The emerging demand to control the quality product in industrial crystallization processes is stimulating the necessity for developing reliable methods able to measure nucleation rates. In this regard, a new and more successful approach to measure J, particularly suitable for microfluidics systems, is described in the following section and will be adopted in this work.

2.1.2 Stochastic model of nucleation

It is well established that nucleation is a stochastic phenomenon, so that predicting deterministically where and when nucleation events will take place within a given volume is impossible[35]. For this reason, we may adopt two strategies to determine nucleation kinetics. We can work with a single, large volume, which owing to its size behaves deterministically, or with a large number of small, not interacting volumes, which owing to their size behave stochastically. In the first case, at least in theory, one experiment suffices for deriving nucleation rates, while in the second case, to obtain the kinetics, one needs to consider the results of a large set of statistically independent, small-volume experiments. In spite of the advantages that the deterministic approach offers in terms of (simple) experimental setup, this method makes it hard to operate isothermally under uniform fluid dynamic conditions (owing to the large dimensions of the setup), rendering the system difficult to operate, control, and analyze. In fact, in a large system, the shapes, the size distribution and the number of crystals that we obtain reflect the effect not only of primary nucleation but also other mechanisms such as secondary nucleation, breakage, agglomeration and growth. These mechanisms are difficult to consider separately when one adopts a deterministic approach, and so one ends up with a "global" nucleation rate, which combines together all these mechanisms[29].

Microfluidics offers great potential for controlling and studying nucleation. With the aim of generation of kinetics data, microfluidic devices are useful tools for screening crystallization, for they offer good control of transport phenomena (enhanced mass and heat transfer), little gravity effect, and few impurities. Moreover, in specific channel geometries, two-phase flows can produce nearly monodisperse droplets. The hundreds of droplets generated in the microfluidic chip yield a large set of independent nucleation events suitable for conducting a statistical analysis. For example, such systems have been used to calculate nucleation and growth rates for proteins by means of microliter droplets and "double step" temperature profiles, respectively[43]. Droplet-based microfluidic crystallizers are also adopted for controlling crystal size by confining crystallization within nearly identical droplets that reside in the crystallizer for nearly equal times[44]. Various microfluidic devices and experimental procedures have been introduced in recent years to investigate crystal nucleation kinetics of several compounds in static arrays of monodisperse droplets[45,46,47,48,49,50,51,52]. A device example is reported in Figure 2.4.

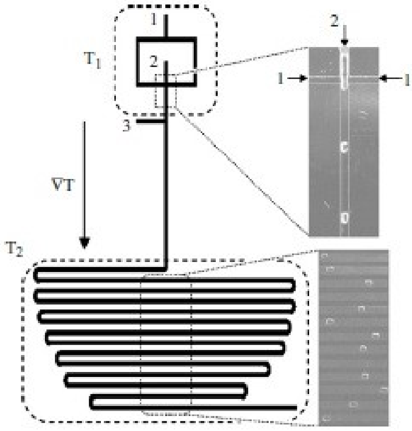

Figure 2.4. Design of a droplet-based micro-device. The oil and aqueous phases are injected, respectively, in inlets 1 and 2. Oil can also be injected in inlet 3 to increase the velocity of the droplets. The two dashed areas are temperature controlled at T_1 and T_2[48].

Although the nucleation process is stochastic, the primary nucleation rate can be regarded as a deterministic quantity. This is because $J(S)$, which represents the expected (or mean) number of nuclei generated per unit volume and time at a given supersaturation ratio S refers to volumes that are sufficiently large to eliminate the stochastic (or random) nature of the process. For conventional batch crystallizers, one can thus adopt a deterministic modeling approach, on the basis of the *population balance* equation[53]. This is a technique to measure crystal nucleation describing nucleation directly in terms of $J(S)$. On the other hand, for small-volume systems (droplets), one needs to resort to a statistical modeling approach[52]. The most reliable way of measuring crystal nucleation kinetics is the droplet method. Each droplet behaves as a single (random) batch system, and a large number of such systems permits deriving the required statistics and therefore the nucleation rate $J(S)$ as reported below.

For small volumes the process is stochastic and the probability $P_T(n,t,S,V)$ to measure n_c crystals in a vessel of volume V within a time t for a solution at supersaturation S evolves as a stationary Poisson's process[48,54]:

$$P_T(n_c,t,S,V) = \frac{N(t,S,V)^{n_c} e^{-N(t,S,V)}}{n_c!} \qquad \text{Eq. 2.45}$$

where:

$$N(t,S,V) = J(S)Vt \qquad \text{Eq. 2.46}$$

is the expected average number of crystals formed per unit time and volume by the nucleation rate $J(S)$.

The probability of not measuring crystals is given by:

$$P_T(n_c = 0,t,S,V) = e^{-N(t,S,V)} = e^{-J(S)Vt} \qquad \text{Eq. 2.47}$$

Thus, the *cumulative distribution function* $P_T(t,S,V)$, which represents the probability of detecting *at least* one crystal within a time t in a droplet of volume V at a given supersaturation ratio S, is equal to[55]:

$$P_T(t,S,V) = 1 - P_T(n_c = 0,t,S,V) = 1 - e^{-J(S)Vt} \qquad \text{Eq. 2.48}$$

This probability increases with the time, the volume and the nucleation rate. It is worth mentioning that if at a given time many crystals are present, they almost certainly did not nucleate at the same time, and so almost certainly do not have the same size: a crystal size distribution is therefore present. For infinite times, volumes and nucleation rate, the cumulative distribution $P_T(t,S,V)$ tends to unity. The infinite time limit $\lim_{t\to\infty} P(t,S,V) = 1$ indicates that at thermodynamic equilibrium an event that is bound to happen will have happened. Whereas, the infinite time limit $\lim_{V\to\infty} P(t,S,V) = 1$ is the macroscopiclimit which represents the condition of the stochastic process towards the deterministic one.

To obtain the probability function experimentally, we operate as follows. In a small droplet sample of a given volume V containing a solution at a given supersaturation ratio S, we record the time t at which crystals are detected. For all times shorter than t no crystals are visible, whilst for all larger times crystals are detectable. We then repeat the same experiment, in the same conditions, M times. With these data, one can obtain the experimental probability function $P_E(t,S,V)$. If we denote as $M^+(t,S,V)$ the number of droplets in which at least a crystal forms within a time t and as M the overall number of droplets considered, then

$$P_E(t,S,V) = M^+(t,S,V)/M \qquad \text{Eq. 2.49}$$

From a statistical standpoint, M needs to be large enough that its choice does not affect the value of $P_E(t,S,V)$. Eq. 2.49 allows determining the cumulative distribution function experimentally. In reality, even the more accurate equipment is able to detect only particles with size greater than a minimum size d^*. If a crystal of size $d < d^*$ were present in the volume V, we would thus not be able to detect it. To solve this problem we perform our experiments using a double step temperature technique combined with probability function analysis[43,50]. According to this technique, the first step represents the nucleation stage, in which nuclei form at S within a fixed residence time t, afterwards, we move our nuclei within a second step (growth) to let crystals grow up to a detectable size d^* for a time t_{d^*}. In the second step the supersaturation is changed to S^* (by changing the temperature) to be close to the solubility curve so that we can only grow those crystals nucleated in the previous stage. Thus:

$$P_E(t, S, V) = P_E(t_{d^*}, S^*, V) \qquad \text{Eq. 2.50}$$

Eq. 2.48 permits the determination of the value of the nucleation rate $J(S)$: that is, the number of nuclei formed per unit time and volume at a given supersaturation ratio S. Note that, even though Eq. 2.48 and Eq. 2.49 involve the volume of the droplets as independent variable, the value of the nucleation rate does not depend on it; as reported in Eq. 2.49, $J(S)$ depends solely on the supersaturation ratio S. To obtain its value, we fit the theoretical function $P_T(t, S, V)$ with the experimental function $P_E(t_{d^*}, S^*, V)$. Note that the nucleation rate determined in this way refers to primary nucleation, inasmuch as the probability function has to do only with the presence of at least one crystal: it is not concerned with the total number of crystals present in each droplet. Only the latter might be affected by the presence of secondary nucleation. The probability function relates only to primary nucleation. In classical nucleation theory, the primary nucleation rate is given by:

$$J(S) = ASexp\left(-\frac{B}{(lnS)^2}\right) \qquad \text{Eq. 2.51}$$

where A and B are the kinetic and thermodynamic parameters for the selected compound. We may rewrite Eq. 2.51 equivalently as

$$y = lnA - Bx \qquad \text{Eq. 2.52}$$

where

$$y = ln[J(S)/S] \text{ and } x = 1/(lnS)^2 \qquad \text{Eq. 2.53}$$

If we repeat the experimental campaign described above for different values of S, we can obtain the function $y(x)$ and, from its linear diagram, the values of the parameters A and B (from the intercept and the slope of the line, respectively). A and B are related to other variables of interest such as the nucleus size n^*, the nucleation work $W(n^*)$, the Zeldovich factor z, the attachment frequency f^*, the concentration of nucleation sites C_0, and the crystal-liquid interfacial energies for homogeneous and heterogeneous nucleation, here denoted as γ and γ_{ef}, respectively. These, except for γ, are all functions of A, B, and S; their expressions are given by the classical nucleation theory

$$n^* = \frac{2\mathrm{B}}{(lnS)^3} \qquad W(n^*) = \frac{1}{2}n^*KTlnS \qquad z = \left[\frac{W(n^*)}{3\pi KTn^{*2}}\right]^{0.5}$$

$$f^*C_0 = \frac{AS}{z} \qquad \gamma_{ef} = \left(\frac{3B(KT)^3}{16\pi v_0^2}\right)^{1/3} \qquad \text{Eq. 2.54}$$

So far, two approaches have been most widely used in the literature to determine the nucleation rate $J(S)$: the polynuclear nucleation mechanism (PNM) and mononuclear nucleation mechanism (MNM). The former assumes that, when nucleation starts taking place, several stable nuclei appear simultaneously in the solution; these are observed only when their size has increased sufficiently for detection. Conversely, the latter mechanism assumes that nucleation originates via a single crystal. The MNM and PNM approaches model different processes that are encountered in reality and lead to different expressions for the cumulative distribution function $P_T(t,S,V)$, because they describe two limiting cases of nucleation that can occur in practice. The MNM and PNM hold for small and large fluid volumes, respectively[40]. In the mononuclear mechanism (operative in small volumes) the process is controlled only by the nucleation rate J, because the growth rate G (ms^{-1}) is so high that the very first supernucleus leads to crystallization. As a result, experimental technique allows one to focus on a small portion of the solution and easily detect the first crystal appearance. Conversely, in the polynuclear mechanism (operative in large volumes), the process is controlled by growth rate G of the crystallites and then more nuclei have time to come into being while the first nucleus grows to a macroscopic size. As a result, multiple crystal appearance in the solution is generally observed within the solution volume.

In this work, the $P_T(t,S,V)$ reported so far refers to the mononuclear nucleation mechanism because the experimental conditions reflect the requirements for the applicability of such a mode (refer to section 4.3.4 for details). The MNM has been used with promising results and good data fitting to describe nucleation in microfluidic devices; for instance, for m-ABA and L-His[55,56], lysozyme[57] and isonicotinamide[50] assuming the MNM as the dominant nucleation mechanism, instead of the PNM, led to better experimental data fitting.

It is worth noting that according to the definition, the mean time of formation of the first nucleus is given by[40]:

$$\tau_{mean} = \int_0^{\infty} t \frac{dP_T(t,S,V)}{dt} dt = 1/J(S)V \qquad \text{Eq. 2.55}$$

Since it is postulated that the system loses its metastability just at the moment when the first nucleus comes into being, the induction time τ, for new phase formation coincides with τ_{mean} and can be simply calculated by knowing the nucleation rate $J(S)$ and the volume V.

$$\tau = \tau_{mean} = 1/J(S)V \qquad \text{Eq. 2.56}$$

If the induction time data are obtained by a method involving three dimensional growth of the nucleus to a registrable macroscopic volume V_m which is a fixed fraction $\alpha_V = V_m/V \leq 1$ of the parent phase volume V, the requirement $\tau \gg \tau_g$ sets up the limit of applicability of the MNM. Thus:

$$\tau \gg \tau_g \quad \rightarrow \quad \frac{1}{JV} \gg \frac{(V_m)^{\frac{1}{3}}}{G} \quad \rightarrow \quad \frac{1}{JV} \gg \frac{(\alpha_V V)^{\frac{1}{3}}}{G} \quad \rightarrow$$

$$V \ll \alpha_V^{-\frac{1}{4}} \left(\frac{G}{J}\right)^{\frac{3}{4}} \qquad \text{Eq. 2.57}$$

Finally, it is also important to note that the CNT assumes the supersaturation remains constant during the nucleation event as if an infinite reservoir of molecules would be available. If we operate with small volumes, the total number of molecules is decreased and this reservoir becomes finite, in contradiction to the CNT, thus increasing the energy barrier needed to form stable clusters. Nucleation experiments conducted with different microfluidic devices show that volume does not affect the nucleation process and even volume samples of nanoliter scale are still representative of nucleation in an infinite volume[58].

2.1.3 Secondary nucleation

The expressions for homogeneous and heterogeneous nucleation reported so far refers to the particular nucleation process known as *primary nucleation*. Nevertheless, another nucleation mechanism known as *secondary nucleation* can also occur in nucleating systems. The difference between these mechanisms is explained with the help of Figure 2.5:

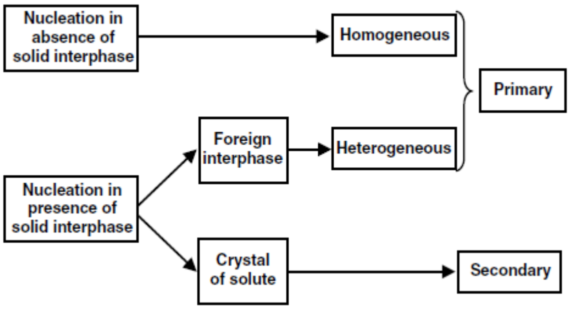

Figure 2.5. Outline of different nucleation processes: homogeneous, heterogeneous, primary and secondary nucleation.

It has been observed that nuclei can be generated at very low supersaturation within the MSZW, when crystals of the same material (crystal of solute) are already present in solution, for instance in the form of added seed crystals (seeding technique) or attrition fragments. Such fragments or secondary nuclei generally result from crystal-crystal or crystal-vessel shearing action. This mechanical fracture process, also known as *secondary contact nucleation*, is the most important source of secondary nuclei and occurs in systems where the suspension is very dense and subjected to violent agitation or high velocity pumping and stirring. There is evidence in the literature that secondary nuclei that are not attrition fragments can also be formed either as preordered species or as clusters in the immediate solution vicinity of the crystal surface or on the crystal surface by dendritic growth and dendritic coarsening. This mechanism is known as *secondary surface nucleation* and can lead to the formation of nuclei and/or the detachment of small dendrites from the crystal surface without any fluid dynamics or mechanical shear. These small particles detach in solution, while the stable ones continue to grow[1,38]. Different correlations are available in the literature to account for the generation of these secondary nuclei by adding an extra term to the classic primary nucleation rate equation shown before. This term is a function of supersaturation, operating parameters, vessel geometry physical properties of the solid-liquid system[38].

2.1.4 Crystal growth

Once stable nuclei are formed in a supersaturated solution, they begin to grow into crystals of macroscopic size. Several growth mechanisms have been proposed in the literature and investigated experimentally[1]. Nowadays, the *diffusion-reaction mechanism* is the most widely accepted growth theory to describe crystal growth in supersaturated solution[1,38]. According to this theory, the complex process of crystal growth is simply divided into two main steps: the diffusion of the solute from the solution to the surface of the crystal and the reaction, consisting of the integration of growth units oriented into the crystal lattice, with the supersaturation being the driving force. A representation of these two stages is shown in Figure 2.6.

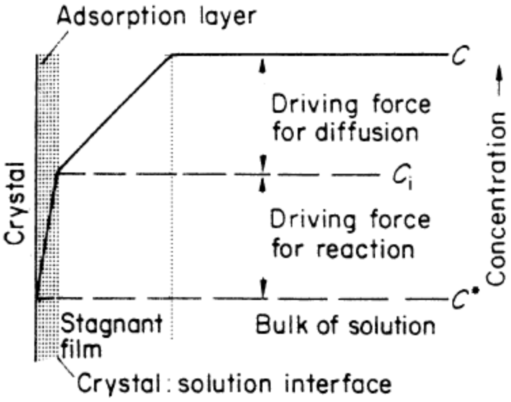

Figure 2.6. Concentration driving forces in crystallization from solution according to the diffusion-reaction model.

Crystal growth occurs under the influence of two different concentration gradients. Molecules of solute diffuse thorough the first stagnant film (its thickness probably does not exceed 100 Å) of liquid adjacent to the growing crystal face A_C by the gradient $(C - C_i)$ and then arrange themselves into the crystal lattice according to the r_i-order integration reaction within the boundary reaction layer $(C_i - C^*)$. As a result, the mass flux $\left(\frac{dm}{dt}\right)$ towards the crystal surface can be expressed by the equations

$$\frac{dm}{dt} = k_d A_C (C - C_i) \qquad (diffusion) \qquad \text{Eq. 2.58}$$

and

$$\frac{dm}{dt} = k_r A_C (C_i - C^*)^{r_i} \qquad (reaction) \qquad \text{Eq. 2.59}$$

where C is the solute concentration in the supersaturated solution, C_i the solute concentration in the solution at the crystal-solution interface, C^* the equilibrium concentration, k_d is the coefficient of mass transfer by diffusion and k_r is the reaction rate constant for the surface integration process.

The application of Eq. 2.58 and Eq. 2.59 involves interfacial concentrations that are difficult to measure. It is usually more convenient to eliminate the term C_i and introduce a general equation for crystallization based on the "overall" concentration driving force $(C - C^*)$, which is easier to measure:

$$\frac{dm}{dt} = K_G A_C (C - C^*)^{g_i} \qquad \text{Eq. 2.60}$$

where K_G is the overall crystal growth coefficient and g_i is the order of the overall crystal growth process. When $g_i = 1$ the mass flux $\left(\frac{dm}{dt}\right)$ can be rewritten as

$$\frac{dm}{dt} = \frac{A_C (C - C^*)}{\left(\frac{1}{k_d} + \frac{1}{k_r}\right)} \qquad \text{Eq. 2.61}$$

with:

$$\frac{1}{K_G} = \frac{1}{k_d} + \frac{1}{k_r} \qquad \text{Eq. 2.62}$$

When reaction is rapid, i.e. large k_r, $K_G \approx k_d$, the crystallization process is controlled by diffusion. Similarly, when the value of k_d is large, the diffusional resistance is low, $K_G \approx k_r$, and the process is controlled by the surface integration. It is worth pointing out that the diffusion step is generally considered linear with the concentration, while the validity of the assumption of a first order reaction ($g_i = 1$) is questionable. In fact, many inorganic salts give an overall growth rate order g_i in the range 1 to 2[1]. The order of reaction g_i should not be confused with its more conventional use in chemical kinetics, where the order always refers to the power to which a concentration should be raised to give a factor proportional to the rate of an elementary reaction. In crystallization work the exponent, which is applied to a concentration difference, has no fundamental significance and can not give any indication of the number of elementary species involved in the growth process.

There are many theories describing the actual integration step such as *continuous growth model* and *surface nucleation growth model*[38]. However, the detailed description of the different growth integration mechanisms is not the main focus of the present research work and we refer to the specific literature for more details and further developments[1,38,59]. Many different experimental techniques have been employed to measure crystal growth. A single crystal face can be accurately monitored for fundamental growth studies, while measurements made on populations of crystals are more useful for determining overall mass growth rate. Since crystal growth has a complex dependence on temperature, presence of dissolved impurities, supersaturation, turbulence, size and habit, there is no simple or generally accepted method of expressing the rate of growth. However, Eq. 2.63 is the most widely adopted expression that provides the overall linear growth rate G from the deposited mass flux $\left(\frac{dm}{dt}\right)$.

$$\frac{1}{A_C}\frac{dm}{dt} = \frac{3\alpha}{\beta}\rho\frac{dL}{dt} = \frac{3\alpha}{\beta}\rho G \qquad \text{Eq. 2.63}$$

where L (m) is the characteristic size of the crystal, ρ its density and the volume and the surface shape factors $\alpha = V/L^3$ and $\beta = A_C/L^2$, respectively.

2.1.5 Crystal breakage and crystal agglomeration

Nucleation and growth are not the only processes that define the crystal size distribution in a crystallizer. With respect to the real CSD, other mechanisms such as *crystal breakage* and *crystal agglomeration, aggregation and flocculation* play a relevant role in the determination of the final CSD[38].

Small particles suspended in liquid have a tendency to cluster together, leading to agglomeration, aggregation or flocculation. Agglomeration can be considered as the unification of primary particles that are cemented afterward by chemical forces (*e.g.*, by a crystalline bridge between two or more crystals). In the case of aggregation and flocculation, the bonding forces, such as van der Waals forces, are quite weak. A flocculate is a group of particles that consists of primary particles connected by weak cohesive forces. In the case of aggregates, the strength of the bonding forces is intermediate to agglomerates and flocculates. Aggregates and flocculates can occur in saturated or undersaturated solutions and can readily be destroyed. However, strong agglomerates are generated only in supersaturated solutions. Two types of crystal agglomeration can be distinguished: (a) primary agglomeration as a result of malgrowth of crystals (polycrystals, dendrites, and twins) and (b) secondary agglomeration as a consequence of crystal-crystal collisions in supersaturated solutions. It is often difficult to distinguish between the different origins of particles by microscopic observation. For this reason, in this thesis we use the general term “agglomeration” to refer to any process of particle-to-particle formation. Depending if the collision of primary particles is caused by Brownian motion (diffusion controlled) or by fluid-mechanical forces (shear rate controlled), agglomeration mechanism can be also defined as perikinetic or orthokinetic. Agglomeration is dominant in micron ranges of particles and is less important for particles larger than about $50\ \mu\mathrm{m}$, or above a certain critical size which depends on the supersaturation and growth rate[38].

Crystal breakage or fragmentation is a process that includes crystal fracture in crystallizers induced by fluid dynamics. Parent particles are broken down into smaller fragments, resulting in a rapid disappearance of the original particles.

Two main mechanisms exist for this process. The first is a consequence of collisions of particles with parts of the equipment (impeller or walls) of the crystallizer: this is the breakage mechanism expected in dilute solutions. The second is caused by inter-particles collision.

As for secondary nucleation and crystal growth, different physical models have been proposed to account for crystal breakage and crystal agglomeration. An overview of the theory and the details of governing equations for the methods used to predict agglomeration and breakage can be found in the specific literature[38,60].

2.2 Continuous flow crystallization

The vast majority of industrial scale pharmaceutical crystallization processes are done in batches, either as a cooling, antisolvent, or reactive crystallization. Although batch crystallization is widely employed in the pharmaceutical industry, there are still significant issues with batch-to-batch reproducibility which generally affects the quality of the final isolated product. On the other hand, continuous processes, while more difficult to develop, offer a number of substantial advantages over the batch processes. The main advantage of continuous process is related to the smaller size of the equipment that leads to a substantial reduction in both capital and operating expenses. For example, if we assume that we need to produce $16\ \mathrm{tons}$ per annum of API with a solvent to API ratio of $20:1$ and $4\ \mathrm{h}$ residence time, we could support this with $250\ \mathrm{L}$ reactor, whereas a comparable batch system would typically require a $5000\ \mathrm{L}$ reactor[4]. Continuous processing also provides higher reproducibility and control of physical characteristics, CSD and polymorphic form of the crystalline material. The more uniform and homogeneous properties of the final product will enable the elimination of a number of downstream processes (*e.g.* wet or dry granulation) that are normally employed in batches to simply create a more uniform dosage form. In fact, post-crystallization techniques are an additional cost for the process as well as they represent a risk of contamination and inducing solid state transformations and chemical degradations in the product.

The ability to monitor a key parameter such as the crystal size distribution and the mean crystal size of power mixture is an attractive benefit for continuous processing to produce a material with a sufficiently small particle size so that the solubility and hence bioavailability is increased.

Table 2.1 is reported a list of the comparisons between batch and continuous processes[4].

Table 2.1. Comparison of batch and continuous processes.

Variable	Comparison
Equipment footprint and capital expenditure	Continuous processing offers orders of magnitude reduction in equipment footprint giving rise to +20% reduction in the capital expenditure.
Process variability	Batch processes demonstrate significant batch-to-batch variability with regard to physical properties compared to continuous processes.
Yield	In a once through system, a batch process has a higher yield; however, with the appropriate recycling strategy, it is feasible to achieve higher continuous yields.
Material traceability	Process for tracing material in batch process is well understood both from an operational perspective as well as from a regulatory perspective, whereas for a continuous process there is still a gap between operational understanding and regulatory acceptance of this.

Although there is a wide variety of different continuous crystallizer adopted in the chemical industry, two main categories are commonly used for pharmaceutical applications: single or multiple stages mixed suspension mixed product removal (MSMPR) and plug flow reactors (PFR). The former offers a simple temperature control and has low costs of maintenance but is typically less efficient. The latter has a higher efficiency but temperatures are harder to control, maintenance is more expensive and complicated and it is affected by settling of solids and therefore fouling[38,59]. The choice of whether to use a MSMPR or a PFR is primarily driven by the kinetics of the crystallization: the MSMPR is generally preferred for low conversions and long residence times while the PFR is more convenient for higher conversions and short residence times. A MSMPR approach is also attractive due to the flexibility that it offers in being easily converted from batch capacity to continuous capacity.

While numerous examples of continuous crystallization have been implemented successfully in the chemical industry, the application of continuous processes within the pharmaceutical manufacturing still require significant efforts, particularly in the introduction of new continuous technologies such as continuous filtration and grinding and their regulation. In fact, the relatively low volume of API products combined with the current excess of commercial batch capacity, generate a significant resistance to investing in new technologies/approaches for adopting a continuous process. However, the advantages in terms of product quality and the longer term savings that are offered by switching to continuous processing will enable these processes to become embedded within the industry. For example, recently a continuous MSMPR laboratory-scale crystallizer that can operate in batch or continuous mode has been designed for adipic acid sonocrystallization with promising results in terms of narrow CSDs and high rate of crystal production[16,33,61,62].

The successful resolution of problems related to continuous processing would also allow continuous crystallization to be done at the microscale or milliscale and thus would allow process chemists/engineers to develop flow chemistry and purifications at the same time. As compared to large crystallizer, microfluidic systems offer higher heat and mass transfer. Therefore, the ability to carry out crystallization experiments in microreactors provides a new route that will enable rapid form screening and crystallization process understanding of compounds development. The advantages and the drawbacks of microfluidic crystallization will be discussed in more detail in the next section.

2.3 Microfluidics

Microfluidic systems manipulate and control fluids that are geometrically constrained within environments having internal dimensions, or hydrodynamic diameters, on a scale of micrometers. The term *“microfluidics”* is still a quite vague term which is often used to define fluids with different fluid dynamic conditions. In fact, while some authors consider microsystems all the devices that operate with a characteristic channel size below $500\ \mu\mathrm{m}$ some others resort to a more flexible definition which considers a microsystem one that operates at Reynolds and thermal Péclet numbers below 250 and 1000 respectively. According to the latter definition, microfluidic reactors that have a characteristic dimension above $500\ \mu\mathrm{m}$ can still maintain a microfluidic regime by using low flow rates[31].

Some simple considerations show what various opportunities can emerge from miniaturization of reaction systems. The intrinsic advantages associated with performing chemistry in microfluidic devices are simply due to the scale-dependent processes of heat and mass transfer. Small fluidic volumes dictate that regimes of low Reynolds number are the norm, with fluids being increasingly influenced by viscosity rather than inertia. These low values of Reynolds affirm that viscous forces typically overwhelm inertial forces, and the resulting flows are laminar. Furthermore, for very small Reynolds values, the nonlinear terms of the Navier-Stokes equation disappear, resulting in linear and predictable Stokes flow. Without the inertial nonlinearity, straightforward microfluidic systems have regular, deterministic flow generating in circular micro-channels the typical Poiseuille parabolic velocity profile. In addition, due to the short distances in microfluidic channels, the transport times of mass and heat are shortened. Fast and controlled heat supply as well as cooling is facilitated due to high surface to volume ratio. Therefore, important running conditions of chemical processes, such as compound concentration and temperature, can be regulated precisely. These basic properties give rise to several advantages that have made the technology attractive for chemical synthesis in both industry and academia[31].

With respect to cooling crystallization performed in micro geometries, we highlight the following important advantages[31,32]:

- Fast and easy temperature control. Supersaturation is changed with a defined temperature quench in the solubility diagram, the experiment describes almost a step trajectory of S from undersaturated to supersaturated region. This allows one to perform nucleation studies resorting to a droplet-based stochastic approach (Figure 2.7).
- Simple crystal detection. The optical access and tight control of supersaturation offer the potential for detailed studies of fundamental nucleation processes, as well as fast screening of crystallization conditions (Figure 2.7).
- Nucleation and growth decoupling. Laminar and predictable continuous flow crystallization allows one to improve process controllability by maximising segregation in the spatial domain of the key processes of crystal nucleation, growth and disruption.
- Simple integration of different functional units for crystallization. Mixer, heater, separation and detection units can be easily implemented in a channel network.
- Numbering up. Scale-up by increasing the number of units instead of their size (numbering up) can be implemented to increase throughput maintaining the benefits of each microfluidic device. As every reactor is identical to the pilot reactor, there is no need to change dimensions or conditions.

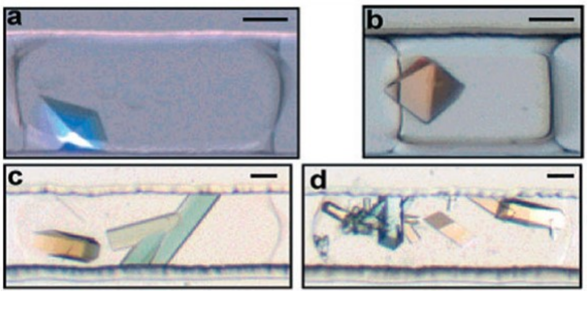

Figure 2.7. Example of different proteins crystallized within droplet-based system[32].

The advent of microreaction technology was initially underpinned by silicon microfabrication methods originally developed from the microelectronics industry. However, as new or improved precision engineering methods and tools become available, they allow manufacture of microengineered structures from metals, ceramics, silicon, glass and plastics (Figure 2.8)[27]. The standard microfluidic device employed in microreactor engineering is commonly fabricated in silicon by means of photolithography and deep reactive-ion etching (DRIE). Alternatively to microchips, simple, flexible and cheap microfluidic layouts can be also realized using plastic capillary tubes or hollow fibers[46,63]. Further information on the progress of ‘cleanroom’ fabrication processes for engineering solid flat substrates and other microfabrication technologies and details are available on specific reviews and textbooks[27,28,64].

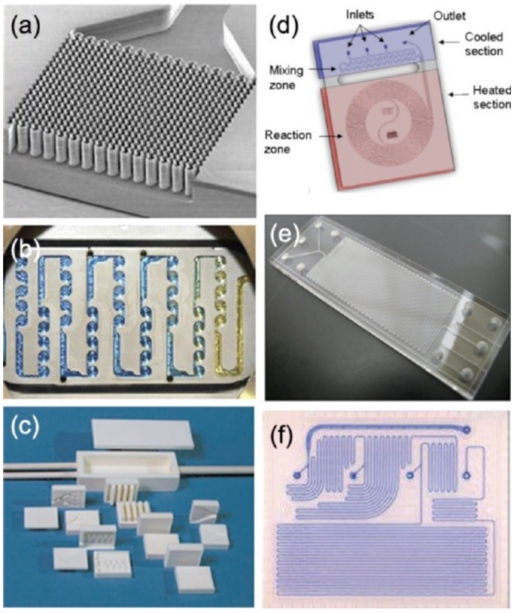

Figure 2.8. Microfluidic devices available in different geometries and material. (a,b) Metal devices fabricated from stainless steel and special alloys. (c) Chemically inert ceramic devices. (d) Devices made from silicon. (e,f) Glass microreactors[65].

Despite all the advantages mentioned before, microstructured reactors are not currently widely employed in the manufacturing industry because, except for those active pharmaceutical ingredients (API) that are produced in small quantity, they often have a throughput that is insufficient for industrial applications. Numbering up (replication of many units) is commonly used in order to overcome the problem related to the insufficient throughput. However, creating parallel channels to increase the production rate can cause fluid maldistribution that can severely affect the performance of the microreactors. In fact, if the distribution of the fluids inside the microchannels is not accurate, the velocity of the fluids, and consequently the flow pattern, can change from channel to channel leading to problems related to pressure drop, residence time distribution etc. Moreover, microchannel fabrication is time and cost consuming and once a microchip has been fabricated, there is rarely any opportunity to make variations to the device. In addition to this, the major challenge that still continues to limit the use of microfluidic devices is the ability to perform operations involving solid particles[20,65]. In this regard, channel occlusion represents the crucial problem that has to be solved to get more reproducible results also improving the whole process working time. A lack of technological approaches or fundamental understanding of how to deal with particulate matter in microscale laminar flow often leads to devices that clog rendering them inoperable.

2.3.1 Particulate flows in channels

The need to handle particulate in small channel geometries remains a crucial problem in continuous fine chemical manufacturing and several strategies have been adopted to reduce channel blockage. However, managing solids in microfluidic devices without resulting in particle deposition on the channel surfaces is practically impossible and therefore, microchannel devices need to be regenerated and cleaned regularly. Particulate flow is even more challenging when dealing with crystals obtained by cooling crystallizing solutions that are flowing through the channels. In fact, channel surfaces represent a potential site for heterogeneous crystallization: nucleation takes place along the channel walls where the thermodynamic conditions are favored as compared to the bulk of the solution where nucleation would be mainly homogeneous. In this regard, if particles form and stick the wall they can grow and bridge till clogging the entire channel cross section limiting fluid flow and thereby render continuous crystallization process inoperable. Moreover, particle accumulation can also impact the heat transport via conduction. Material deposits reduce the effective thermal conductivity of the channel walls and therefore the heat to be added or removed. To prevent and attenuate particle deposition the following aspects need to be considered[65]:

- Fluoropolymer surfaces exhibit non sticky properties and therefore are particularly suitable to minimize the mass of material deposited.
- Glass, metal and silicon surfaces are subjected to micro-etching and surface pitting when exposed to strong acids or bases. This will enhance surface roughness increasing the potential sites for heterogeneous nucleation.
- Continuous reactor fabrication techniques that produce rough surface devices are more likely to cause accumulation problems.
- Particle-to-wall attraction that depends on the ionic strength of the fluid media and the relative particle and wall surface charge, creates conditions for particle deposition. In this regard, manipulation of surface chemistry, such as superhydrophobic and superoleophobic surfaces, has been shown to be effective in reducing particle accumulation.
- Insoluble reaction by-product can undergo nucleation and deposition on reactor walls. In this case the reactor residence time has to be lower than the induction time of by-product formation.
- Channel surface roughness, very high specific surface aspect and temperature inhomogeneity between the channel wall and the bulk, can drastically improve the clogging phenomena. Moreover, channel particular features like bottlenecks, edges, cavities and tight curves are generally undesired patterns that promote crystal deposition and therefore agglomeration and caking.

Three main hydrodynamic mechanisms can lead to plugging in laminar flow:

- *Particle deposition*

Channel blockage generally occurs due to the deposition of particles along the channel surfaces. The Stokes number St, is a useful quantity in estimating the risk of clogging via inertial impaction. This number is defined as the ratio of the characteristic time of the particle (the time constant in the exponential decay of particle velocity due to drag) to the characteristic time of the flow[66]:

$$St = \frac{\text{Solid Response Time}}{\text{Fluid Response Time}} = \left(\frac{\rho_D d^2}{18\mu_L}\right) \Big/ \left(\frac{w}{v_L}\right) \qquad \text{Eq. 2.64}$$

where ρ_D is the particle density, d the particle diameter, μ_L the viscosity of the fluid, v_L the velocity of the fluid and w the channel characteristic size (typically its diameter). For $St > 1$, particles will detach from a flow especially where the flow velocity decreases abruptly. Whereas, for $St < 1$, particles will follow fluid streamlines (perfect advection), the particle motion will be tightly coupled to the fluid motion and the particle dispersion will be the same as the fluid dispersion. In conclusion, particle deposition can be essentially characterized by the Stokes number and the amount of deposition tends to increase with the Stokes number. The definition of the Stokes number given in Eq. 2.64 is valid in the case of stokes flow when the Reynolds number is low enough that the particle drag coefficient is inversely proportional to the Reynolds number itself.

- *Hydrodynamic bridging*

Channel clogging normally occurs when particles travelling along laminar streamlines approach simultaneously a channel constriction. Their mutual interaction results in particle-to-particle cross-linking. This phenomenon is commonly known as bridging and consists in the formation of large agglomerates that block the channel section. Experimental results show that bridging is only a statistical phenomenon which is a function of time, flow rate and channel geometry. Semi-empirical correlations have been formulated for microchannel of rectangular cross-section and irreversible sticking events. For instance, for a given quite high flow rate, the average number of particles N^* that can pass through a microchannel before clogging occurs is[67]:

$$N^* \cong \frac{{w_c}^3 h}{6\omega^2 d^4} \qquad \text{Eq. 2.65}$$

where w_c is the microchannel constriction width, h the microchannel height which is constant before and after the constriction, $\omega = \varepsilon/d$ the ratio of the particle sticking distance from the wall (ε) to the particle diameter d. Whereas, the clogging time t^* can be expressed as follows[67]:

$$t^* \cong \frac{N^* V_p}{Q\chi} \qquad \text{Eq. 2.66}$$

where Q is the fluid flow rate, χ the particle volume fraction and V_p the particle volume. Identifying a potential constriction problem in a continuous microprocess is made possible through the monitoring of the pressure drop from the inlet to the outlet of the reactor.

- *Random detachment of deposits*

In the presence of a sufficiently high shear stress, the formation of deposits on the channel surfaces can undergo random detachment or breaking. This creates the potential of rapid bridging downstream and consequent tubing blockage. Amorphous or crystalline material stuck on channel surfaces can fail under shear stress by adhesive or cohesive failure. The former phenomenon is defined as the simple deposit detachment from the material-wall interface while the latter consists in the breakage of the deposit within is own crystalline or amorphous network. Both mechanisms are totally stochastic and therefore difficult to model and predict[68]. Instead of understanding the random detachment phenomenon, it is more useful to yield insight on how to manage it. Adhesive and cohesive failure can be limited by surface chemistry modification, manipulation of surface roughness and application of external forces that induce shacking such as acoustics waves or pressure gradients applied by pumping[65].

In recent years, continuous particle separation can be achieved using several techniques which typically focus particles within selected streamlines in a channel exploiting the interaction of particles with external electric, magnetic and acoustic fields[69]. Downstream particles or crystals that are not accumulated within the channel are therefore separated in batch processes, such as filtration, centrifugation, chromatography or electrophoresis. Crystals in the dry state can be in two forms: agglomerated (hard bonds between primary particles due to sintering) or aggregated (held by weaker van der

Waals forces). Agglomerates and aggregates are typically separated when added to a liquid using several methodologies (*e.g.* ultrasound technologies) that allow overcoming attractive forces. This strategy is commonly employed before measuring particle size distributions. Particles are suspended in a carrier fluid and surfactants and ultrasound are applied to separate and disperse eventual agglomerates before taking any measurements. Aggregate and agglomerate bonds are the result of simultaneous physical and chemical mechanisms that depend on the particular crystal-solvent system, supersaturation, crystal shape, fluid shear and hydrodynamic effects[70].

2.3.2 Liquid/Liquid (L/L) two phase flow: addressing the clogging issue

One of the most common solutions adopted to prevent clogging in microchannels relies on the introduction of an immiscible phase. The main flow is fragmented in a tee or cross junction in small segments (Figure 2.9), droplets or plugs that constitute the dispersed phase, separated one from the other by a continuous phase (typically a hydrocarbon or fluorocarbon oil)[71,72]. By using these plugs as individual batch reactors, we can confine the solid products within the droplet volume, thus keeping the particles away from the tubing walls[73].

In laminar flow each plug breakup in a repeatable manner and is separated from the channel wall by a thin film of continuous phase which spontaneously forms when the carrier fluid and the wall have similar wetting properties[74].

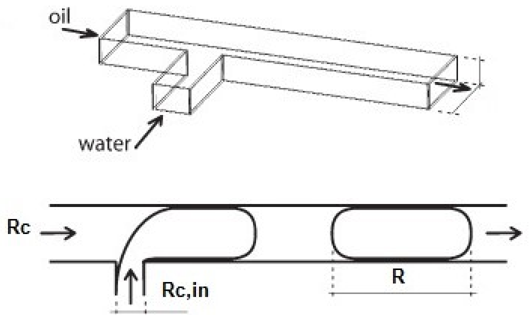

Figure 2.9. Schematic of the microfluidic T-junction composed of rectangular channels[75].

Many attempts have been done to determine both numerically or experimentally the wetting film thickness. It is generally accepted that the film thickness h_w is $1 - 5\%$ of the channel radius R_c and scales according to the Bretherton's law as follows[76]:

$$h_w \propto R_c Ca^{2/3} \qquad \text{Eq. 2.67}$$

where Ca is the dimensionless capillary number, which is the ratio of viscous-to-interfacial tension stress, given by:

$$Ca \propto \frac{\mu_{cp} V_{Plug}}{\gamma_p} \qquad \text{Eq. 2.68}$$

where μ_{cp} is the viscosity of the continuous phase, V_{Plug} the plug velocity and γ_p interfacial tension between the two fluid phases. It has been proved that, although Eq. 2.67 is derived for gas-liquid Taylor flow, the equation is still valid for liquid-liquid systems when the viscosity of the continuous phase is larger than the dispersed phase and $Ca < 0.01$[77]. Two phase flows are distributed into a rich variety of flow patterns (Figure 2.10) depending on the flow rate ratio between the two phases, channel geometry, characteristic size and wetting properties as well as presence of surfactants and fluids viscosity[71,72,78,79,80]. Figure 2.10 displays all the situations observed in a range of flow rates. Isolated structures flowing with the mean flow velocity are obtained in the upper left corner at low water flow rates and substantial oil flow rates. These drops are produced by the interfacial instability taking place at the channel intersection. Once the drop is formed is entrained by the flow and its shape does not evolve any further. As the oil flow rate is decreased, the water concentration increases, and drops tend to assemble into pairs or triads or larger structures (pearl-necklace state). Other regimes appear at higher flow rates corresponding to the upper right part of the diagram. In this particular case the interfacial instability leading to drop formation ceases to hold because viscous forces (which increase with the flow rate) now prevail against capillarity. As a consequence, water simply flows into an oil tube and this gives rise to a stratified regime. At the right bottom right the oil drop is formed at the entrance but it travels with a long tail connected to the entrance region. This particular shape is stil under investigation and it might due to the depletion of surfactant at the tip of the drop[78].

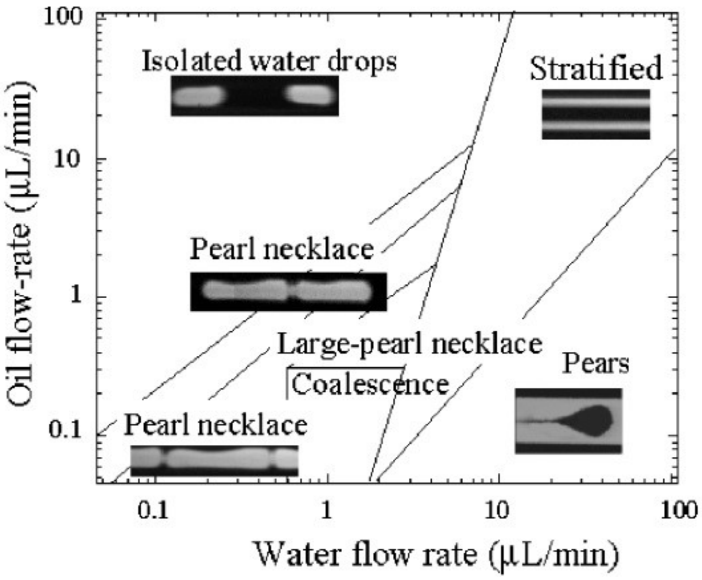

Figure 2.10. Oil-water flow patterns obtained with a T-junction[78].

The predicted size of a droplet R under external shear force is approximated by equating the Laplace pressure with the shear force between the different phases at the crossflow junction[71]:

$$R \propto \frac{\gamma_p R_{c,in}}{\mu_{cp} V_{Plug}} \propto R_{c,in} Ca^{-1} \qquad \text{Eq. 2.69}$$

where $R_{c,in}$ is the inlet channel radius of the dispersed phase. This relation holds true when droplets are introduced with a tee or cross junction that has a dimension smaller than the outlet channel dimension. In this case the droplet is small enough that the hydrodynamic forces exerted by the channel are not dominant and breakup at the squeezing point fully relies on the interaction of the shear force of the continuous flow and interfacial tension. On the other hand, when the squeezing point size is more or less comparable with the characteristic dimension of the outlet channel, wall effects are dominant over the stresses directly imposed by the flow, and the dependency of droplet characteristic size R on flow rate is much weaker giving[27,75,81]:

$$R \propto 1.34 R_{c,in} Ca^{-0.3} \qquad \text{Eq. 2.70}$$

As the liquid droplets move along the channel at constant speed, the fluid within them circulates, giving rise to counter-rotating vortices with closed streamlines. This occurs because the dispersed phase moves faster than the continuous phase, therefore a shear between the droplet and the wetting film is generated. As a result, the film is not completely stagnant because the plug exerts considerable shear stress on it, which keeps the film moving at a low velocity. However, the plug moves with a velocity v_D slightly higher than the average flow velocity $\bar{v}$. This velocity can be calculated by assuming a fully developed laminar velocity profile in the capillary[82]:

$$v_D = \frac{2}{1 + \left(\frac{R}{R_c}\right)^2} \bar{v} \qquad \text{Eq. 2.71}$$

2.4 Fundamental theory of power ultrasound and its usage on crystallization

The application of power ultrasound to industrial chemical processing (sonochemistry) is an intensification technology that has undergone serious development over the past 20 years. The type and class of materials synthesized sonochemically has become very extensive including different areas of chemical engineering: synthesis of organic and inorganic compounds[22], catalysis, polymerization and electrochemistry[83], synthesis of nanostructured materials[84] and drug crystallization[6]. The combination of ultrasound and crystallization is known as sonocrystallization. This technology offers significant improvement to the crystallization process, both in terms of controllability and product quality. As compared to the traditional silent crystallization, the use of ultrasound enhances the product quality by narrowing the crystal size distribution, lowering the mean crystal size and enhancing the nucleation rates. Moreover, a desired crystal habit and polymorphic form can be selected. When ultrasound is applied to a crystallization system, it may also influence growth rates, agglomeration and breakage, with significant influence on the crystal production. Furthermore, ultrasound seems to provide a distinct alternative to more traditional techniques of controlling the crystallization process as seeding strategies[6,85].

2.4.1 Acoustic Theory

A sound wave is a pressure disturbance that results from vibration. The two conditions that are required for the generation of a sound wave are a vibratory disturbance and an elastic medium (solid liquid or gas). The movement of the vibration body (the sound source) is communicated to the molecules of the medium, each of which transmits the motion to an adjoining molecule before returning approximately to its original position. As a result, the density fluctuations of molecules is increased. We generally refer to ultrasound (US) when the periodic vibration frequency is greater than $20\ \mathrm{kHz}$ which is beyond the normal range of hearing (Figure 2.11).

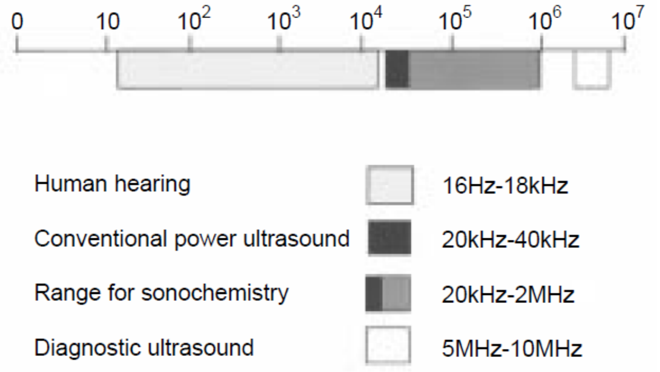

Figure 2.11. Sound frequency ranges[21].

Like other sound waves, ultrasound propagates within the medium by alternately stretching and compressing the molecular structure in a sequence of negative and positive cycles (Figure 2.12). Therefore a pressure oscillation is produced in time and space. Under the conditions of high negative pressure which is sufficiently great to destroy the attraction and pull the liquid molecules apart, the liquid is broken down to create cavitation bubbles at the rarefaction cycle. Theoretically, to produce cavitation in pure water a negative very high pressure of $10000\ \mathrm{atm}$ is required. However, the inevitable presence of air bubbles (initial nuclei) and tiny suspended particles trapped in water, reduces the tensile strength of the medium allowing the occurrence of cavitation at lower pressure[86].

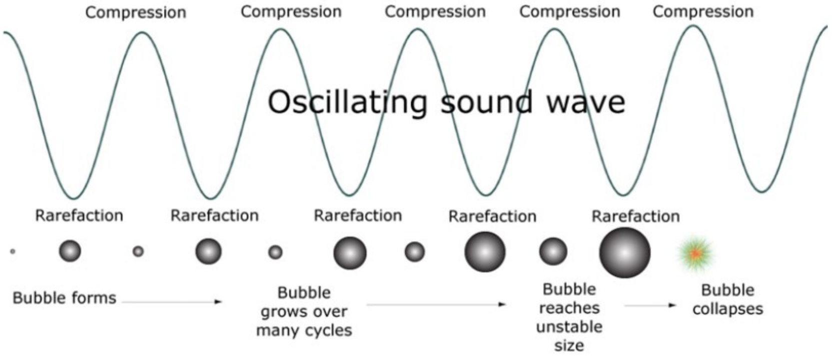

Figure 2.12. Graphical summary of the event of bubble formation, bubble growth and subsequent bubble collapse over several acoustic cycles.

The dynamics of bubble equilibrium radius with external liquid pressure can be described by considering the mechanical equilibrium between the internal bubble liquid vapor and air pressure, that tend to expand the bubble, and the external pressure and Laplace tension, that tend to compress the bubble. The Rayleigh-Plesset equation is commonly employed to model the evolution of the bubble radius with the time under the effect of an applied acoustic field within an incompressible liquid[87]. Thanks to single-bubble sonoluminescence experiments and ultra-high speed video imaging, this law has been widely validated and the physics of the single-bubble cavitation has progressed considerably. However, many aspects related to multibubble fields, remain obscure and still represent an active subject of research. The main obstacle remains the extrapolation of the known single-bubble behavior, to the macroscopically observed level which include bubble size distributions and their spatial distribution[86].

Acoustic cavitation can be regarded as a response to an externally applied acoustic pressure. In fact, it is more useful to consider cavitation as the 'mechanical activation' of a gas inclusion in a liquid by an acoustic field. In a liquid of density ρ_L, with ambient pressure P_0, a gas bubble of radius R_0 has a specific resonance frequency f_0 equal to[86]:

$$f_0 = \frac{1}{2\pi R_0}\sqrt{\frac{3\kappa P_0}{\rho_L}} \qquad \text{Eq. 2.72}$$

where κ is the polytropic index which varies between unity and the ratio of the specific heats of the gas at constant pressure and constant volume. In case of a bubble in water in ambient conditions, we may approximate to $R_0 f_0 \cong 3\ \mathrm{ms^{-1}}$. For $f_0 \cong 20\ \mathrm{kHz}$, the resonant radius is $150\ \mu\mathrm{m}$, while for $f_0 \cong 1\ \mathrm{MHz}$, it drops down to $3\ \mu\mathrm{m}$. At fairly low ultrasonic power $(1 - 3\ \mathrm{Wcm^{-3}})$ bubbles oscillate non-linearly around their equilibrium radius for several cycles and finally implode gently. This phenomenon is known as *stable cavitation*. Whereas, at high ultrasound power (higher than $10\ \mathrm{Wcm^{-3}}$), bubbles expand through a few acoustic cycles to a radius of at least twice their initial size. When a cavitation bubble is overgrown, it no longer absorbs sound energy as the elastic energy has exceeded the state that it can sustain and experience a violent collapse. This second mechanism is known as *transient (or inertial) cavitation*[86]. Both stable and transient cavitation generate pressure waves. However, the violence of the collapse of a transient cavity produces much larger pressures than those associated with stable cavitation. In fact, bubble collapse in liquids results in an enormous conversion of the kinetic of liquid motion into localized heating and pressure. These high spots of temperatures $(ca. 5000\ \mathrm{K})$ and pressures $(ca. 1000\ \mathrm{atm})$, combined with extraordinarily rapid cooling $(ca. 10^{10}\ \mathrm{Ks^{-1}})$ and light emission (sonoluminescence), provide a unique means for driving chemical reactions under extreme conditions[88,89].

By lowering the ultrasonic power densities below the cavitational threshold, the transient pressure field induces a stationary motion within the fluid known as *acoustic streaming*. This occurs when an acoustic wave propagating in a fluid gives rise to a time-dependent movement of the fluid. This phenomenon enhances macromixing and indirectly molecular mass transfer[90].

2.4.2 Generation of power ultrasound

Ultrasonic bath systems and sonoprobe systems are the two main types of laboratory ultrasound generators normally employed in sonochemistry. The ultrasonic bath is the most popular and cheapest apparatus with the common commercial frequency of $40\ \mathrm{kHz}$. It provides a low intensity of ultrasound power as compared with the probe system and is difficult to monitor and control the fluid temperature. Generally, sonochemical reactions are performed in a vessel immersed in the sonicated medium within the ultrasonic bath. The bath itself can be used as the reactor, but flammable, corrosive and volatile reagents are hence not allowed. Another disadvantage of the ultrasonic bath is that they usually have no vapor-tight lids which limits their application in reactions require inert atmosphere or reflux condenser[91]. On the other hand, the ultrasonic probe device is the alternative ultrasound generator which offers higher intensity of ultrasound and therefore considerable advantage in performing sonochemical reactions. Sonoprobes are very easy to use and fit with different vessel geometries. They are more flexible enabling adjustable power control as well as variable frequency. However, the sonoprobe system usually has the problem of probe tip erosion and the characterization of the cavitating bubble distributions is very difficult[91].

An ultrasonic processor transforms electrical energy into mechanical. Electromechanical transducers are normally implemented to convert electrical signals into mechanical energy in the form of oscillation of a *piezoelectric crystal*. This mechanical energy is converted into acoustical energy in the form of acoustic waves that propagate through the medium causing streaming and cavitation. The latter is responsible of the extreme high level of energy released into the liquid which is therefore dissipated into heat. This energy cascade of complex energy conversion allows one to measure acoustic power by measuring the dissipated heat. Thermal methods are quite reliable and are currently the most common adopted in the literature[92].

2.4.3 Literature review of sonocrystallization from solution

Crystallization is usually considered in terms of the two fundamental processes of nucleation and growth. Although these two stages occur sequentially, the very small scale of monomers self-assembling and the very short time scale of nuclei formation make these processes difficult to decouple for fundamental investigations[40]. For the similar reason, the experimental study of the different types of nucleation such as primary or secondary and homogeneous or heterogeneous results particularly demanding. Primary nucleation analysis has progressed considerably in the recent years due to small-angle and wide-angle X-ray scattering for the structural evaluation of a nucleation phase. Molecular resolution atomic force microscopy imaging has been employed to monitor phase transitions of the protein glucose isomerase proving that crystals are formed classically[93]. Recently evidence of multi-step nucleation pathways have been observed for the nucleation of Fe-O-Al from melt which may also be extended in nucleation and crystallization from solution[94]. Despite these results, the analysis of the early stages of nucleation is still unclear and there is scope for debate on the limits of the validity of the Classical Nucleation Theory[95]. In this regard, several attempts to modify the CNT have been done and ‘non-classical’ nucleation models such as the two-step mechanism have been introduced[96]. This model considers the crystalline order preceded by the separation of a dense disoriented liquid phase. Molecular-dynamics simulation is another alternative tool to provide insight into nucleation at the molecular scale. However, these simulations have to face an important problem: nucleation is a typical example of a rare event occurring on a timescale that is much longer than what atomistic simulations can typically afford[97].

Considering the significant challenges in getting more insight into the basics of crystallization, the addition of another parameter (ultrasound) makes the whole process understanding even more difficult. Research in sonocrystallization has been conducted almost experimentally and industrially orientated using large batch stirred vessels and cooling as main method to achieve the desired supersaturation. For instance, sonocrystallization improvements have been reported for different organic compounds such as adipic acid, aspartame, paroxetine, amino acids, paracetamol, accutane and sodium-thyroxine and fenoterol HBr[6]. In this section, a literature review of the research into power ultrasound effects on various aspects of crystallization from solution is given in details.

- *Effect of power ultrasound on primary nucleation*

Primary nucleation is highly affected by the application of power ultrasound. The experimental determination of metastable zone width and induction times are two traditional strategies adopted to measure primary nucleation and quantify the effect of ultrasound. Lyczko et al. (2002) investigated the effect of ultrasound on cooling crystallization of potassium sulphate solution in a batch reactor[11]. Results indicated that, especially at low supersaturation, ultrasound increases significantly primary nucleation rates. Using the classical nucleation theory, the authors concluded that this is due to a reduction of the activation energy and therefore of the critical radius of stable nuclei. Castro et al. (2007) reported similar results for the sonocrytallization of K_2SO_4/water system showing a dramatic reduction of induction period and metastable zone width[8]. The impact of ultrasound on $BaSO_4$ nucleation was analyzed by Guo et al. (2005). The study suggested that diffusion acceleration is the main reason for the reduction of induction time and metastable zone width[10]. An alternative mechanism was proposed by Wohlgemuth et al. (2009) and Wohlgemuth et al. (2010). In their work the authors assumed that nucleation is induced by the cavitating bubble surface which acts as nucleation site for heterogeneous nucleation. To prove this assumption, silent gassing experiments were compared with sonocrystallization experiments to induce adipic acid nucleation during batch cooling[9,98]. Research on the effect of ultrasound on nucleation has progressed in the recent years also considering different crystallizing systems[14,33,99]. Nowadays, the majority of researchers agree that ultrasound exhibits a positive effect on crystallization by inducing primary nucleation in the solution allowing nucleation to occur at much lower supersaturation levels[6,22].

Although the positive consequence of ultrasound in shortening the induction times and accelerating the crystallization process, some exceptions are reported in literature. In this regard, an opposite phenomenon was revealed by Miyasaka et al. (2006) for the sonocrystallization of acetylsalicylic acid. In their first study the authors demonstrated that ultrasound irradiation increases the average number of crystals. However, at a low level of ultrasonic energy it decreases the average number of crystals inhibiting nucleation[12]. In a second study, the same authors proposed a relationship between the energy necessary to form a stable nucleus, $W(n^*)$, and the ultrasonic energy at which the ultrasound exhibits an improved effect. As the two variables are directly proportional, it is considered that ultrasonic energy supplies the energy required for primary nucleation[13]. A similar behavior is also confirmed by Kurotani et al. (2009) in the sonocrystallization of some amino acids[100].

The majority of researchers agree that the effect of ultrasonic waves during nucleation is not due to the sound waves directly but to the consequence of cavitation. The dominant theory in explaining the effect of sonication is the *hot spot cavitation theory*. This is based on the heat generation associated to the compression of a gas. The rapid compression of gas and vapor during a cavitational collapse leads to nearly adiabatic heating of the content of the bubble, because thermal transport is slower than the collapse. Thus, a short lived, localized hot-spot is formed. However, the physical mechanism of how such local and transient energy concentrations correlate with nucleation events have not yet been fully explained[88].

The first attempt to relate the collapse pressure of the cavitating bubbles with the nucleation rate was made by Virone et al. (2006)[24]. The authors designed a novel reactor where the ultrasound pressure was well-defined and tried to establish the relationship between cavitation and nucleation events based on the assumption that the nucleation rate is a function of the collapsing pressure of cavitating bubbles. However, the measured and calculated induction times did not match. This could be caused by the low sensitivity of the instrument or by the uncertainties in the assumptions made. Subsequently Dodds et al. (2007) and Grossier et al. (2007) discussed the effects of ultrasound on the production of $BaSO_4$, K_2SO_4, TiO_2 crystals and presented a new possible mechanism known as *segregation theory*[101,102]. An inertial bubble is theoretically able to segregate large molecules or nanoparticles from a host liquid of different density. A species denser than the liquid is depleted on average at the bubble wall and largely over-concentrated during a very short time at the end of the bubble collapse. In the case where the species is a solute in a metastable equilibrium state, segregation may enhance the attachment of solute molecules to form clusters, and therefore increase the nucleation kinetics. The segregation theory gained further consideration after the crystallization experiments performed by Harzali et al. (2011) on $ZnSO_4 \cdot 7H_2O$[103]. Although its solubility is pressure-independent, the induction time is drastically reduced by ultrasound and the pressure effect alone can not explain all experimental results. Instead, the authors showed that an interpretation by the segregation theory remains semi-quantitatively plausible.

- *Effect of power ultrasound on secondary nucleation*

Only a few works are dedicated to the effect of ultrasound on secondary nucleation. The experimental complexity in decoupling the occurrence of primary nucleation from secondary nucleation makes this research subject difficult to approach. Hickling (1965) first investigated secondary nucleation on a single component system using ice water nucleation as a selected case of study. The author stated that cavitation can fragment ice crystals and therefore produce secondary nuclei[104]. Only recently Chow et al. (2003) managed to detect experimentally power ultrasound inducing secondary nuclei of ice in sucrose solution[105]. Dendrites were observed to be broken into fragments at the moment of cavitational bubbles collapse. These fragments grew again in the sucrose solution to act as nuclei, inducing the formation of more ice crystals (Figure 2.13). Similar results were then obtained for pure water ice crystals[106,107]. The dendritic ice structures fragment under the influence of ultrasound, thus increasing the number of nuclei which subsequently grow giving secondary nucleation.

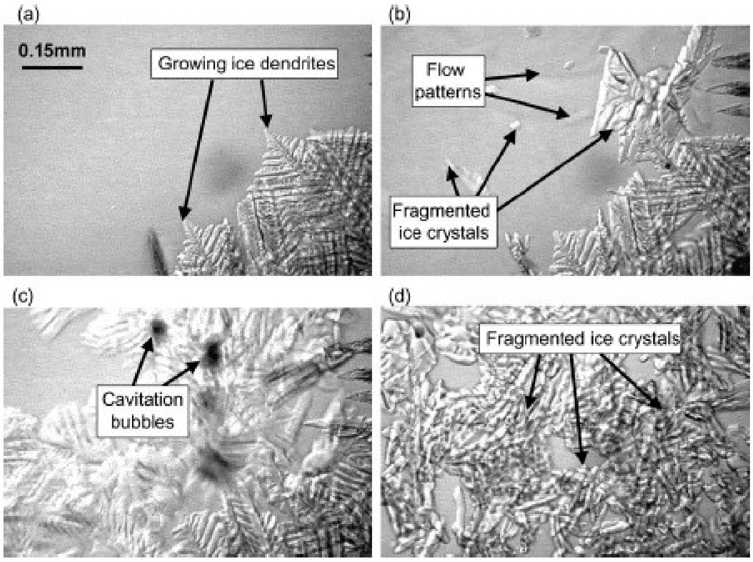

Figure 2.13. Effect of power ultrasound on the secondary nucleation of ice in sucrose solution[105].

- *Effect of power ultrasound on crystal growth*

As compared to nucleation, the effect of ultrasound on crystal growth is much less relevant and only a few works are dedicated to this subject. The majority of researchers agree that the effect of ultrasound on growth rate depends on the magnitude of the supersaturation driving force. When superstauration is low, ultrasonic irradiation almost double the growth rate. At high supersaturation, with faster growth, ultrasound appears to have less effect. Under the condition of low supersaturation levels, the quantity of available growth units in the vicinity of the crystal surface is small and bulk-phase mass transfer is rate limiting in supplying growth units to the crystal surface. Therefore the application of ultrasonic irradiation will enhance the growth rate[108,109].

- *Effect of power ultrasound on crystal agglomeration, breakage and CSDs*

The application of power ultrasound has a considerable impact on both crystal agglomeration and breakage. These processes occur simultaneously and their spatial and temporal separation is a very challenging problem. As a result, the determination of the kinetics of both mechanisms is still unknown.

Despite the interest in sonocrystallization, the effect of crystal breakage on the product of sonocrystallization experiments remains almost unexplored. Guo et al. (2007) first investigated the dispersion of inert particles of different sizes in ethanol comparing mechanical stirring with ultrasound. In their experiments, the larger particles were more sensitive to ultrasound. The authors also showed that the breakage of particles was caused by collisions between particles and by vibration and implosion of cavitation bubbles[110]. This result was then partially confirmed by Zeiger et al. (2011). In their work Aspirin suspended in dodecane was used as a model system[111]. The authors found that interparticle collisions, sonoprobe - particle collisions, and particle - wall collisions are not the major contribution to particle breakage and that direct particle - shock wave interactions are implicated as the primary pathway (Figure 2.14).

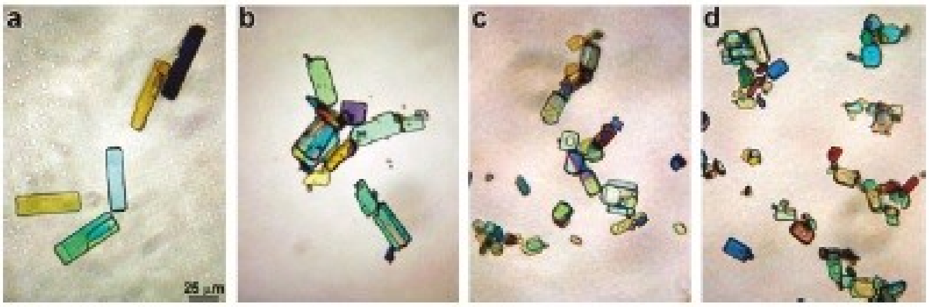

Figure 2.14. Sonofragmentation of aspirin crystals suspended in dodecane (a) before sonication, (b) after 1 min of sonication, (c) after 3 min of sonication, and (d) after 10 min of sonicaion[111]. Crystals exposed to high intensity ultrasound at 10 W and 20 kHz using a titanium horn.

Reliable evidence has shown that power ultrasound is potentially applicable in preventing agglomeration during crystallization. A reasonable explanation is that the shock wave caused by cavitation and the relevant improved mixing can shorten the contact time between crystals to an extent precluding their bonding together[6]. A recent study on the precipitation of hydroxyapatite conducted by Castro et al. (2013) in a microchannel equipped with piezoelectric actuators showed that ultrasound either prevents the formation of agglomerates or breaks up agglomerates, preventing the channel from plugging[112].

In conclusion when ultrasound is applied, the enhancement of primary nucleation rate and crystal breakage combined with the reduction of crystal agglomeration leads to the production of very fine crystals[8,9,10,33] (Figure 2.15 and Figure 2.16).

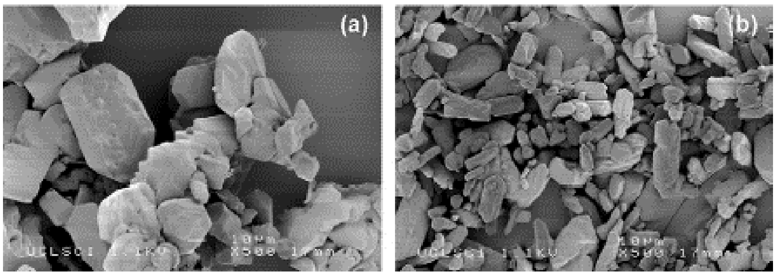

Figure 2.15. SEM photomicrograph of adipic acid crystals at steady state: (a) without sonication and (b) with sonication[33].

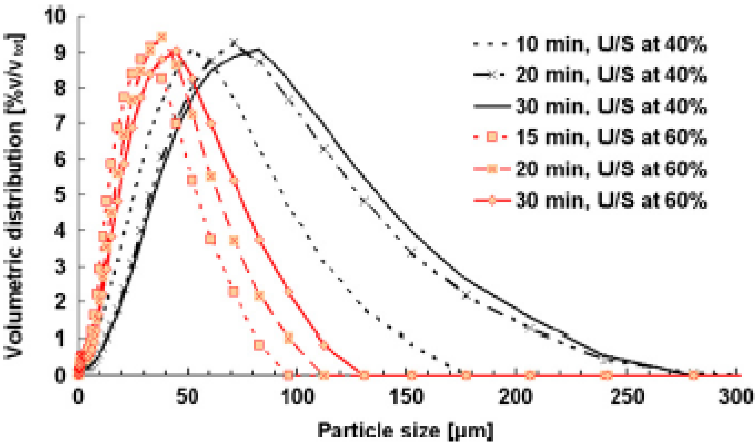

Figure 2.16. Effect of power amplitude and residence time on the adipic acid crystal size distribution[33].

- *Effect of power ultrasound on polymorphism and crystal habit*

Many pharmaceutical solids can exist in different physical forms. Polymorphism is often characterized as the ability of a drug substance to exist as two or more crystalline phases that have different arrangements and/or conformations of the molecules in the crystal lattice. The crystal polymorphism control is very important in the pharmaceutical industry because the polymorphism affects the physical and thermal properties of compounds such as the melting point, solubility, morphology, compressibility and hence the industrial handling processes and the bioavailability.

Although a lack of basic understanding regarding the link between ultrasound application and crystal polymorphism, power ultrasound has been extensively investigated in polymorphic systems as a powerful method to industrially isolate a desired crystal form. The influence of ultrasound on polymorphism has also been studied in the past decades. For example, Gracin et al. (2004) and Gracin et al. (2005) obtained the metastable β-form of p-aminobenzoic acid, which is normally impossible to produce without ultrasound, under the application of specific ultrasonic condition and supersaturation levels[113,114]. Another important study was conducted by Louhi-Kultanen et al. (2006) on the influence of ultrasound on glycine crystallization. The authors discovered that ultrasound decreased the amount of the α-polymorph at the higher temperature range ($40-50^{\circ}\mathrm{C}$), while at the lower temperature range ($20-30\ ^{\circ}\mathrm{C}$) the α form was obtained almost exclusively[115].

3. Materials, process analytical techniques and instrumentation

In this chapter, we provide the description to the chemical materials used in this research work together with the introduction of the basic principle of the analytical techniques and the main instrumentation employed.

3.1 Materials

3.1.1 Adipic acid

Adipic acid (hexanedioic acid, $(CH_2)_4(COOH)_2$, > $99.5\ \%$ pure, Sigma-Aldrich, U.K.) is the working substance selected for this research work. It is used as received without further purification. Adipic acid solutions are made using deionized water (conductivity < $0.2\ \mu S/\mathrm{cm}$). The solid density of adipic acid at $20\ ^\circ\mathrm{C}$ is $1.36\ \mathrm{g/cm^3}$ and its melting point is $152\ ^\circ\mathrm{C}$. The solubility of adipic acid in water at various temperatures is determined from the solubility curve shown in Figure 3.1, which is derived by fitting experimental data reported in the literature[1].

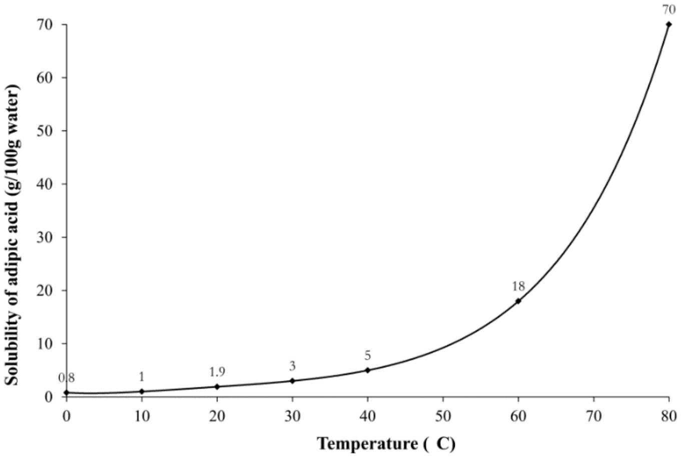

Figure 3.1. Solubility of adipic acid as a function of temperature.

The trend shows a strong dependency on the temperature above $20\ ^\circ\mathrm{C}$. For this reason, cooling crystallization from higher temperatures is the most efficient method of crystallization for this binary system.

As sketched in Figure 3.2 the compound normally crystallizes from aqueous solution as flat, slightly elongated, hexagonal, monoclinic plates[116]. The compound has been also selected due to the absence of polymorphism, which simplifies the analysis of the impact of ultrasound on crystallization.

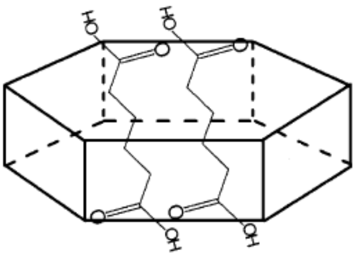

Figure 3.2. Morphology, faces, and orientation of the adipic acid molecules with respect to the faces of adipic acid crystals. The linear six-carbon chains are perpendicular to the C face so that the face is made up entirely of carboxylic group.

3.1.2 Carrier fluid

n-Hexane ($(CH_3)(CH_2)_4CH_3$ > 97 % pure, max. 0.005 % water, VHR, UK), which is insoluble in water, is used as received without further purification, and is the selected carrier fluid for generating the segmented flow and address particle fouling in microfluidics.

3.2 Process analytical techniques and instrumentation

3.2.1 Power ultrasonic instrument

The ultrasonic processor used in this work is a Cole-Parmer ultrasonic probe system with a fixed 20 kHz frequency and adjustable ultrasonic power (from 21 % to 100 % of the maximum 750 W input power). The apparatus consists of two major components: an ultrasonic power supply and converter model CP750 (Figure 3.3b) and a sonoprobe model CV33 (Figure 3.3a). The ultrasonic power supply converts 50/60 Hz voltage to high frequency electrical energy. This energy is transmitted to the piezoelectric transducer within the converter where is changed into small mechanical vibrations. These longitudinal vibrations are finally amplified by the probe and transmitted to the liquid. The probe tip has a diameter of 13 mm and is immersed within the liquid medium that has to be sonicated. The acoustic intensity of the probe is adjusted by regulating the level of the tip amplitude (as a percentage of the maximum tip displacement which is 35 μm). This percentage is given on the display and is kept constant by the generator.

Figure 3.3. Sonoprobe (a). Ultrasonic power supply and converter (b).

As mentioned in Chapter 2 the advantages of the ultrasonic probe system in laboratory scale are its high power and the ability to conveniently control energy input to the process.

3.2.2 Laser diffraction particle size analyzer

Nowadays the laser diffraction (LD) method is the most common way for the examination of the size distributions of disperse systems such as emulsions and particle systems. Generally speaking, LD technique is based on the fact that the spatial distribution of scattered light is a function of the particle size of the sample analyzed, the wave length of the light and the scattering angle of the incident light on the particle[117]. Many samples have particle sizes that extend into the submicron range creating a wider size distribution range. However, as a particle size gets smaller, the ratio of particle dimension to light wavelength is reduced. Interference effects are thus reduced and the scattering pattern becomes smoother and less angular dependent. At this smaller size range, the sensitivity of particle size to scattering intensity pattern is greatly reduced causing it to be more and more difficult to obtain correct size values.

A Beckman Coulter LS13320 single wavelength laser diffraction particle size analyzer (Figure 3.4) is employed in this work to determine the size distributions of adipic acid crystals produced in different experimental conditions. The apparatus measures the size distribution of particles suspended inside the dedicated flow cell of the machine in a carrier fluid, providing reliable and reproducible results within a particle size range of $0.017\ \mu\text{m}$ and $2000\ \mu\text{m}$.

Figure 3.4. LS13320 laser diffraction particle size analyzer.

3.2.3 High speed camera

To clearly detect crystals flowing within narrow channel geometries very high frame rates are required. To this purpose, a Photron high speed camera FASTCAM MC1 is employed in this study to capture images of moving crystals (Figure 3.5). The camera operates up to a maximum frame rate of $10000\ \text{fps}$ with a $512\ x\ 512$ maximum resolution and is coupled with a PRIOR $750\ \text{W}$ light source. Full camera operations can be performed on the PC with the control of the PFV software supplied.

Figure 3.5. Photron high speed camera FASTCAM MC1.

3.2.4 Microscopy

A standard inverted IX50 Olympus optical microscope (Figure 3.6a) and a VHX-600 Keyence digital microscope (Figure 3.6b) are the two main detection systems used in this work for the image examination of the crystals produced. The former microscope is particularly useful to be attached to the high speed camera previously described for online crystal detection at high frame rates. The later microscope is more suitable for static crystal observation.

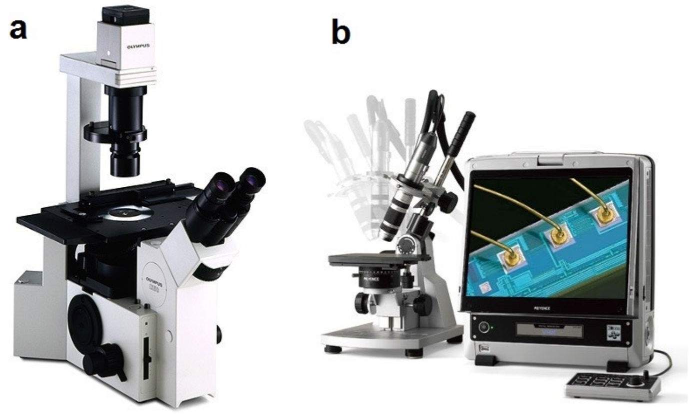

Figure 3.6. IX50 Olympus optical microscope (a) and VHX-600 Keyence digital microscope (b).

3.2.5 Syringe pump

Standard infuse/withdraw Harvard PHD 2000 programmable syringe pumps equipped with a remote controller and a multistage are the selected systems for fluid motion in microfluidics (Figure 3.7). $25\ \mathrm{mL}$ or $100\ \mathrm{mL}$ SGE glass syringes are used depending on the total volume of fluid to be pumped continuously.

Figure 3.7. Harvard PHD 2000 programmable syringe pump.

3.2.6 Peristaltic pump

A Gilson MINIPULS 3 peristaltic pump is employed in this work when dealing with particle suspension or when particularly high flow rates are required (up to $30\ \mathrm{ml/min}$).

Figure 3.8. Gilson Minipus 3 persistaltic pump.

3.2.7 Conductivity and pH meters

Electrical conductivity and pH of sparingly soluble electrolytes in water depends on concentration and temperature. Therefore, conductivity and pH measurements can be both used to monitor concentration at constant temperature. In this work a Mettler Toledo S230 SevenCompact Conductivity Meter (Figure 3.9a) and a S220 SevenCompact pH/Ion meter (Figure 3.9b) are used to monitor adipic acid desupersaturation trends over time.

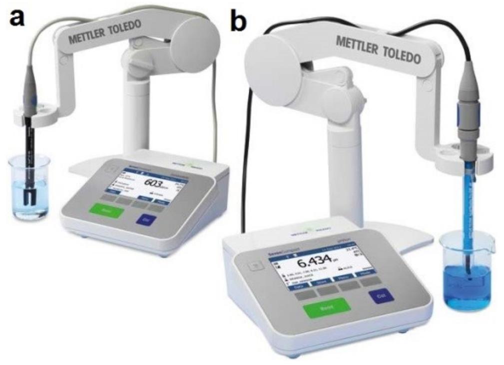

Figure 3.9. Mettler Toledo S230 SevenCompact Conductivity Meter (a). Mettler Toledo S220 SevenCompact pH/Ion meter (b).

3.2.8 Sieving machine

A typical sieving machine involves a nested column of sieves with wire mesh cloth (screen). A representative weighed particle sample is poured into the top sieve which has the largest screen openings. Each lower sieve in the column has smaller openings than the one above. At the base is a round pan, called the receiver. The column is typically placed in a mechanical shaker. The shaker shakes the column, usually for some fixed amount of time. After the shaking is complete the material on each sieve is weighed. The weight of the sample of each sieve is then divided by the total weight to give a percentage retained on each sieve. The size of the average particle on each sieve is then analyzed to get a cut-off point or specific size range, which is then captured on a screen.

In this work we employ a OCTAGON 200CL Endecotts sieving machine (Figure 3.10) to select and collect specific size ranges of crystals.

Figure 3.10. OCTAGON 200CL Endecotts sieving machine.

3.2.9 Spectrophotometer

In this work we employ a USB2000+UV-VIS-ES Ocean Optics miniature spectrometer pre-configured for general UV and visible measurements (Figure 3.11a). The system covers a wide wavelength range, from $200\ \mathrm{nm}$ to $850\ \mathrm{nm}$ and is pre-configured spectrometer with a Ocean Optics light sources DH-2000-BAL Balanced Deuterium, Halogen Light (Figure 3.11b).

Figure 3.11. Ocean Optics USB2000+UV-VIS-ES Spectrophotometer (a). Ocean Optics Light source DH-2000-BAL (b).

4. Adipic acid primary nucleation kinetics from probability distributions in droplet-based systems under stagnant and flow conditions

In this chapter, we introduce a novel capillary crystallizer that allows one to perform nucleation studies in different fluid dynamic conditions. The results obtained give more insight into the effect of mixing on primary nucleation. The material of this chapter has been featured in the following publication:

Rossi, D. et al. Adipic acid primary nucleation kinetics from probability distributions in droplet-based systems under stagnant and flow conditions. Cryst. Growth Des. 15, 1784–1791 (2015).

4.1 Introduction

All studies using microfluidics on crystal nucleation occur under quiescent conditions. Crystal detection and nuclei counting are performed in micro or milliliters droplets volumes produced by means of transparent microfluidic devices. Lab-on-a-chip (LOC) devices normally integrate one or more laboratory functions on a single unit of only millimeters to a few square centimeters to achieve automation and high-throughput crystal screening[118]. As already discussed in Chapter 2, these systems offer a lot of advantages in terms of high reproducibility and high mass and heat transfer. Despite these important benefits, microfluidic devices are normally rigid structures: once a particular chip has been fabricated, there is no possibility to make any change to its design and readapt the microchannel geometry to a new experimental condition. For instance, a parametric study which involves the change of the channel length or channel radius would require the fabrication of completely new structures for each geometrical condition leading to high experimental costs.

In this chapter, we focus on primary nucleation within droplets under both stagnant (motionless droplets) and flow (moving droplets) conditions to study if and how the mixing, generated within the droplets by the flow, affects the nucleation kinetics. To this end, we employ a versatile and flexible capillary crystallizer with a T-shaped junction for droplet generation. We control nucleation residence times by varying the length of the capillary and supersaturation by varying the temperature of the mixture. The two-phase system also permits us to avoid clogging issues, to which small channels are prone. In segmented liquid−liquid flow in small channels, as the liquid droplets move along the channel at constant speed, the fluid within them circulates, giving rise to counter-rotating vortices with closed streamlines and a pattern symmetrical about the channel axis[75,119] (Figure 4.1).

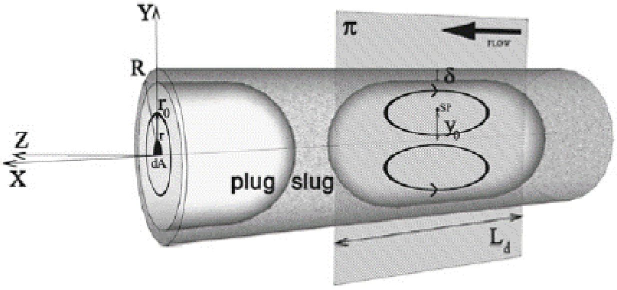

Figure 4.1. Schematic of flow patter inside a moving droplet in a microchannel.

This occurs because the dispersed phase (water) moves faster than the continuous phase (carrier fluid), generating a slip between the two phases (refer to section 4.2.1). The mixing that takes place permits us to study the primary nucleation process under different fluid dynamic conditions, not only under stagnant conditions, which one normally encounters in nucleation studies where mass transfer is dominated by molecular diffusion. We finally discuss the nucleation rates and kinetics determined experimentally by resorting to the classical nucleation theory and the mononuclear nucleation mechanism for both fluid dynamic conditions. By studying the confined fluid recirculation occurring within moving droplets, that can be considered as perfectly mixed volume behaving stochastically, we estimate the contribution of mixing on primary nucleation.

4.2 Experimental section

In this section, we describe the experimental setup and procedure employed to conduct the nucleation study described above under stagnant and flow conditions.

4.2.1 Experimental setup and procedure

We study nucleation by using liquid/liquid segmented flows in which the crystallizing aqueous solution (dispersed phase) is split into a series of droplets by hexane (continuous phase). Adipic acid solution droplets take on the characteristic capsular shape owing to the hydrophobicity of the internal capillary surface (Figure 4.2). Droplets can either completely or nearly completely fill the cross section of the channel. A thin liquid film of hexane separates them from the channel walls confining the nucleation process within the droplet volume, avoiding contact with the walls and thereby preventing clogging.

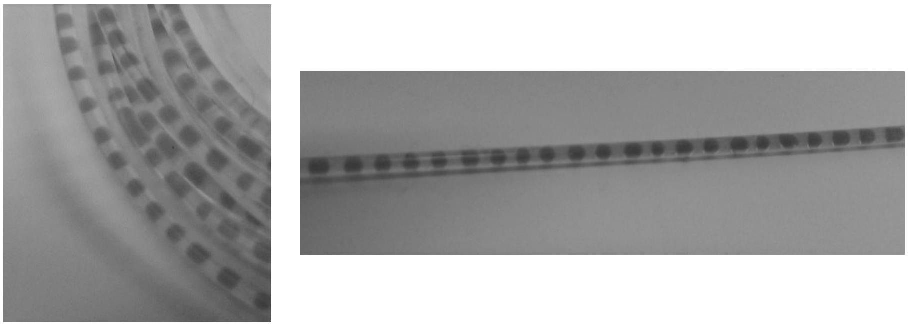

Figure 4.2. Basic blue 41 dye water solution/hexane droplet arrays in 1 mm ID PFA capillary tube.

Figure 4.3 shows the schematic of the droplet-based capillary crystallizer setup adopted for stagnant and flow experiments. The two-phase flow is obtained with PFA (perfluoroalkoxy alkanes) capillaries ($1\ \mathrm{mm}$ ID, $1.58\ \mathrm{mm}$ OD) connected to two Harvard PHD 2000 programmable syringe pumps followed by PCTFE (polychlorotrifluoroethene) filters ($2\ \mu\mathrm{m}$) and a PEEK T-junction ($0.5\ \mathrm{mm}$ ID). The pumps and T-junction are located inside a Perspex enclosure in which the adipic acid solution is kept undersaturated at temperature $T_3 =$

$30\ ^\circ\mathrm{C}$. The temperature inside the Perspex enclosure is maintained constant by a fan heater.

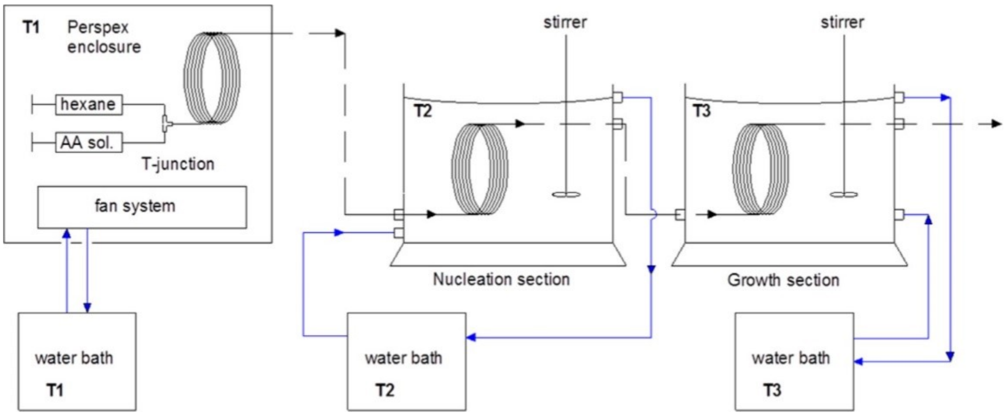

Figure 4.3. Schematic of the droplet-based capillary crystallizer setup; dashed line for flow conditions.

Under stagnant conditions, droplet arrays are generated inside the enclosure at T_1 and manually moved to the nucleation section at T_2 (to reach the desired supersaturation S) and then to the growth section at T_3 to let crystals grow to reach an observable size, at a temperature very close to the saturation limit where no nucleation occurs. The temperature history is illustrated in Figure 4.4. In this way, nucleation times could be easily set. The nucleation and growth sections are two jacketed vessels connected to different water baths; these permit setting the desired temperature. The growth time is kept constant, and $3\ \mathrm{h}$ is assumed to be sufficient for nuclei to reach a detectable size. The growth time does not affect the outcome of the experiments: the same values of the experimental probability function $P_E(t, S, V)$ defined in section 2.1.2 are found for growth times longer and shorter than $3\ \mathrm{h}$ (Eq. 2.49 and Eq. 2.50). From a statistical standpoint a sufficiently large value of M is considered to be around 100[48]. For this reason, we decide to operate with arrays of 200 droplets (that is, $M = 200$ in Eq. 2.49 and Eq. 2.50).

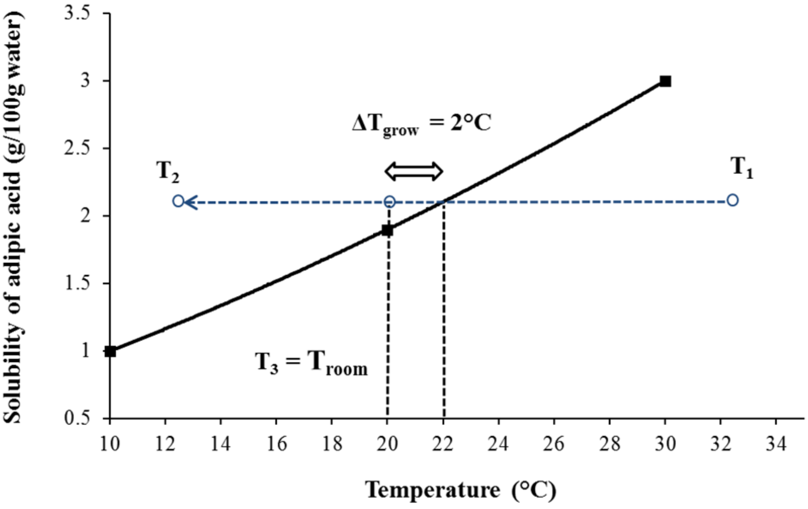

Figure 4.4. Temperature profile in droplet-based capillary crystallizer.

Crystals are detected by optical microscopy (Olympus IX50). To improve crystal detection and eliminate light reflection problems owing to the curvature of the capillary external surface, a refractive index matching device is implemented in the microscope unit. The capillary is immersed in a plastic box filled with water and fixed by guides that allows moving the capillary and passing the droplets in front of the microscope lens.

The crystals present within each droplet after $3\,\mathrm{h}$ of growth are not clearly identifiable, as they tend to agglomerate (Figure 4.5). This occurs at all the supersaturations investigated. Adipic acid normally crystallizes from aqueous solutions as flat, slightly elongated, hexagonal, monoclinic plates. It is hard, however, to clearly identify this shape when crystals are not well isolated (Figure 4.5). We should also note that the light coming from the microscope has to pass through the refractive index matching device, the wall of the capillary, and the water droplet volume; this affect the quality of the images, introducing some shadows in the background. However, these detection issues do not pose problems in our investigation, as we only need to know whether crystals are present or not in each droplet to obtain the cumulative probability function (Eq. 2.48). The crystal number and shape, as well as the structure of the agglomerates formed, are not critical aspects in our analysis.

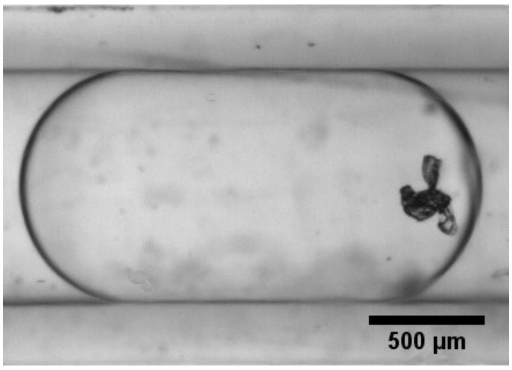

Figure 4.5. Adipic acid crystals in a water droplet.

The laboratory temperature is thermostated and fixed at $T_{room} = 20\ °\mathrm{C}$. Therefore, we choose the adipic acid solution concentration ($2.1\ \mathrm{g}$ of adipic acid per $100\ \mathrm{g}$ of water; under this condition $pH = 3$ is measured) so that the growth temperature T_3 coincides with the room temperature T_{room}. In this way, we do not have problems of crystal dissolution during the crystal detection process. T_3 is set to a temperature difference of $\Delta T_{growth} = 2°\mathrm{C}$ from the equilibrium solubility curve to make sure that no nucleation could occur in the growth section. We verify this experimentally by checking that, if we bypass the nucleation section, the value of the experimental cumulative probability function $P_E(t, S, V)$ after $3\ \mathrm{h}$ of growth at T_3 is 0.

We repeat under flow conditions the study performed under stagnant conditions, where we change the residence time of the droplets in the channel by varying the length of the capillary immersed in the nucleation unit at the temperature T_2. To generate the droplets, we use the same water/hexane flow rates ($0.3925\ \mathrm{mL/min}$ for both fluids) employed in the stagnant experiments. The droplets appear to be stable with uniform total length of ca. $2.2\ \mathrm{mm}$ and a corresponding constant volume of ca. $V = 1.5\ \mathrm{mm}^3$ (Figure 4.5). We estimate the latter by assuming that droplets have semispherical front and back sections. Once a water droplet forms, it is no longer in contact with the internal channel wall and a very thin film of liquid surrounds it. This film allows the droplet to travel at a relatively higher local velocity than the hexane slugs, and its thickness depends on the fluid system and the flow rates. A Matlab image processing program is used to measure the water droplet and hexane slug lengths, water droplet velocities, volumes of the two phases and holdup. The pictures are obtained with the Fastcam MC1 Photron high-speed camera attached to the optical microscope (Figure 4.6). The presence of a slip velocity between the two phases is confirmed by the positive water/hexane relative slip ratio ($s = 1.15$), which is calculated from the two-phase holdup as follows[120]:

$$s = \frac{velocity\ of\ water\ phase}{velocity\ of\ hexane\ phase} = \frac{\mathrm{Q_w}/\varepsilon_\mathrm{w}}{\mathrm{Q_h}/(1-\varepsilon_\mathrm{w})} \qquad \text{Eq. 4.1}$$

where Q_w and Q_h are respectively the water and hexane flow rates and ε_w is the water holdup which is the ratio between the water droplet volume and the total volume of the channel. This proves the presence of shear stress between the dispersed and continuous phases, which induces the internal recirculation within the droplets.

Figure 4.6a Figure 4.6b show respectively the droplet plug length and velocity calculated by Matlab as total plug head-bottom distance and water/hexane interface displacement between two consecutive frames. According to Eq. 2.71 the plug velocity $v_D = 18.90\ \mathrm{mm}/s$ is slightly higher than the average fluid velocity $\bar{v} = 16.66\ \mathrm{mm}/s$. This also proves the presence of a film of hexane between the capillary wall and the plug.

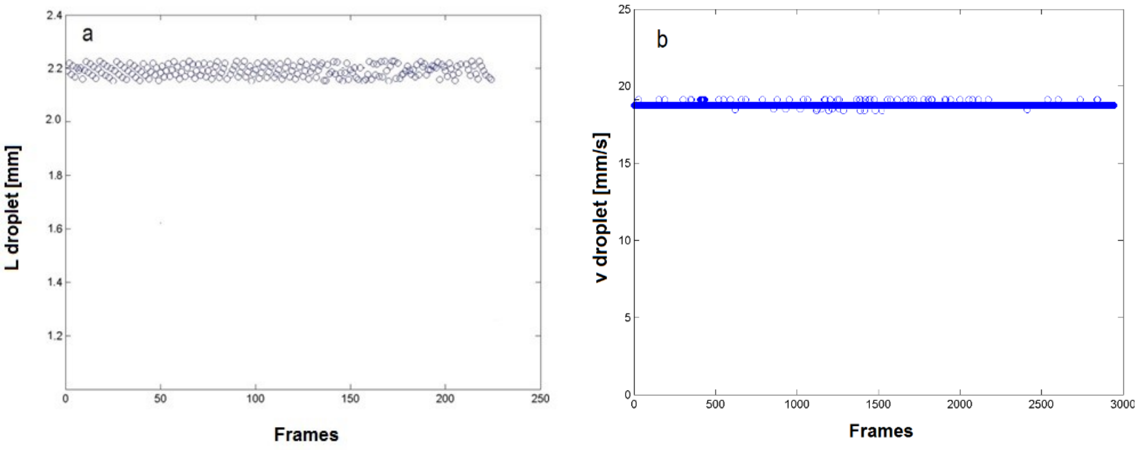

Figure 4.6. Plug head-bottom length (a) and water/hexane plug interface velocity (b).

The values of the supersaturation ratio used are $S = 2.1, 1.57, 1.39$ and 1.23 obtained by cooling the droplet arrays to $10, 12, 14, 16$ and $18\ ^\circ\mathrm{C}$, respectively. If adipic acid were significantly soluble in hexane, the values of the supersaturation ratio reported above could change owing to mass transfer of adipic acid from the drops to the slugs. To check whether adipic acid is soluble in hexane, we perform the following experiment. We add $5\,\mathrm{g}$ of adipic acid crystals to $100\,\mathrm{mL}$ of hexane in a glass beaker. We stir the mixture for $24\,\mathrm{h}$ at $30\,°\mathrm{C}$. Subsequently, we separate (by filtration) the undissolved adipic acid from the mother liquor and then we evaporate all the mother liquor. We repeat the same experiment at higher temperatures (35 and $40\,°\mathrm{C}$), but we could never collect and weigh any crystals after evaporating the mother liquor. This proves that adipic acid is insoluble in hexane. As further evidence, no crystals have ever been detected in the hexane slugs after cooling under either stagnant or flow conditions.

Under both stagnant and flow experiments, we calculate the probability function $P_E(t, S, V)$ for different nucleation times ($10, 30, 60, 90, 120, 180$ and $480\,\mathrm{s}$). Under flow conditions, these times are equal to the residence times of the fluid in the nucleation section; these are obtained by using capillary tubes of $0.167, 0.5, 1, 1.5, 2$ and $3\,\mathrm{m}$, respectively. To check the reproducibility of the results, we repeat each experiment three times, calculating mean values and standard deviations. Since the experimental procedure requires cooling the droplet arrays from the initial temperature T_1 to the nucleation temperature T_2, a time lag t^* is present for the achievement of the specific supersaturation $S(T_2)$. According to COMSOL simulations (refer to section 4.2.2), the fluid temperature reaches the constant value T_2 over a distance along the capillary axis corresponding to a residence time of $t^* = 6\,\mathrm{s}$, starting from the temperature T_1 for both stagnant and flow conditions. Supposing that no nucleation events take place during the achievement of the temperature T_2 (refer to section 4.2.2), we determine the nucleation rates by shifting the origin of the time axis by $6\,\mathrm{s}$ ($t' = t - t^*$). Hence, the rescaled residence times are $t' = 4, 24, 54, 84, 114, 174$ and $474\,\mathrm{s}$, respectively. The longest nucleation time investigated under stagnant conditions ($480\,\mathrm{s}$) is not considered in flow experiments due to the necessity to operate with a very long capillary tube (8 m), which results in pressure drops that are too high for the syringe pumps employed.

4.2.2 COMSOL simulation of temperature profile

The actual temperature profiles within the capillaries are determined by using COMSOL Multiphysics 5.0. In stagnant conditions, the result of COMSOL simulations show that after a cooling time of $6\,s$ the solution temperature is uniform over the entire cross-section of the channel (Figure 4.7a and Figure 4.7b). The simulation refers to the worst scenario in which the capillary is cooled from $T_1 = 30\ °\mathrm{C}$ to $T_2 = 10\ °\mathrm{C}$.

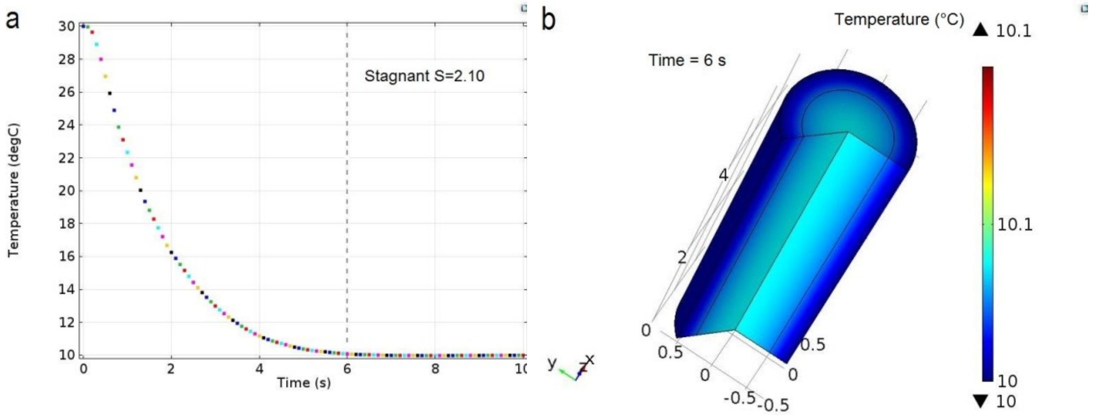

Figure 4.7. Temperature profile over the time at the capillary axis in stagnant conditions for the cooling temperature: from 30 °C to 10 °C (S=2.1) (a). Temperature map within the capillary (3D section) at time t*=6 s in stagnant conditions for the cooling temperature: from 30 °C to 10 °C (S=2.1) (b).

We perform similar simulations in flow conditions at steady state. Figure 4.8a and Figure 4.8b show the temperature profiles along the capillary axis at the different cooling temperatures employed in our experiments.

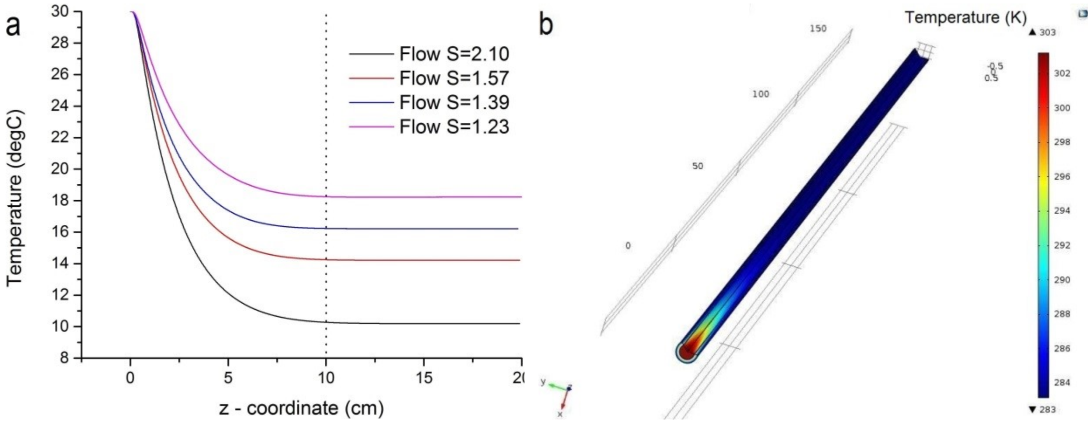

Figure 4.8. Temperature profiles along the capillary axis in flow conditions at different cooling temperature: from 30 °C to 10 °C (S=2.1), 14 °C (S=1.57), 16 °C (S=1.39) and 18 °C (S=1.23) (a). Temperature map along the capillary (3D section) in flow conditions for the cooling temperature: from 30 °C to 10 °C (S=2.1) (b).

In the worst case, for $S = 2.1$, the cooling time t^*_{flow} is still about $6\ \mathrm{s}$, being of course shorter at lower supersaturation. As we see from Figure 4.8, the temperature becomes constant after a capillary length of $L^* = 10\ \mathrm{cm}$; as the average fluid flow rate $Q = 0.785\ \mathrm{mL/min}$, we obtain $t^*_{flow} = 6\ \mathrm{s}$. The simulations in this numerical analysis refer to a simplified water single phase system; the properties and geometry of the PFA capillaries are employed. The outer-wall of the capillary is kept at constant temperature as the cooling liquid. The simulation is conducted using the Heat Transfer Module implemented in the software. The governing equations and numerical approach are described in detail in the Module Tutorial[121].

4.3 Results and discussion

4.3.1 Determination of nucleation rates

Figure 4.9 shows the cumulative distribution function for the four supersaturation levels considered under stagnant and flow conditions. As expected, the higher the supersaturation, the larger the driving force and in turn the nucleation rate. The fitting functions (performed on the mean values) reproduce very well the experimental points. This confirms that the stochastic process can be described by the Poisson model. At high supersaturation ($S = 2.1, 1.57$), nucleation rates are higher under flow conditions, while at lower supersaturation ($S = 1.39, 1.23$) the results are similar to those obtained in stagnant droplets. Moreover, the experimental error is larger at high supersaturation, especially under flow conditions. At high supersaturation there is a clear effect of flow conditions (the errors bar do not overlap), whereas at low supersaturation this difference vanishes.

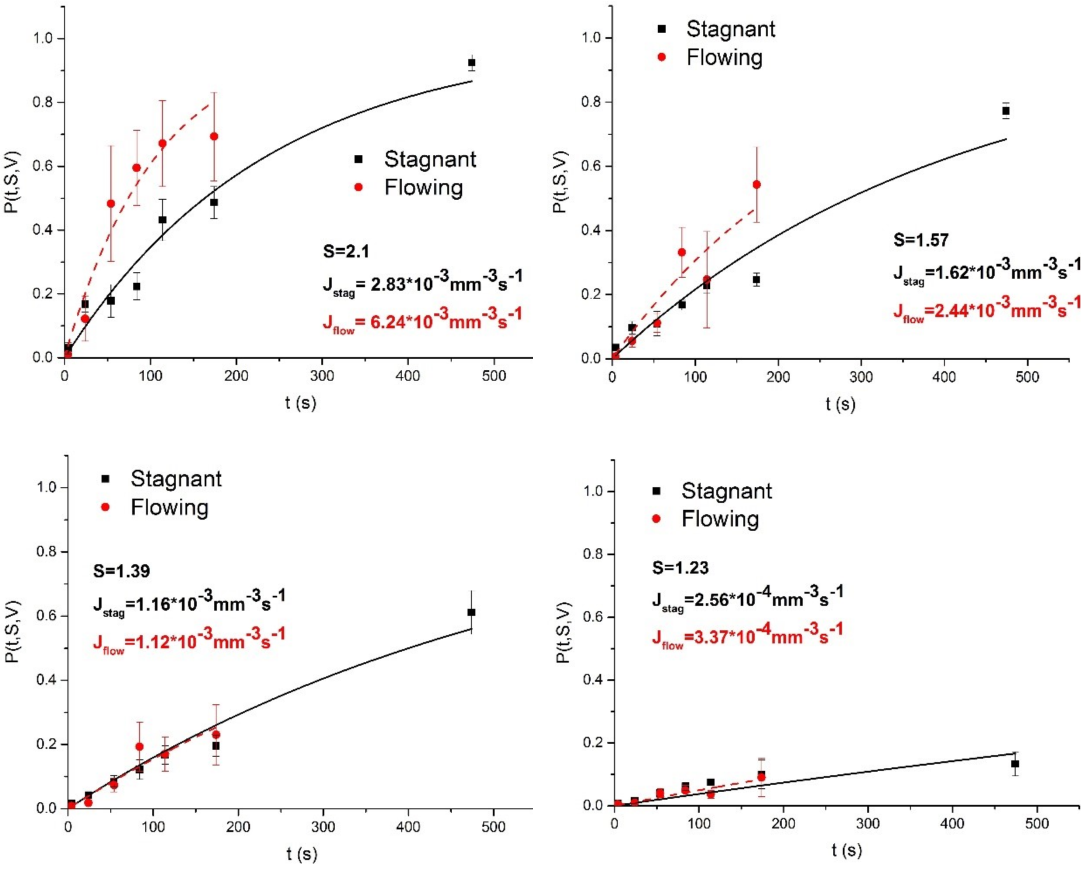

Figure 4.9. Adipic acid nucleation rate determined by fitting the experimental points of the cumulative distribution function at different residence times for various supersaturations with the theoretical cumulative distribution function. Fittings performed on the mean values around the standard deviations.

4.3.2 Nucleation parameters

The relation between the nucleation rate J and the supersaturation ratio S expressed as per Eq. 2.52 and Eq. 2.53 allows calculating the kinetic and thermodynamic parameters A and B, as described in chapter 2, by the best linear fit reported in Figure 4.10 for both stagnant and flow conditions.

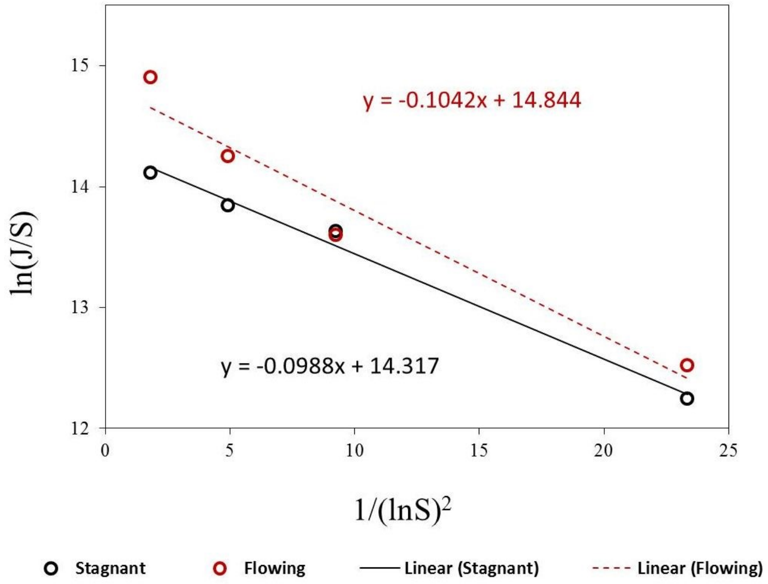

Figure 4.10. Fitting of nucleation rate equation J(S) = ASexp[−B/(lnS)^2].

After obtaining the values of A and B, we calculate the nucleation parameters given in Eq. 2.54. The results are reported in Table 4.1 and Table 4.2. To calculate the crystal-liquid interfacial energy γ for homogeneous nucleation, we adopt Mersmann's equation[38], setting the constant in the equation to 0.514, assuming a spherical nucleus[37]. Therefore, it is

$$\gamma = \frac{0.514KT}{v_o^{\frac{2}{3}}} ln\left(\frac{1}{N_A v_0 C_e}\right) \qquad \text{Eq. 4.2}$$

where C_e is the adipic acid equilibrium concentration ($68.43, 91.42, 103.73$ and $116.60\ \mathrm{mol/m^3}$) calculated at the nucleation temperatures $T_2 = 10, 14, 16$ and $18\ °\mathrm{C}$, respectively, v_0 the volume of a molecule of solute in the crystalline state calculated from Eq. 2.9 ($1.78 \cdot 10^{-28}\ \mathrm{m^3}$ for adipic acid) and c the dimensionless shape factor of the crystal that relates the surface area an object to its volume defined from Eq. 2.10.

Table 4.1. Nucleation parameters under stagnant and flow conditions.

	$J(S)$ $(10^6 \mathrm{m}^{-3}\mathrm{s}^{-1})$		A $(10^6 \mathrm{m}^{-3}\mathrm{s}^{-1})$		B		n^*		$\frac{W(n^*)}{KT}$		z		f^*C_0 $(10^7 \mathrm{m}^{-3}\mathrm{s}^{-1})$	
S	**Stag**	**Flow**	**Stag**	**Flow**	**Stag**	**Flow**	**Stag**	**Flow**	**Stag**	**Flow**	**Stag**	**Flow**	**Stag**	**Flow**
1.23	0.256	0.337	1.65	2.8	0.0988	0.1042	22.27	23.49	2.31	2.43	0.022	0.022	9.14	15.91
1.39	1.16	1.12					5.53	5.84	0.91	0.96	0.056	0.055	4.08	7.10
1.57	1.62	2.44					2.15	2.27	0.48	0.51	0.105	0.103	2.45	4.28
2.10	2.83	6.24					0.48*	0.51*	0.18	0.19	0.285	0.278	1.21	2.11

Table 4.2. Interfacial energy ratio for heterogeneous/homogeneous nucleation ($\gamma_{\mathrm{ef}}/\gamma$).

	γ_{ef} (mJm^{-2})		γ (mJm^{-2})		$\gamma_{\mathrm{ef}}/\gamma$	
S	**Stag**	**Flow**	**Stag**	**Flow**	**Stag**	**Flow**
1.23	2.23	2.27	31.13	31.13	0.071	0.073
1.39	2.26	2.30	29.71	29.71	0.076	0.077
1.57	2.27	2.31	29.10	29.10	0.078	0.080
2.10	2.29	2.33	28.54	28.54	0.080	0.082

If the data fitting of Figure 4.9 and Figure 4.10 is performed without rescaling the time axis, the values of A increase by 5 % for stagnant and flow regimes, while those of B increase by about 1 % for both regimes. This difference arises from the fact that, if we do not rescale the time axis of $6\ s$, we basically consider the cooling time as part of nucleation time and therefore the resulting nucleation rates become larger. However, in this study we are interested in understanding the difference between nucleation in flow and stagnant conditions rather than determining the exact values of nucleation rates. This difference between the two regimes is still present no matter how the fittings are performed.

4.3.3 Discussion

Using Eq. 2.54, we may express the nucleation rate in terms of the nucleation parameters reported in Table 4.1, to obtain

$$J(S) = \mathrm{z} f^{*} C_0 \exp\left(-\frac{W(n^{*})}{KT}\right) \qquad \text{Eq. 4.3}$$

For both regimes, the number of molecules in a critical nucleus n^{*} and (normalized) nucleation work barrier $\frac{W(n^{*})}{KT}$ decrease with increasing supersaturation, since it is easier to form small stable nuclei at high supersaturation levels. This is quite intuitive, as the supersaturation is the driving force of the process.

The Zeldovich factor z, which accounts for the fraction of nuclei larger than the critical nucleus of n^{*} molecules that decay and disappear rather than growing to macroscopic size (probability for a stable nucleus to redissolve), is in the typical range of $0.01 - 1^{40}$ for both stagnant and flow conditions. In this regard, we should notice that not all the nuclei that reach the critical size turn into stable crystals: the probability of the nuclei at the top of the activation energy barrier to grow into stable crystal is less than unity. The Zeldovich factor z corrects $J(S)$ by taking into account the loss of stable nuclei. This factor is introduced to compensate for the effect of detachments of monomers from cluster. These are "escaped nuclei" that do not contribute to nucleation and thus reduce the nucleation rate[37].

In case of homogeneous nucleation (HON), experimental estimations of A are generally on the order of $10^{26} - 10^{30}\ \mathrm{m^{-3}s^{-1}}$, whereas for heterogeneous nucleation (HEN) A an assume values that are several orders of magnitude lower[48,40].

The A values that we measure in our experiments are $A_{stag} = 1.65 \cdot 10^{6}\mathrm{m^{-3}s^{-1}}$ and $A_{flow} = 2.8 \cdot 10^{6}\mathrm{m^{-3}s^{-1}}$. This suggests that heterogeneous nucleation should be the dominant nucleation mechanism. Accordingly, the low values of the heterogeneous crystal-liquid interfacial energy γ_{ef} in comparison to the homogeneous crystal-liquid interfacial energy γ results in low values of $\gamma_{\mathrm{ef}}/\gamma$

for stagnant and flow conditions (Table 4.2). This confirms the dominant HEN mechanism for both regimes. The $2\ \mu\mathrm{m}$ filters employed to pretreat the adipic acid solution ensure no impurity particles larger than $2\ \mu\mathrm{m}$ are present but do not eliminate all foreign particles.

As nucleation is easier to achieve under heterogeneous conditions in comparison to homogeneous, one may expect that $A_{HEN} > A_{HON}$. This, however, does not have to be, because the nucleation rate $J(S)$ strongly depends on the exponential term of Eq. 4.3 and therefore on the thermodynamic factor B that appears in it. $J(S)_{HEN}$ can be larger than $J(S)_{HON}$ even if $A_{HEN} < A_{HON}$ as long as B_{HON} is considerably larger than B_{HEN}. This is what happens in our case: the nucleation rates $J(S)_{HEN}$ are orders of magnitude higher than the corresponding homogeneous rates evaluated considering the theoretical value of B calculated from the equation

$$B = \frac{4}{27}\frac{c^3 v_0^2 \gamma^3}{(KT)^3} \qquad \text{Eq. 4.4}$$

where γ is given in Eq. 4.2. The values obtained are $B_{HON} = 219$, $B_{HON,stag} = 0.0988$ and $B_{HON,flow} = 0.1042$, which result in $J(S)_{HEN} \gg J(S)_{HON}$.

Narducci et al. (2012) investigated the nucleation rate of adipic acid in a continuous cooling crystallization process conducted in a stirred crystallizer (MSMPR)[122]. This is a large, and accordingly deterministic, system; thus, to model the process, the authors used a population balance equation. To derive nucleation rates, they fitted the crystal size distribution in the stream, leaving the crystallizer obtained numerically with that measured experimentally. The shapes of the distributions reflect the effect not only of primary nucleation but also of secondary nucleation, breakage, and agglomeration. These mechanisms are difficult to consider separately when one adopts a deterministic approach, and so one ends up with a “global” nucleation rate, which combines primary and secondary nucleation. Conversely, the stochastic method adopted in this work allows considering only primary nucleation, as we discussed in chapter 2. Thus, the higher values of nucleation rates $(10^{11} - 10^{12}\mathrm{m}^{-3}\mathrm{s}^{-1})$ found by Narducci et al. (2012) in comparison to our values are not surprising[122]. Such a difference is most probably due to the large occurrence of secondary nucleation and breakage in the MSMPR crystallizer promoted by the shear created by the stirrer and the vigorous fluid mixing.

Our results indicate that the flow conditions do not have a significant effect on the thermodynamics of the nucleation process, increasing the B parameter only from 0.0988 to 0.1042 and consequently leading to very small differences in the other parameters such as n^*, $\frac{W(n^*)}{KT}$, z, and γ_{ef}. This is reasonable, as these variables have a thermodynamic origin and are unrelated to flow. Moreover, as the calculated variation of B from stagnant to flow is about $5\ \%$, which is within the experimental error, we conclude that the internal droplet mixing does not affect the thermodynamic parameter B at all. We should note that the values of n^* obtained for $\mathrm{S} = 2.1$, reported in Table 4.1 (followed by an asterisk), are lower than unity; this implies that stable nuclei are formed by less than one molecule. This result makes no physical sense and has to be discarded. The reason for this is that the classical nucleation theory applies solely to nuclei of large enough size (more than a few molecules). When the value of n^* approaches unity, one needs to resort to the atomistic model of nucleation to calculate the values of n^*[37]. In the latter, the critical nucleus size has a discrete character, not being a continuous function of the supersaturation ratio. Supersaturation ranges are present in which the size of the critical nucleus is invariant. In such a model, the number of molecules in the critical nucleus can vary only discretely and can not be less than unity.

Different conclusions arise from the analysis of the A factor, which accounts for the kinetics of the nucleation process. While the flow conditions do not affect the thermodynamics of the process, a remarkable variation is observed for the A factor, which changes from $1.65 \cdot 10^6 \mathrm{m}^{-3}\mathrm{s}^{-1}$ (stagnant conditions) to $2.8 \cdot 10^6 \mathrm{m}^{-3}\mathrm{s}^{-1}$ (flow conditions). A difference of more than $30\ \%$ can not be related to experimental error and consequently can be only explained by a change in the kinetics of nucleation. Experiments show that $J(S)_{flow}$ is larger than $J(S)_{stag}$ and this gap arises from the pre-exponential term zf^*C_0 and in particular from the product f^*C_0, which accounts only for the kinetics of the process. In fact, as the Zeldovich factor remains constant in both regimes, the term f^*C_0 dominates in flow conditions, making $J(S)_{flow}$ exceed $J(S)_{stag}$. Therefore, we may hypothesize that the recirculation present within the droplets in flow conditions[119] increases $J(S)$ by enhancing the attachment frequency f^*. This increases because convection renders the flux of monomers toward the nucleus surface larger. This hypothesis is supported for example in the case of capillary liquid-liquid reactions by the enhancement of mass transfer coefficients registered at high slug flow velocities[123] or mechanical mixing[42]. The enhancement of mass transfer is interpreted in terms of internal circulation flow within the plugs, a conclusion corroborated by experimental and CFD calculations[124,125]. The attachment frequency f^* has been determined theoretically for spherical nuclei and HON in diffusion-controlled processes with less concentrated solutions (Eq. 2.24) and interface-controlled processes with highly concentrated solutions (Eq. 2.26). The resulting formulas show a direct proportionality between f^* and the monomer diffusion coefficient D ($f^* \propto D$). As mentioned in chapter 2, the theoretical determination of f^* when nucleation occurs on a substrate (HEN) is still a problem under investigation owing to the inhomogeneity of the concentration field around the foreign substrate, which complicates the calculation of the monomer flux. This makes it difficult to estimate f^* in our case, because under both flow and stagnant conditions the nucleation mainly occurs heterogeneously. We can not even calculate f^* experimentally from the known product f^*C_0, since in heterogeneous nucleation we can not estimate the concentration of nucleation sites C_0 in the system. This problem does not arise in HON, where one assumes that each molecule in the solution gives a nucleation site from which a nucleus can grow and possibly become stable (so that $C_0 = {}^{1}\!/_{v_0} \cong 10^{11} - 10^{12}\mathrm{m}^{-3}$). This also explains why A is much higher in HON than in HEN, as the concentration C_0 tends to be considerably higher in the case of HON than in HEN.

We conclude that mixing tends to enhance the nucleation rate by increasing the mass transfer of monomers toward the surface of the forming nucleus. This is reflected by a rise in the attachment frequency f^*. The recirculation within the flowing droplets does not affect the thermodynamics of primary nucleation, as the enhancement of f^* is not accompanied by a drop in the nucleation work barrier represented by the B factor.

The recirculation patterns inside the droplets do not always cover the entire droplet volume: the patterns depend on the mixture velocity and capillary cross-section profile[119]. This fluid dynamic inhomogeneity within the droplet samples, due to the presence of stagnation and mixed areas, may explain the larger spread of values observed in flow experiments. Moreover, the small difference in $J(S)$ values at low supersaturation ($S = 1.39, 1.23$) between stagnant and flow conditions could be due to the fact that recirculation within the droplets may not play a significant role when the cluster concentration is relatively low.

The validity of the values of the nucleation rate parameters reported in this study is guaranteed only within the ranges of supersaturation ratio and operating conditions considered. We expect that they should also be valid outside these ranges, provided the nucleation mechanism remains the same. As was said, in our experiments we opted to work at low temperature because this allowed us to control the temperature better during the counting process. This was performed at a temperature (T_3) that is close to room temperature (T_{room}) and was in a part of the metastable zone where no nucleation takes place (refer to section 4.2.1).

4.3.4 Stochastic model validation

As reported in section 4.2.1, in calculating the values of the function $P_E(t, S, V)$, we assume that no nucleation occurs whilst the adipic acid solution is cooled from the temperature T_1 to the desired nucleation temperature T_2. In this section, we intend to support this assumption. To this end, we compare the values of the calculated cooling times $t^* = 6\ \mathrm{s}$ (refer to section 4.2.2) and the mean nucleation induction time τ_{mean} (Eq. 2.56), for both stagnant and flow conditions. Our assumption is acceptable if:

$$t^* \ll \tau_{mean} \qquad \text{Eq. 4.5}$$

At the largest supersaturation ratio considered ($S = 2.10$), the nucleation rates for stagnant and flow conditions are equal to $J(S = 2.1)_{stag} = 2.83 \cdot 10^{-3}\,\mathrm{mm^3 s^{-1}}$ and $J(S = 2.1)_{flow} = 6.24 \cdot 10^{-3}\,\mathrm{mm^3 s^{-1}}$, respectively; for droplets of volume $V = 1.5\,\mathrm{mm^3}$, the corresponding mean nucleation induction times are equal to $\tau_{mean,stag} = 3.92\,\mathrm{min}$ and $\tau_{mean,flow} = 1.78\,\mathrm{min}$. For both stagnant and flow conditions, the requirement in Eq. 4.5 is met; our assumption is thus legitimate.

In section 2.1.2 we discussed the criteria for the applicability of the mononuclear nucleation mechanism (MNM) to the stochastic primary nucleation analysis. According to Eq. 2.57, the mononuclear approach employed in this study is legitimate if

$$\tau_g \ll \tau_{mean} \qquad \text{Eq. 4.6}$$

which is equal to

$$\frac{(\alpha_V V)^{\frac{1}{3}}}{G} \ll \frac{1}{J(S)V} \qquad \text{Eq. 4.7}$$

Assuming a typical value for the crystal volume at detectable size over the parent phase volume $\alpha_V = 10^{-4}$ and a rather high growth rate $G = 1\,\mathrm{\mu m s^{-1}}$[126], a growth time $\tau_g = 0.89\,\mathrm{min}$ is calculated. For both stagnant and flow conditions, the requirement in Eq. 4.7 is met; therefore the MNM is applicable.

4.4 Conclusions

We derived crystal primary nucleation kinetics by probability distribution functions under stagnant (motionless droplet) and flow (moving droplet) conditions, determining nucleation rates, kinetic and thermodynamic parameters, and characteristic nuclei parameters using the mononuclear nucleation mechanism and the classical nucleation theory. The results indicate that the nucleation of the adipic acid solution occurs predominantly by a heterogeneous mechanism in both cases. The mixing patterns achieved inside the moving droplets accelerate the nucleation rates $J(S)$. This is due to the enhancement of the attachment frequency by the increase of the flux of monomers toward the nucleus surface by convection. The evaluation of the thermodynamic factor B for both regimes and related parameters demonstrate that flow conditions do not promote primary nucleation (they do not lower the nucleation energy barrier). The evaluation of the effective crystal-liquid interfacial energy γ_{ef} over the theoretical homogeneous crystal-liquid interfacial energy γ determined for both regimes demonstrates the dominance of heterogeneous nucleation over homogeneous nucleation in both circumstances.

5. Continuous flow sonocrystallization in droplet-based microfluidics

In this chapter, we perform nucleation studies under the effect of ultrasound employing the droplet-based capillary device introduced in the previous chapter. The system allows one to perform basic studies on the effect of different ultrasound conditions on primary nucleation as well as running continuous flow sonocrystallization of adipic acid in microchannel for pharmaceutical production.

The material of this chapter has been featured in the following publication:

Rossi, D. et al. Continuous-Flow sonocrystallization in droplet-based microfluidics. Cryst. Growth Des. 15, 5519–5529 (2015).

5.1 Introduction

One of the main problems in the sonocrystallization research is to find a method to separate and analyze the contribution of bubble collapse from the contribution of mixing produced by acoustic streaming on primary nucleation. As mentioned before, the two phenomena occur very quickly on a small spatial scale that the physical decoupling of both mechanisms and their experimental investigation is practically impossible. This is particularly true in large geometries. To overcome this problem, in this chapter we attempt to calculate nucleation rates and nucleation kinetics applying the stochastic method adopted in chapter 4 with the only difference that here the droplets are exposed to a specific ultrasonic field. The designed droplet-based capillary sonocrystallizer is suitable for studying the effects of specific ultrasonic conditions on crystallization, because of the flexibility that the setup offers in adjusting the distance between the ultrasonic source and the small portion of the sonicated solution, in contrast to fixed geometries where the ultrasonic conditions are not adjustable[127]. The specific pressure field inside the capillary is calculated by means of numerical simulation. This allows the estimation of the possibility of cavitation and relating it to sonocrystallization. Evidence of cavitation is also provided by observing the occurrence of sonoemulsification[128] as well as by detecting the presence of sonochemiluminescence[129].

In addition, the designed droplet-based setup is suitable to obtain better control of crystal size by running for the first time cooling crystallization in a compact experimental unit that combines continuous flow in microchannel and ultrasound technology. Cooling crystallization of adipic acid from aqueous solution is the selected case study, and hexane, used as main carrier fluid, is employed to generate the segmented flow pattern required to overcome clogging issues. The effect of supersaturation and ultrasonic power in a confined tubular geometry on crystal size, crystal size distribution, and crystal production are investigated. To this end, a filtration protocol is developed for separating hexane and water from the crystals formed within the droplets.

5.2 Experimental section

In this section, we describe the experimental setup and procedure employed to run continuous flow sonocrystallization experiments in a droplet-based capillary device.

5.2.1 Experimental setup and procedure

Figure 5.1 shows the schematic of the droplet-based capillary sonocrystallizer used in this work. The segmented flow was successfully employed in chapter 4 to prevent clogging in a hydrophobic tubular geometry. The droplets are generated in the first stage at temperature T_1 using the same approach already described in chapter 4. Flow rates of $0.3925\ \mathrm{mL/min}$ are used for both fluids.

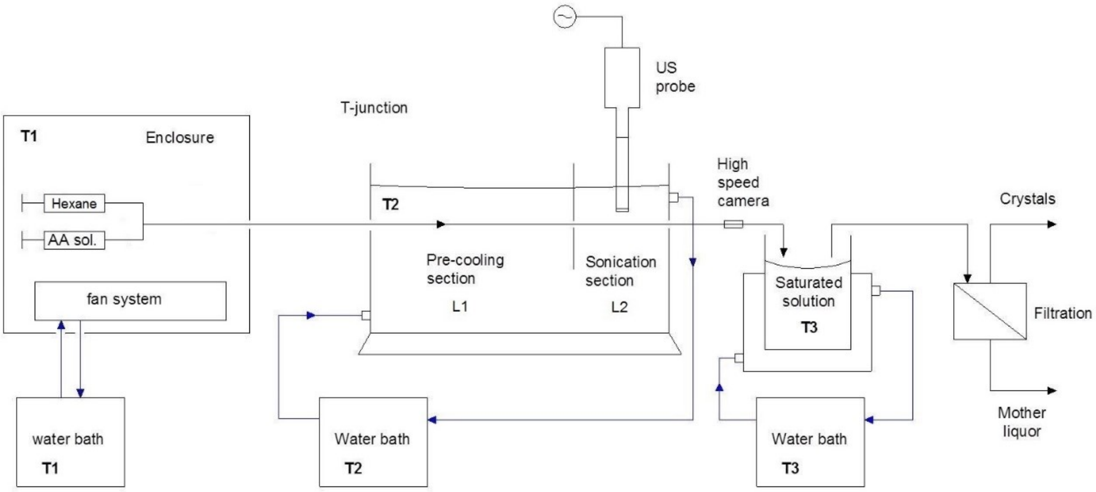

Figure 5.1. Schematic of the droplet-based capillary sonocrystallizer setup. Solution maintained in understaurated condition at T_1. Solution flows in the pre-cooling section L_1 = 15 cm at T_2 to reach the desired supersaturation. Solution flows in the sonicated section L_2 = 10 cm at T_2. Crystals collection in saturated solution at T_3 and final crystals filtration.

According to the thermal path illustrated in Figure 5.2, the droplets move from temperature T_1 to temperature T_2 to reach a specific supersaturation. The initial adipic acid concentration is 2.12 g per 100 g g of water, which is the saturation concentration at room temperature ($22\ °\mathrm{C}$). Six cooling temperatures are employed, $T_2 = 6\ °\mathrm{C}, 8\ °\mathrm{C}, 10\ °\mathrm{C}, 12\ °\mathrm{C}, 14\ °\mathrm{C}$ and $16\ °\mathrm{C}$, corresponding to supersaturations of $S = 2.62$, $S = 2.39$, $S = 2.12$, $S = 1.86$, $S = 1.63$ and $S = 1.42$, respectively.

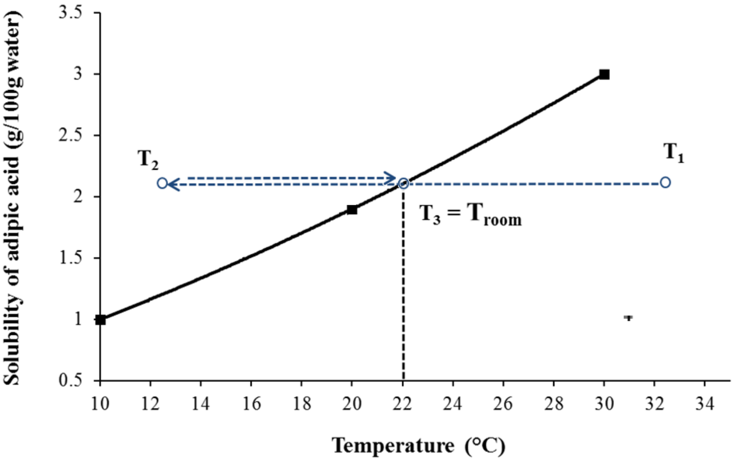

Figure 5.2. Temperature profile in the various stages of the droplet capillary sonocrystallizer.

The capillary is horizontally aligned within a Perspex container ($L = L_1 + L_2 = 25\ \mathrm{cm}$), $W = 20\ \mathrm{cm}, H = 25\ \mathrm{cm}$). To keep the capillary perfectly horizontal, two threads are made in the center of the lateral walls of the container, and the capillary is tightened between two opposite male nuts (Figure 5.1). The Perspex container is divided in two communicating chambers and filled up with cooling water at T_2 which recirculates through a second water bath. The first chamber has a length $L_1 = 15\ \mathrm{cm}$ and works as a precooling section. The length L_1 is fixed taking into account the temperature profiles along the capillary which are calculated using numerical simulation (refer to section 5.2.2).

Ultrasound is applied by fixing the ultrasonic probe ($750\ \mathrm{W}$ ultrasonic processor, frequency = $20\ \mathrm{kHz}$ and amplitude = $21\ \%$) after the precooling section in the middle of the sonication section (of length $L_2 = 10\ \mathrm{cm}$). The center of the $13\ \mathrm{mm}$ circular flat sonoprobe tip is horizontally aligned to the capillary using an adjustable stage holder that allowed us to clamp the sonoprobe, controlling and setting different distances between the sonoprobe tip and the capillary external wall. Experiments are initially run with a tip-capillary external-wall distance of $2\ \mathrm{mm}$ (Figure 5.3). This is an arbitrary distance which allows experiements to be performed at not too high cavitation activity (not too close to the sonoprobe tip) where the mechanical vibration of the tip and the very high cavitation activity would damage the capillary external surface. Each droplet experienced a residence time of less than $1\ \mathrm{s}$ below the sonoprobe and a total residence time of $15\ \mathrm{s}$ within the Perspex container.

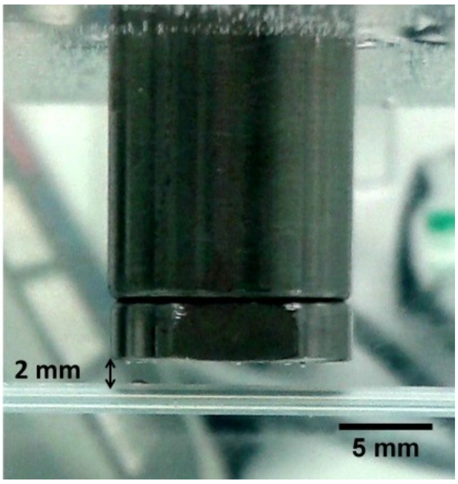

Figure 5.3. Horizontal alignment between the sonoprobe tip and the capillary.

5.2.2 COMSOL simulation of temperature profile

The actual temperature profiles within the capillaries are determined by using COMSOL Multiphysics 5.0. Figure 5.4a and Figure 5.4b show the temperature profiles at steady state along the capillary axis at the different cooling temperatures employed in our experiments.

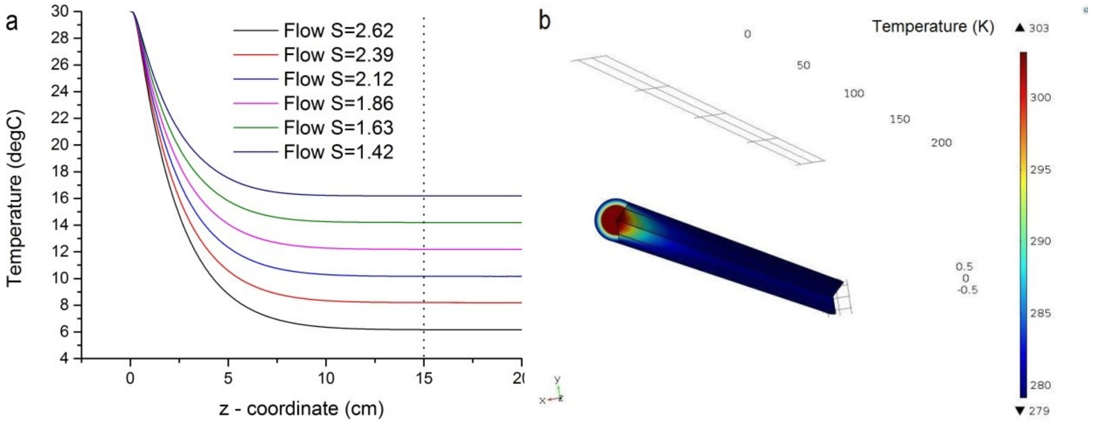

Figure 5.4. Temperature profiles along the capillary axis in flow conditions at different cooling temperature: from 30 °C to 6 °C (S=2.62), 8 °C (S=2.39), 10 °C (S=2.12), 12 °C (S=1.86), 14 °C (S=1.63) and 16 °C (S=1.42) (a). Temperature map along the capillary (3D section) in flow conditions for the cooling temperature: from 30 °C to 6 °C (S=2.62) (b).

As can be observed from the profiles, a plateau in temperature is achieved after about $15\ \mathrm{cm}$ from the inlet of the precooling section. That is why we decided to place the sonoprobe at the distance $L_1 + (L_2/2) = 20\ \mathrm{cm}$ from the section inlet. The effective achievement of the desired temperature T_2 is checked using a thin thermocouple placed within the capillary by means of a PEEK T-junction ($1\ \mathrm{mm}$ ID).

5.2.3 Crystal Detection and Filtration Protocol

Crystallization is detected by placing the high-speed camera attached to the optical microscope immediately after the sonoprobe (Figure 5.1). To improve crystal detection and eliminate light reflection problems owing to the curvature of the lateral walls of the capillary, we use a refractive index matching device in the microscope unit. The capillary is immersed in a plastic box (Figure 5.5) filled with water at room temperature ($22\ ℃$) and fixed by guides that allowed for the movement of the capillary in front of the microscope lens. Because of the small dimensions of the box, the crystals experience a very short residence time (around $1\ \mathrm{s}$); hence, no significant crystal growth can occur. Accordingly, we can safely assume that the CSD is not affected in the refractive index matching device.

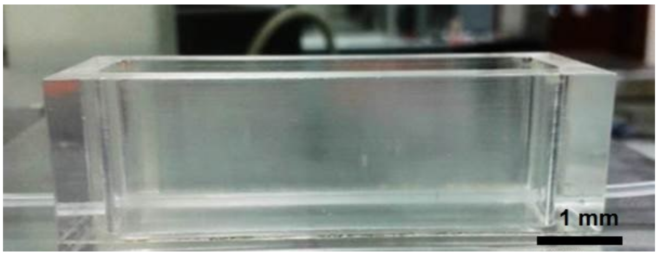

Figure 5.5. Refractive index matching device.

Crystals could be simply recovered by collecting all droplets on a filter paper. Unfortunately, we noted that hexane, which is very volatile, tends to evaporate immediately within the filter funnel when vacuum is applied flooding the filter and making the filtration impossible to occur. In light of this, the following filtration protocol is developed to recover crystals and determine their CSD.

Hexane and water droplets with crystals are collected in a $50\ \mathrm{mL}$ saturated solution kept at $T_3 = 22\ ℃$ (Figure 5.2). The collection time is set so that the solute concentration in the resulting solution C_T remains virtually unchanged (a $5\ \%$ maximum decrease is arbitrary accepted to reamain). This condition ensures that no significant crystal size reduction due to dissolution occurs in the collected mother liquor (nucleation and growth can not take place because the solution is not supersaturated), so that during the collection time the crystal size distribution is not altered. The collection time is set to $10\ \mathrm{min}$. Even in the situation in which ultrasound consumes the total available solute at the lowest temperature T_2 considered (making the solute reach its lowest concentration in the stream leaving the sonication section), a collection time of $10\ \mathrm{min}$ is found to meet the requirement given above. This is verified by solving the following adipic acid mass balance based on the mother liquor.

$$V_1C_1 + V_2C_2 = (V_1 + V_2)C_T \qquad \text{Eq. 5.1}$$

As we are dealing with dilute adipic acid solutions, the density of the solutions is assumed to be constant and equal to pure water. The density terms canceled out in Eq. 5.1. In V_1 and C_1 are respectively the volume and the concentration of the saturated solution at T_3 and V_2 and C_2 are respectively the volume and the concentration of the of mother liquor of the total droplets collected assuming that all the available adipic acid within the droplet has crystallized. C_2 is therefore the adipic acid saturated solution at T_3. The temperature and the concentration profile are depicted in Figure 5.6.

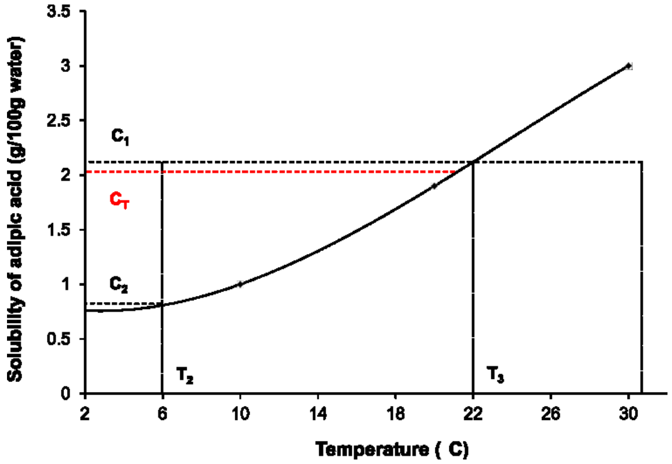

Figure 5.6. Temperature and the concentration profile during droplets collection.

Considering $V_1 = 50\ \mathrm{mL},\ C_1 = 2.12\ \mathrm{g/100\ mL},\ C_2 = 0.808\ \mathrm{g/100\ mL}$ which is the concentration of the saturated solution at $T_2 = 6\ °\mathrm{C}$ and $C_T = 0.95 \cdot C_1$, we calculate $V_2 = 4.3\ \mathrm{mL}$. For the flow rate is $Q = 0.3925\ \mathrm{mL/min}$, the maximum droplets collection time that allows us to operate below the concentration threshold C_T is:

$$t_{collection} < \frac{V_2}{Q} \cong 10 - 11\ \mathrm{min} \qquad \text{Eq. 5.2}$$

The solution containing the suspended crystals is first separated from the supernatant hexane (the two fluids are immiscible) and then filtered by means of vacuum filtration using $0.3\ \mu\mathrm{m}$ Whatman cellulose nitrate membranes. To recover all the crystalline material, the beaker and the filter funnel are washed with the prepared saturated solution of adipic acid at $22\ ^{\circ}\mathrm{C}$. The filters are dried for $10\ \mathrm{min}$ on a hot plate at $80\ ^{\circ}\mathrm{C}$ and weighed to determine the mass of the crystals produced. The crystals are subsequently suspended in vegetable oil, in which adipic acid is insoluble, and homogeneously dispersed using an ultrasonic water bath for $10\ \mathrm{min}$[117]. This slurry is used to determine the CSD with the laser diffraction particle size analyzer.

To establish whether or not primary particles break up in the ultrasonic water bath, we compared the CSD of the raw adipic acid material (raw particles purchased, which do not present agglomerates) with that of the same crystals suspended and treated in the ultrasonic water bath for $10\mathrm{min}$ according to our protocol. Finding the two CSDs nearly identical, we concluded that in the deagglomeration stage the primary particles do not break up. This stage affects only the agglomerates.

5.2.4 Sonochemiluminescence

Sonochemiluminescence (SCL) refers to the light that is emitted when luminol (5-amino-2,3-dihydro-1,4-phthalazinedione) reacts with OH· radicals owing to the presence of collapsing (that is, cavitation) bubbles. The nearly adiabatic collapse of the bubbles results in the rapid generation of high temperatures and pressures as well as highly reactive OH· radicals. Luminol reacts with these radicals to produce a characteristic bluish light which is employed to map the spatial distribution of active cavitation bubbles[130]. This technique, which was traditionally used in large geometries, has been recently adopted to demonstrate the cavitation activity in small geometries and microreactors[131,132].

In this work, SCL experiments are carried out using a deionized water solution containing $2\ \mathrm{mM}$ luminol (Merck) at $pH = 12$[129]. Luminol solution is flowed within the capillary sonocrystallizer to display the cavitation activity inside the capillary channel. To visualize the cavitation activity in the vicinity of the sonoprobe tip, the same luminol solution is also employed to fill up the Perspex enclosure. Images are captured in a dark room using a Nikon D60 camera with an $18 - 55\ \mathrm{mm}$ lens at a $35\ \mathrm{mm}$ focal distance. The exposure time is $3\ \mathrm{min}$, the focal ratio is 5.0 and the ISO setting is Hi1[133].

5.2.5 Numerical simulation of ultrasound wave propagation

To elucidate the correspondence between transient cavitation and enhancement of crystallization in the current sonocrystallizer, we simulate the wave propagation in the liquid inside the temperature-controlled Perspex enclosure containing the capillary (see section 5.3.5). The idea is to shed light on how acoustic waves, and the consequences of their propagation in water such as transient cavitation, can possibly influence nucleation of crystals. To this end, a linearized model, which is accepted to give reasonable results for pressure amplitudes and which accounts for wave attenuation owing to presence of bubbles, is solved using the finite element method. The model has been developed using COMSOL and validated by another team of researchers. The description of the acoustics and bubble dynamics implemented in the numerical model are not a subject of the current thesis and can be found in the following publication:

Rossi, D. et al. Continuous-Flow sonocrystallization in droplet-based microfluidics. Cryst. Growth Des. 15, 5519–5529 (2015).

To provide a correct boundary condition for the model we need to estimate the pressure amplitude at the tip of the sonoprobe P_a. The plane wave formulation relates the pressure amplitude at the source boundary to the ultrasonic power P_{US} transferred to the liquid; in its simplest form, it reads[134]:

$$P_a = \sqrt{\frac{2\rho_L v_{sound} P_{US}}{A_{tip}}} \qquad \text{Eq. 5.3}$$

in which $\rho_L = 1000\ \mathrm{kg/m^3}$ is the water density, $v_{sound} = 1480\ \mathrm{m/s}$ is the speed of sound in water at room temperature and A_{tip} is the area of the $13\ \mathrm{mm}$ diameter sonoprobe tip. To calculate the amplitude from Eq. 5.3, one should measure the power transferred to the liquid, and therefore, we use calorimetric measurements. A volume of $20\ \mathrm{mL}$ of deionized water is selected as the sample and fully insulated from the environment using thick layers of wool and aluminium foil. Thus, the dissipated power due to ultrasound could be evaluated by measuring the change in the temperature of the medium and accordingly the dissipated heat as

$$P_{US} = mc_p \frac{dT}{dt} \qquad \text{Eq. 5.4}$$

in which m is the mass of the water $(20\ \mathrm{g})$ and c_p is its specific heat capacity $(4186\ \mathrm{J/kg\ K})$.

The variation of temperature over time in the small beaker is shown in Figure 5.7. According to this temperature gradient, the power dissipated in the medium is calculated as $P_{US} = 8.3\ \mathrm{W}$. This value is used to estimate the pressure amplitude at the tip of the sonoprobe (Eq. 5.3), which results in a value of $P_a = 4.3 \cdot 10^5 \mathrm{Pa}$.

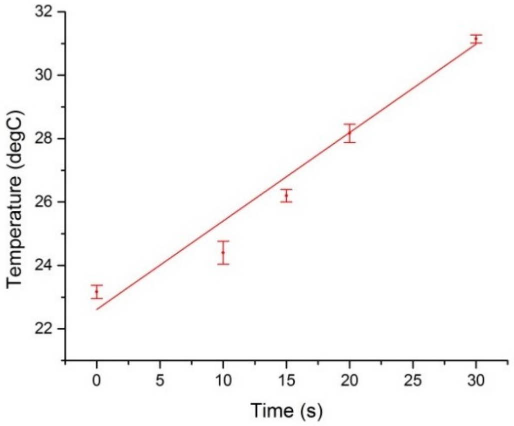

Figure 5.7. Temperature rise in the medium due to the dissipated power.

5.3 Results and discussion

5.3.1 Crystal size distribution and crystal production

To check the reproducibility of the experiments performed with the designed sonocrystallizer, each experiment is repeated three times and the CSD is measured. As a slight scattering in the CSD results is observed for each of the six supersaturations investigated, for each case we report the average result based on the three experimental values found. The corresponding representative standard deviations are shown as error bars reported at the peak of each curve (Figure 5.8). The data variability is attributed to the experimental error as well as to the crystal separation process, which involves a series of additional operations that can not be perfectly controlled and monitored. Because the CSD curves are not obtained by a nonintrusive online crystal detection method, data variability induced by the complex filtration protocol has to be considered as part of the overall experimental error. The results shown indicate that the supersaturation level does not have a significant effect on the CSD, and in turn on the resulting mean crystal size. The curves in Figure 5.8 have similar shapes, and, as one can see, overlap within the experimental error bars. A practically constant mean size $D_{4,3}$ value is measured and found to be around $15\ \mu\mathrm{m}$ for all the supersaturations investigated. The $D_{4,3}$ mean size provided by the laser diffraction measurements is defined as the ratio between the fourth and third moments (m_4 and m_3) of the crystal size distribution $n(L)$; consequently, it is

$$D_{4,3} = \frac{m_4}{m_3} = \frac{\int_0^\infty L^4 n(L) dL}{\int_0^\infty L^3 n(L) dL} \qquad \text{Eq. 5.5}$$

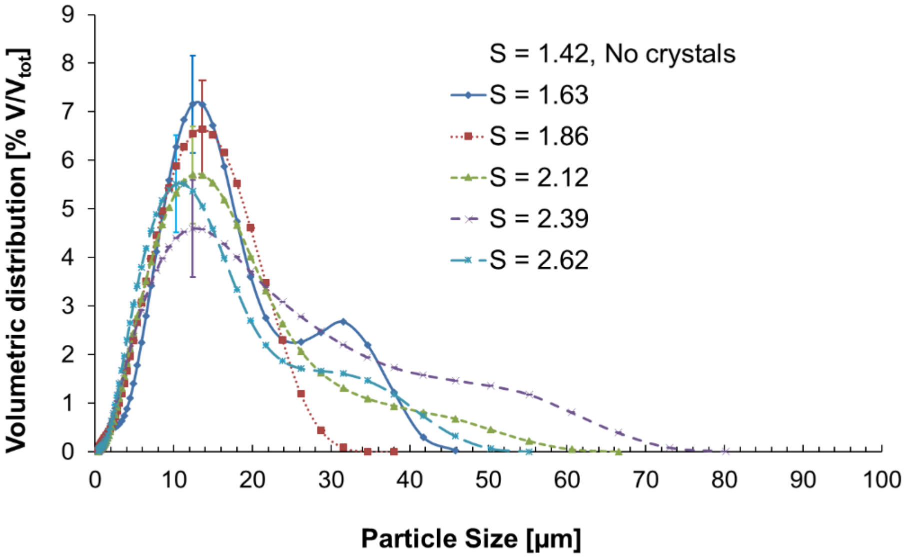

Figure 5.8. Effect of supersaturation on CSD. Supersaturations investigated: S=2.62, S=2.39, S=2.12, S=1.86, S=1.63 and S=1.42. Hexane and adipic acid solution flow rates = 0.3925 mL/min. Sonoprobe tip-capillary external wall distance = 2 mm. Ultrasonic system: Cole-Parmer Instruments 750 W ultrasonic processor, frequency = 20 kHz and amplitude = 21 %.

Even if the optical properties of the vegetable oil used does not allow us to clearly distinguish the crystal morphologies, by checking several snapshots (two are shown in Figure 5.9) we believe that the higher mode in the CSDs reported in Figure 5.8 is predominantly due to large primary particles. These particles form within the capillary sonocrystallizer under the conditions described in the experimental section, giving the CSDs reported in Figure 5.9.

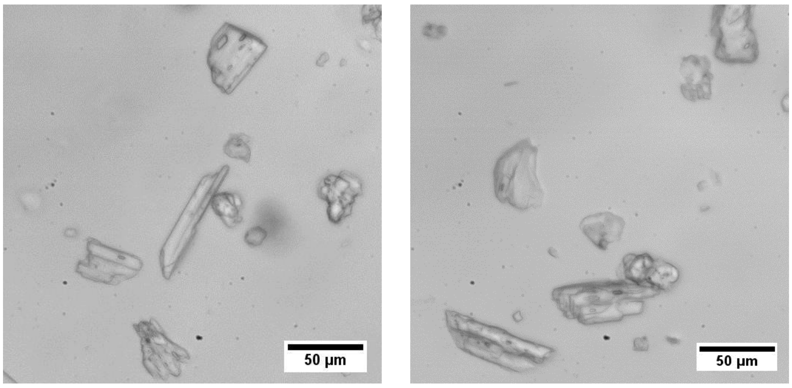

Figure 5.9. Two different pictures of adipic acid crystals after the deagglomeration step in vegetable oil.

Narducci et al.[33,61] designed an MSMPR continuous sonocrystallization process able to produce adipic acid crystals with the same sonication system employed in this study. However, because of the large volume of the system, this could not work with small residence times, and consequently crystal growth played a significant role during the crystallization process. As a result, a larger mean crystal size ($> 30\mu\text{m}$) was observed as compared with our case. On the other hand, the microscale geometry employed here allows experiments to be performed with very small residence times of $0.78\ s$. Crystal nucleation significantly occurs during such short times when ultrasound is applied. Crystals are collected immediately after the sonication stage; no growth section is present in the setup. This shows how quick the sononucleation process is. As soon as the desired supersaturation is reached, we immediately get crystals when the sonoprobe is switched on, whereas no crystals are visible when the sonoprobe is switched off (Figure 5.10).

Ultrasound OFF. No crystals detected.

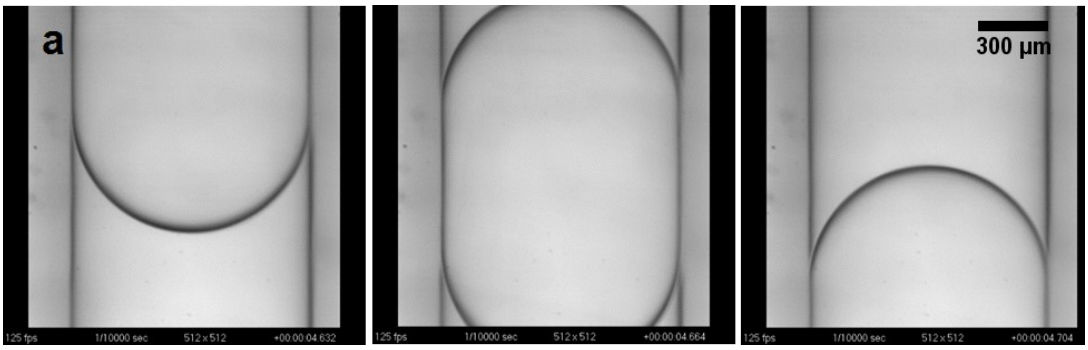

Ultrasound ON. Immediate crystal detection.

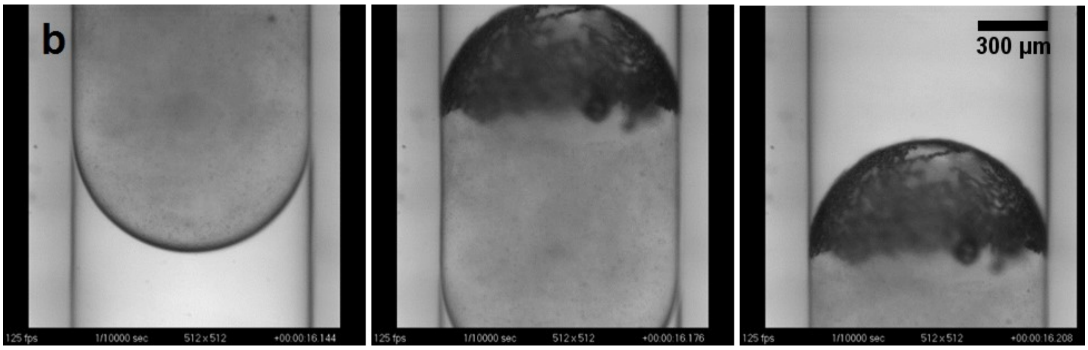

Figure 5.10. Adipic acid aqueous droplets in hexane carrier fluid showing accumulation of crystals. S=1.86. (a) Without sonication; (b) with sonication.

Crystals are created at all the supersaturations investigated except for $S = 1.42$ (Figure 5.11b). This value represents an approximate threshold below which the application of ultrasound does not have any effect, and therefore crystals do not form, as in silent conditions (Figure 5.11h). In conclusion, the capillary sonocrystallizer represents a promising solution for obtaining very small crystals with a reproducible mean size in a very short time. The apparatus leads to crystals one order of magnitude smaller than the commercial adipic acid raw material from suppliers, micronized materials, and hammer milled materials[61].

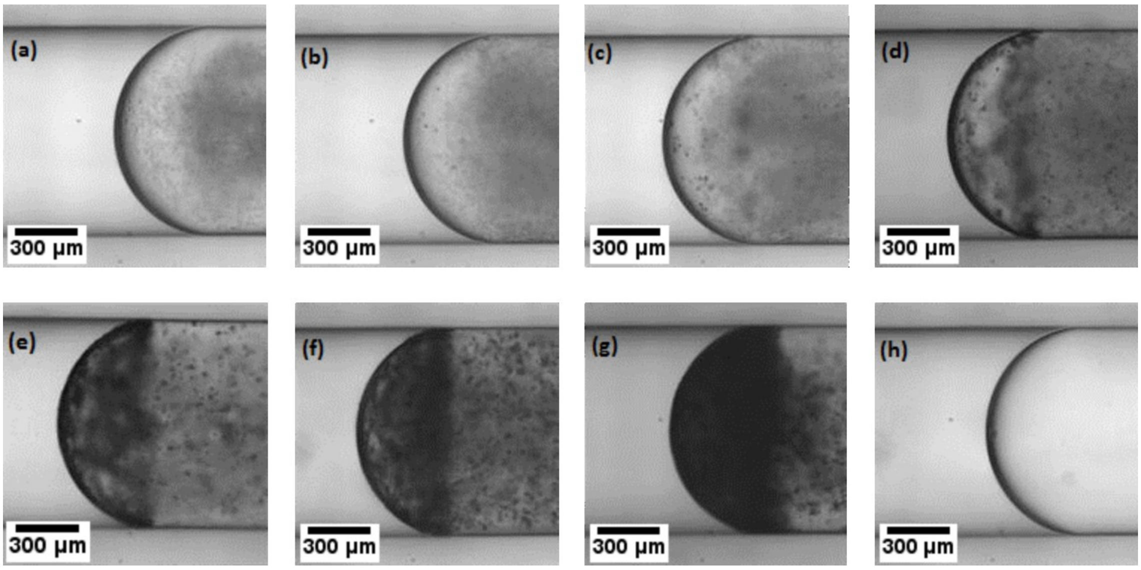

Figure 5.11. Rear end of aqueous droplets in hexane carrier fluid showing accumulation of crystals at various supersaturation conditions. (a) Without adipic acid, with sonication; (b–g) with adipic acid, with sonication; (h) with adipic acid, without sonication. The flow is from left to right. (b) S=1.42, (c) S=1.63, (d) S=1.86, (e) S=2.12, (f) S=2.39, (g) S=2.62, (h) S=2.62.

Assuming no crystal loss during washing, and neglecting the amount of retained mother liquor and impurities, the crystal yield Y is calculated as

$$Y(\%) = \frac{\Delta m_{filt}}{\Delta m_{eq}(T_2)} \cdot 100 \qquad \text{Eq. 5.6}$$

Y represents the percentage of the mass of adipic acid crystallized and therefore filtered Δm_{filt} over of the maximum mass that theoretically can be crystallized at temperature T_2 ($\Delta m_{eq}(T_2)$). The crystal yield Y is determined over the $10\ \mathrm{min}$ collection time (see Eq. 5.2), and the corresponding values are plotted at the different supersaturation levels in Figure 5.12.

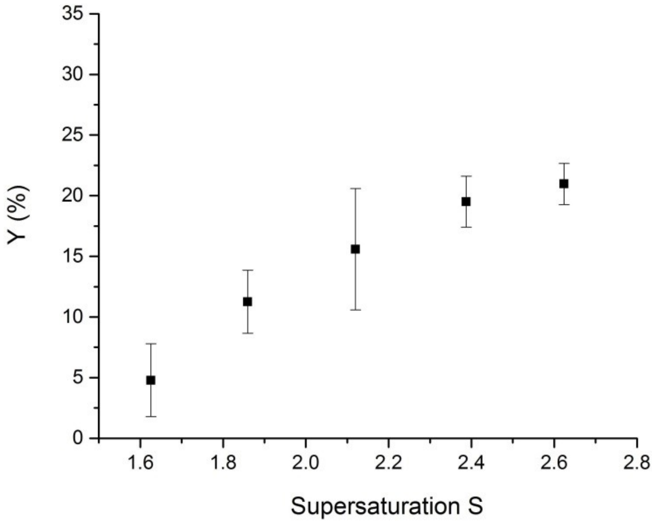

Figure 5.12. Crystal yield at different supersaturations. Hexane and adipic acid solution flow rates = 0.3925 mL/min. Sonoprobe tip-capillary external wall distance = 2 mm. Ultrasonic system: Cole-Parmer Instruments 750 W ultrasonic processor, frequency = 20 kHz and amplitude = 21 %.

The data show an increase of Y with initial supersaturation. This is explained by the increase of the driving force available for crystallization. Note that only a low percentage (maximum around $20\ \%$ at the highest supersaturation) of all the available dissolved adipic acid is crystallized. This is probably due to the lack of a growth stage after the sonication stage. In fact, the higher values of yield measured by Narducci et al.[33] for continuous cooling sonocrystallization of adipic acid were obtained with much longer residence times (a few hours) than those used in this work.

5.3.2 Crystal morphology

Figure 5.13 shows pictures of dried (Figure 5.13a) and resuspended (Figure 5.13b) adipic acid crystals. In the first figure, agglomerates are observed. Most of these are disrupted in the ultrasound-induced deagglomeration step, which yields smaller groups of crystals (Figure 5.13d). The mean crystal size visible by microscope (ca. $10\ \mu\mathrm{m}$) is qualitatively in accordance with the mean size $D_{4,3}$ determined by laser diffraction.

In silent conditions, adipic acid normally crystallizes from aqueous solutions as flat, slightly elongated, hexagonal, monoclinic plates[116] (Figure 5.13c). These crystals have a size of around $50 - 200\ \mu\mathrm{m}$, depending on the growth time.

This characteristic crystalline structure changes when ultrasound is implemented: crystals become smaller, more irregular, rounded, and the typical hexagonal-like habit is lost (Figure 5.13d). The presence of small fragments and the typical irregular geometries observed suggests the occurrence of mechanical disruption induced by cavitation[6,8].

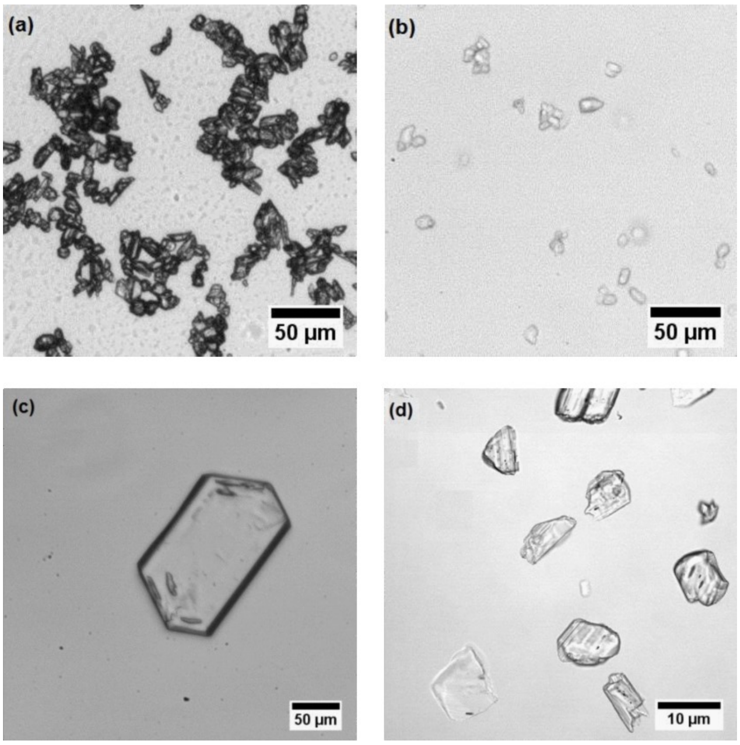

Figure 5.13. Adipic acid crystals: (a) dried on hot plate, (b) resuspended in vegetable oil, (c) without ultrasound, (d) with ultrasound.

5.3.3 Hydrodynamic effects

Ultrasound is the crucial factor that triggers nucleation at all the supersaturations investigated (Figure 5.11). The same experiments performed in silent conditions do not show any crystal formation: the droplets appear transparent, and consequently the nucleation rates are practically zero. In Figure 5.11 the difference between silent and sonicated conditions at all the supersaturation levels is shown. A sharp and marked effect is observed when ultrasound is switched on in terms of immediate crystal production and crystal accumulation at the rear end of the aqueous droplet (Figure 5.14). This accumulation is most probably induced by the internal droplet mixing which pushes backwards the crystals generated by ultrasound[119]. The amount of crystals produced increases with supersaturation in accordance with the yield trend of Figure 5.12.

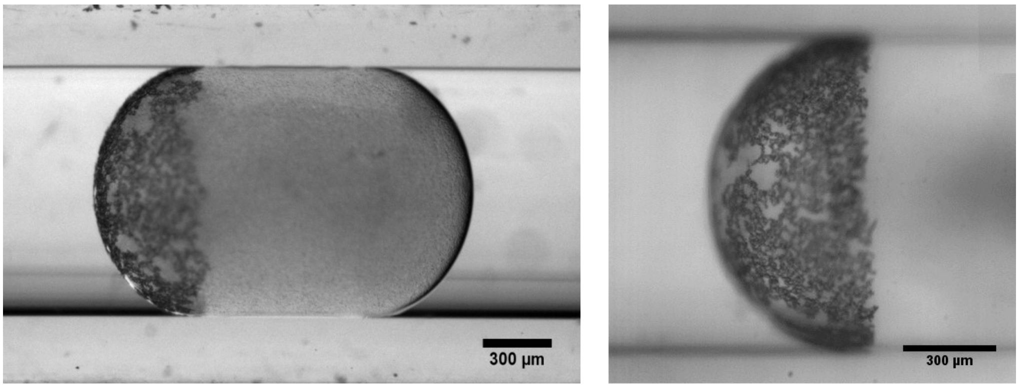

Figure 5.14. Crystal accumulation at the rear end of the aqueous droplet.

The sonocrystallization event is accompanied by water/hexane emulsification: droplets appeared milky as compared with the clean and transparent droplets without crystals obtained under silent conditions (Figure 5.11h). Sonoemulsification (SE) and sonocrystallization (SC) are both promoted by sonication. The former occurs at all the supersaturations investigated, as it is not affected by the presence of the crystallizing compound. The latter, on the other hand, is linked to a specific level of supersaturation, as only when a certain supersaturation is reached the crystals are immediately detected. In this regard, the minimum supersaturation ratio at which sonocrystallization is experimentally observed is $S^{*} = 1.63$ (Figure 5.11c). For $S < S^{*}$ crystals are not detected and only sonoemulsification occurred. For $S < S^{*}$, an increase of the ultrasonic power, obtained by reducing the sonoprobe tip-capillary distance, does not trigger nucleation: only emulsification is intensified (Figure 5.15).

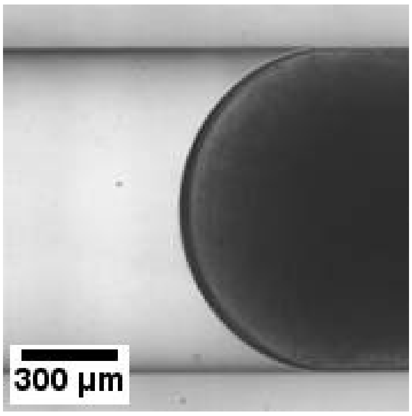

Figure 5.15. Rear droplet emulsion, S=1.42, tip-capillary distance = 0.7 mm.

To determine if crystals are present within the droplets, we always resort to visual observation and filtration. No data point is reported for $S < 1.63$, because we can not collect and weigh any crystal on the filter paper. This confirms the absence of crystals observed in Figure 5.11h within the droplets.

5.3.4 Sonochemiluminescence and its relation to SE and SC

Above the critical supersaturation level S^*, nucleation is linked to transient cavitation occurring inside the capillary channel, and therefore within the droplet volumes where sonocrystallization takes place. This can be shown by monitoring the direct relation between SCL and SE effects in parallel with the concurring crystal production. For $S > S^*$, as long as the sonoprobe is close to the capillary, we see a direct correspondence between the amount of crystal accumulated at the rear end of the droplet, the intensity of the light emitted by the SCL effect, and the amount of generated emulsion. In Figure 5.16, the relation among the three phenomena for a supersaturation of $S = 1.86$ is examined. Similar trends are observed for all the supersaturations investigated. In all cases, above a sonoprobe tip-capillary distance of $10\ \mathrm{mm}$, SCL, SE, and SC are not detectable. In conclusion, as transient cavitation is required for both SCL and SE[128], the results indicate that transient cavitation is crucial for sonocrystallization.

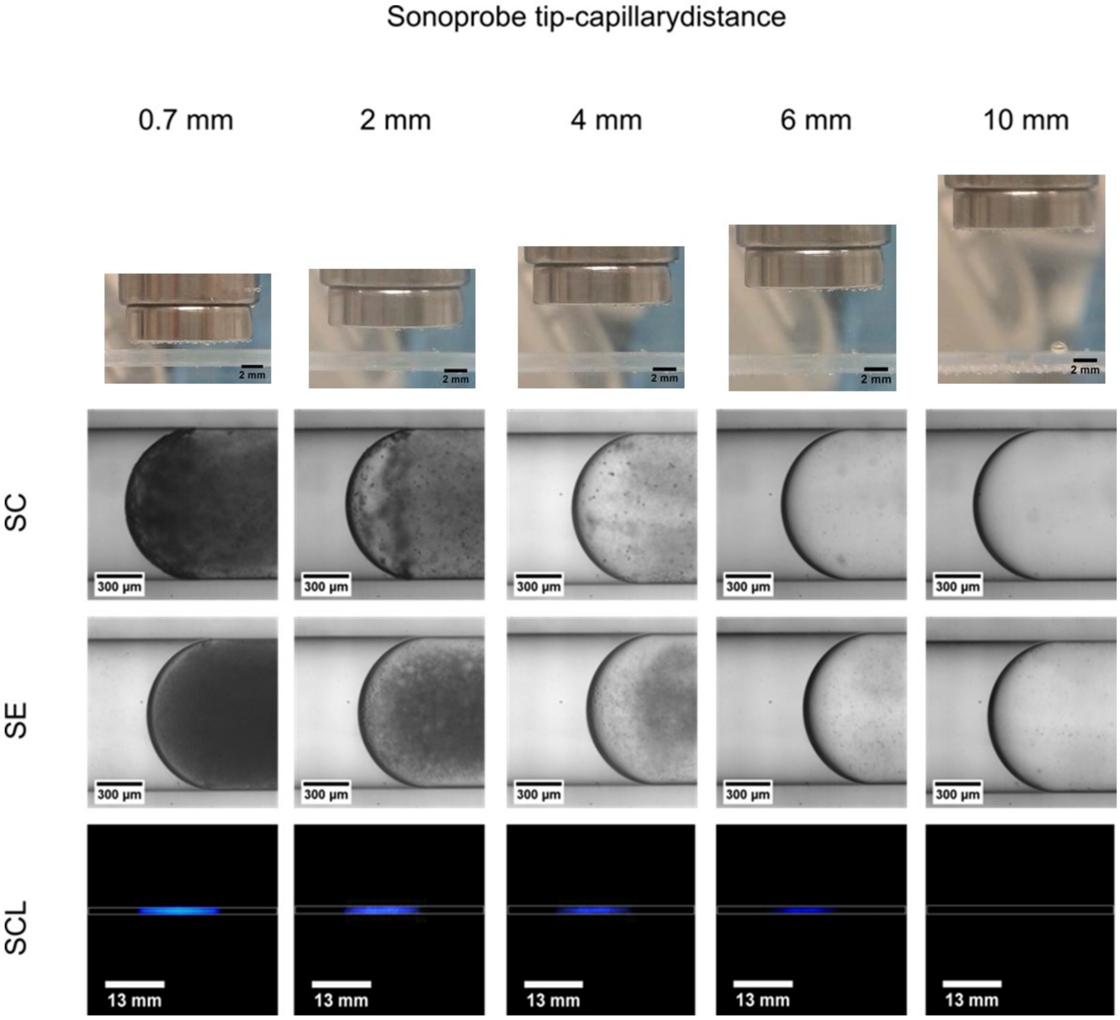

Figure 5.16. Sonocrystallization (SC), sonoemulsification (SE), and sonochemiluminescence (SCL) at different sonoprobe tip-capillary distances for S=1.86. Luminol solution is flowing within the capillary.

Figure 5.17 provides qualitative indication of transient cavitation occurring below the sonoprobe tip surface. If the capillary is removed and the luminol solution is placed directly within the Perspex enclosure, a cone-shaped bright area is observed. The sonochemiluminescence detected is the consequence of the cavitation bubbles self-arranged in the typical cone-like macrostructure in the vicinity of the sonoprobe tip flat surface[135]. A consistent attenuation of the light intensity and consequently of transient cavitation is registered after approximately $10\ \mathrm{mm}$. This is in accordance with Figure 5.16. After a distance of $10\ \mathrm{mm}$, the acoustic pressure decreases to a level at which cavitation is less likely to occur, and therefore SCL, SC, and SE are drastically reduced (for more details, see section 5.3.5). In this regard, we should note that the plastic capillary is acoustically transparent, so that the acoustic field is not affected by its presence.

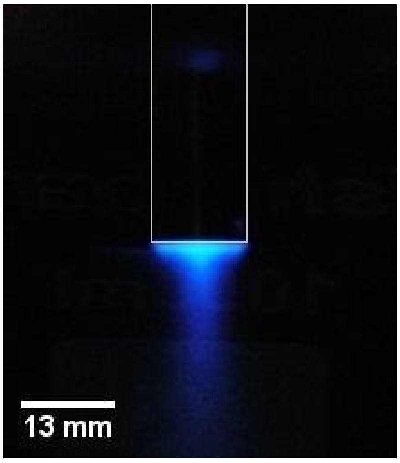

Figure 5.17. Sonochemiluminescence below the sonoprobe tip. A luminol solution is placed within the Perspex enclosure without the capillary.

5.3.5 Cavitation analysis using the results of the numerical simulation

Numerical results for distribution of the pressure amplitude on a cross section passing through the middle of the sonoprobe are shown in Figure 5.18. The pressure drops away from the tip due to the absorbing behaviour of the side walls as well as damping effect of the bubbles. It is concluded that, if the consequences of higher acoustic pressure, such as transient cavitation, are desirable, the distance between the sonoprobe and the capillary carrying the solution should be kept to a minimum.

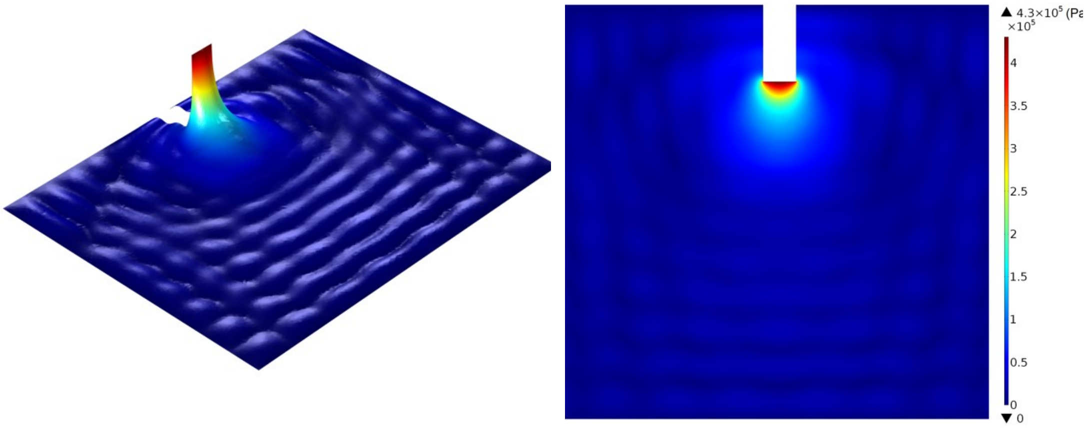

Figure 5.18. Acoustic pressure distribution on a cutting plane passing through the middle cross section of the sonoprobe.

To quantify this conclusion, the radial dynamics of bubbles are modelled at different pressure amplitudes descending from $4.3 \cdot 10^5\ \mathrm{Pa}$, which is the amplitude at the surface of the sonoprobe. The results are shown in Figure 5.19. This trend can be seen in the figure for pressure amplitudes $\geq 1.9 \cdot 10^5\ \mathrm{Pa}$. For amplitudes below this value the bubbles tend to oscillate nonlinearly.

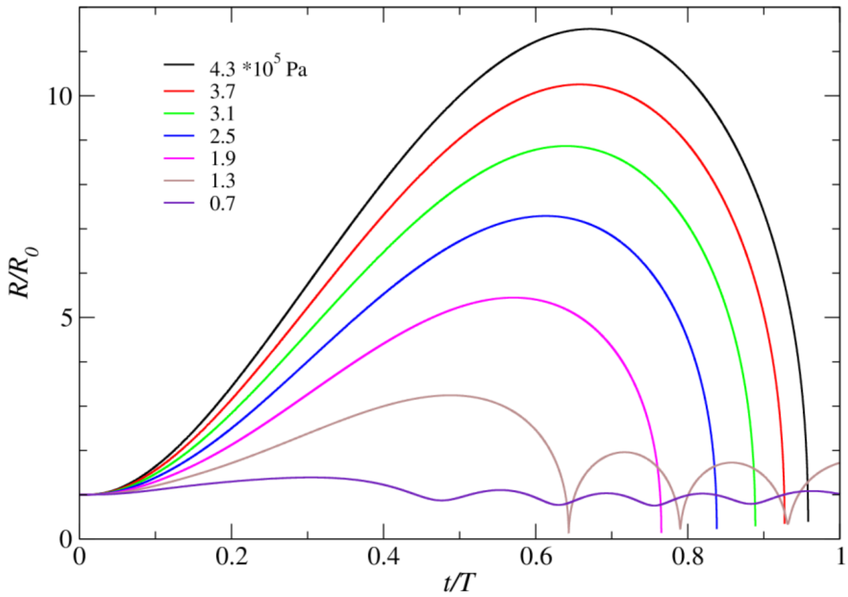

Figure 5.19. Bubble radial dynamics over one acoustic cycle for a bubble assuming an initial bubble size of 30 µm at different pressure amplitudes.

Although it is difficult to define a sharp threshold, the value of $1.9 \cdot 10^5\ \mathrm{Pa}$ can be used as an approximate threshold for transient cavitation in this case. Hence, the zone near the sonoprobe where we expect the bubbles to experience transient cavitation could be predicted from the simulation. This is illustrated in Figure 5.20 in which the decreasing pressure amplitude is plotted versus the distance along the axis of the horn. For comparison, the transient cavitation threshold is shown in the graph as the horizontal dashed line. According to the figure, pressure drops in approximately $10\ \mathrm{mm}$ from the tip to values below the threshold. This is in agreement with the experimental results in which no crystals and no SCL are observed after increasing the distance between the capillary and the sonoprobe beyond $10\ \mathrm{mm}$. For more reliable predictions of cavitation activity and correlating it to nucleation of crystals, we propose to measure the initial distribution of bubbles and their void fraction in a more precise way, because they do affect the pressure distribution, as it is depicted in this work.

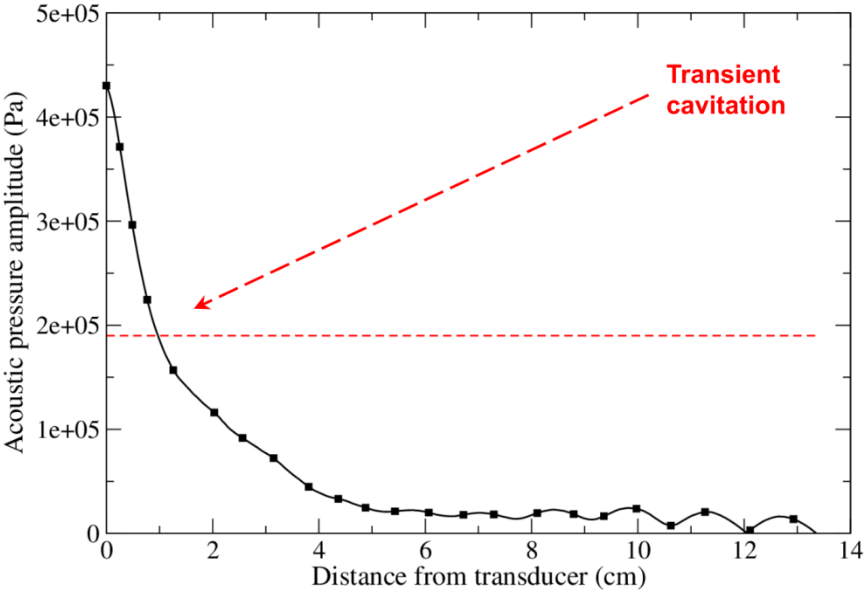

Figure 5.20. Pressure amplitude along the axis of the sonoprobe to the bottom of the reactor. The horizontal dashed line shows the transient cavitation threshold.

5.3.6 Stochastic model feasibility with US

The experimental setup showed in Figure 5.1 is suitable to run a similar stochastic analysis to the one performed in chapter 4 with the difference that in this case we attempt to calculate the nucleation rate of adipic acid in flow conditions under the effect of ultrasound. For this reason, the setup of Figure 5.1 is slightly different from the silent setup of Figure 4.3. In the former in fact the growth stage is missing as the crystals are immediately produced after the short sonication period. Therefore there is no need to add a separate growth unit to let the crystal reach an observable size. Crystals are detected by means of the Photron high speed camera FASTCAM MC1 which is placed straight after the sonoprobe and before the collection stage at T_3. Moreover, the new setup is modified to fit and align the sonoprobe as well as to keep the capillary straight within the Perspex enclosure at T_3. The droplet generation occurs identically in both cases at T_1. The supersaturation S is changed within the region above the rapid crystal production threshold $S^* = 1.63$. Hence, $S^* = 1.63$, $S = 1.86$, $S = 2.12$, $S = 2.39$ and $S = 2.62$ are the selected supersaturations. A tip-capillary external-wall distance of $2\ \mathrm{mm}$ is fixed. To decrease the time during which the droplets are exposed to the ultrasound field, water and hexane flow rates are equally increased. With this technique, we aim to calculate the nucleation rate refining the time axis down to fraction of seconds. Hopefully this condition will allow us to observe a non-step crystal production and therefore apply the stochastic method introduced before. The length of the capillary L_1 submerged in the precooling chamber of the Perspex container is changed in order to achieve the desired temperature T_2. The capillary is coiled and fixed between the lateral walls of the precooling chamber and kept horizontal in the sonicated section. The temperature T_2 is checked by COMSOL simulations and by using a thin thermocouple placed within the capillary. The total hexane and adipic acid solution flow rates, the corresponding average fluid velocities, precooling capillary lengths L_1 and sonicated residence times are reported in Table 5.1.

Table 5.1. Fluid dynamics specifications for the continuous flow droplet-based sonocrystallizer with US.

Cross section (mm^2)	Tot. flow rate (mL/min)	Average velocity (m/min)	Precooling length L_1 (m)	Cooling res. time (s)	Sonicated length (m)	Sonicated res. time (s)
0.785	0.785	1	0.15	9	0.013	0.78
	1	1.27	0.2			0.61
	1.4	1.78	0.28			0.44
	3	3.82	0.6			0.20
	4	5.10	0.8			0.15
	7.85	10	1.5			0.078

As compared to the old setup in which a total flow rate of $0.785\ \mathrm{mL/min}$ and sonicated residence time of $0.78\ \mathrm{s}$ were employed, here the sonicated residence time is decreased to a minimum of one order of magnitude ($0.078\ \mathrm{s}$) using a flow rate ten times higher ($7.85\ \mathrm{mL/min}$). The droplets are generated using a T-junction with an inlet for both the continuous and disperse phases equal to $0.5\ \mathrm{mm}$. According to Eq. 2.70 when both phases are introduced with the same channel diameters the droplet size R scales as $R \propto Ca^{-0.3} \propto (\mathrm{Average\ velocity})^{-0.3} \propto (\mathrm{Tot.flow\ rate})^{-0.3}$. As a result, the volume of the droplets can not be assumed constant for all the flow rates considered. Furthermore, the application of ultrasound tends to emulsify the droplets altering the original droplet volumes. The actual droplet lengths and volumes are therefore measured experimentally with the help of the high speed camera (Table 5.2). An average volume $V_{av} = 1.05\ \mathrm{mm}^3$ is employed in the cumulative probability function $P_T(t, S, V)$ (Eq. 2.48) to determine the value of the nucleation rate $J(S)$ by fitting the experimental cumulative function $P_E(t, S, V)$ (Eq. 2.49).

Table 5.2. Droplet lengths and droplet volumes at different flow rates.

Tot. flow rate (mL/min)	Droplet Length (mm)	Droplet Volume (mm^3)
0.785	2.2	1.5
1	2.0	1.3
1.4	1.8	1.2
3	1.5	0.9
4	1.4	0.8
7.85	1.1	0.6
		V_{av} = 1.05

Figure 5.21 shows the experimental cumulative probability functions for the five supersaturations investigated. At all the supersaturations the values of $P_E(t, S, V)$ is practically constant with the time and equal to one. In other words, the discretization of the time scale below $1\ s$, does not allow us to evaluate the exponential monotonic trend previously observed in the silent experiments. The experimental cumulative data have a unique value and no particular differences are registered when the sonicated residence time decreases. Ultrasound reduces the stochasticity of the process that becomes deterministic. A step-like pattern is present and therefore the $P_E(t, S, V)$ fitting leads to very high values of nucleation rates that are $10^4 - 10^5$ higher than the corresponding silent experiments. The fittings of Figure 5.21 are performed on the mean values around the standard deviations. The difference between the several supersaturations are attributed to the experimental errors rather than to a physical reason. However, these values represent only a lower limit and are not accurate as a further discretization of the time scale would be necessary before applying the fitting and calculate $J(S)$. Unfortunately, this is impossible as the pumps can not deal with such high flow rates and pressure

drops. In addition, the monodisperse droplets pattern would be too difficult to achieve.

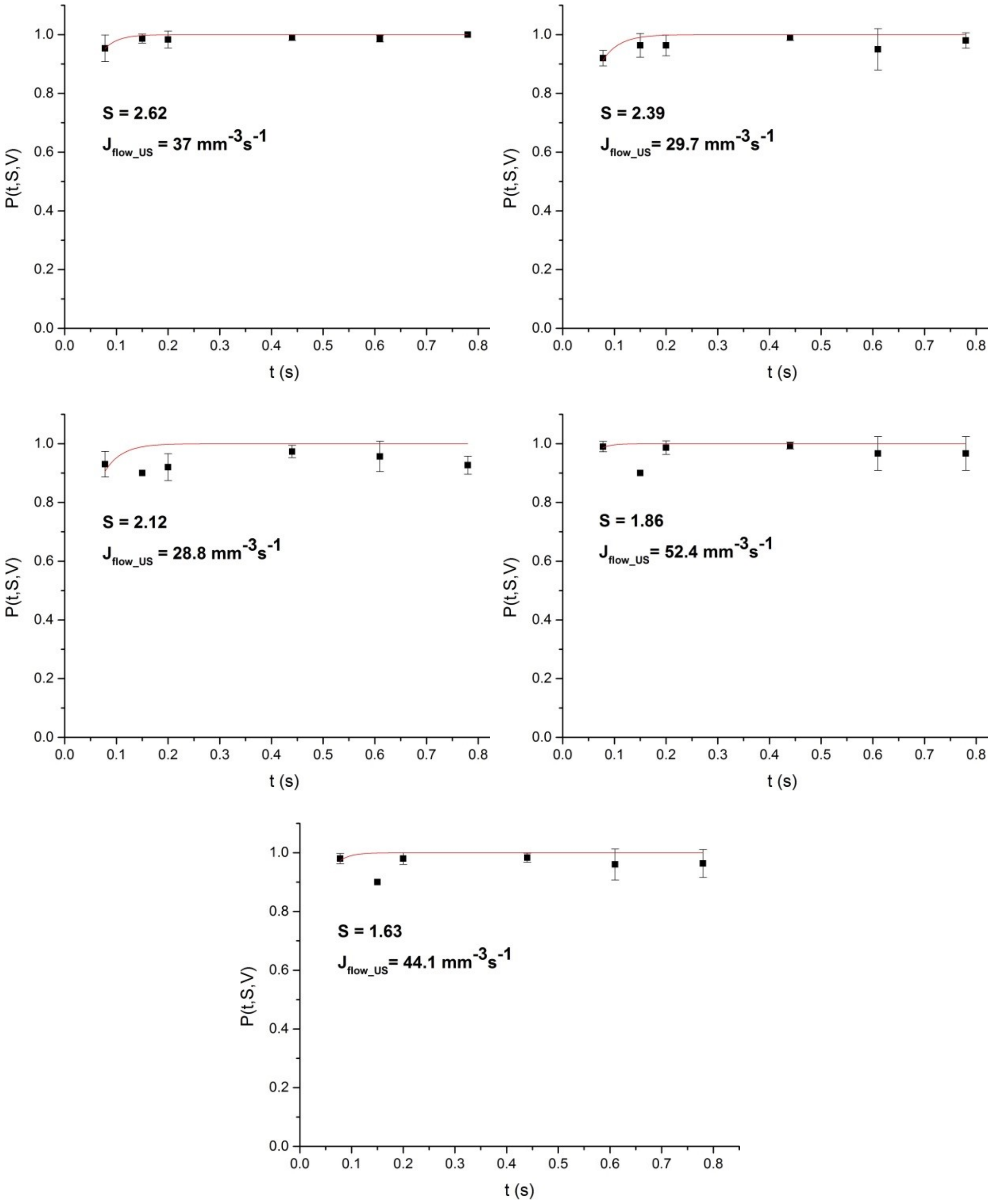

Figure 5.21. Adipic acid experimental probability function $P_E(t,S,V)$ for various supersaturations.

It is worth mentioning that nucleation rates determined in this section refer only to primary nucleation. The probability function is related only to the presence of at least one crystal: it is not concerned with the total number of crystals present in each droplet. Agglomeration, breakage and secondary nucleation that might occur during the application of ultrasound have only to do with crystal particles that are already present in the droplet volume. Therefore these processes do not affect the values of the experimental probability function and the derived primary nucleation rates.Conclusions

In this chapter, a droplet-based microfluidic device for production of adipic acid crystals using ultrasound is presented. The system is able to provide crystals with a very small mean size $(15\ \mu\text{m})$ at high production rates. The crystal size distributions and the corresponding mean size of crystals are independent of the supersaturation level. However, a minimum supersaturation level $S^* = 1.63$ is required to trigger the sonocrystallization process. The production rate (crystal yield) increases by increasing the supersaturation. A maximum yield of about $20\ \%$ is obtained at the highest supersaturation employed $S = 2.62$. Cavitation activity is investigated using sonochemiluminesence and sonoemulsification experiments. Results demonstrate that after a distance of about $10\ \text{mm}$ from the sonoprobe tip, all of the consequences of cavitation disappear. This observation is also investigated numerically by simulation of the wave propagation in the medium. The analysis shows that the expected zones for transient cavitation are predictable by numerical simulations. Furthermore, it is concluded that transient cavitation of bubbles and its consequences are a significant mechanism for enhancing nucleation of crystals among several proposed in the literature.

The designed microfluidic system is also adopted to run stochastic analysis of crystal primary nucleation and calculate the adipic acid primary nucleation rates under the presence of ultrasound. Results show a very rapid enhancement of nucleation processes. As soon as ultrasound is switched on an immediate crystal production is observed. Nucleation occurs in a fraction of a second or even less and therefore a step-like trend in the cumulative probability function leads to nucleation rates of at least four orders of magnitude higher than the corresponding silent ones. Sonication induces a step change from stochastic behaviour to determinist behaviour.

6. Continuous flow sonocrystallization in single-phase microfluidics

In this chapter, we present a second sonocrystallizer, which does not involve the use of a second phase, to produce small crystals with narrow CSDs in a reproducible way without clogging. To avoid channel occlusion, large capillary diameters are adopted.

6.1 Introduction

Most reviews on microfluidic reaction technology mention that micro-reactors are unsuited to the processing of solids having a size between 0.1 and 0.01 channel widths[31,65]. Although some microfluidic systems can be used to produce nanoparticles with excellent control of size, the management of solid compounds with a characteristic size in the range of the smallest channel dimension is still a major challenge to be addressed. Nowadays, microfluidic systems have been demonstrated to be incapable of processing crystals within channels having a similar size[32]. To circumvent this problem, the size of the precipitating particles must be minimized and their interactions with the walls reduced. One such approach involves using liquid-liquid two-phase flow (see section 2.3.2). This method was successfully employed in the previous chapter. Unfortunately, the use of liquid-liquid two phase flow to address channel fouling when dealing with particles in narrow channel geometries, complicates the entire continuous sonocrystallization process introducing operational challenges that are generally not desired. In fact, the use of a second fluid phase inevitably adds additional separation steps that have to be taken into account in the cost and purity of the final delivered crystalline product. Moreover, hexane and other organic solvents are toxic and flammable and hence incompatible with sterile pharmaceutical environments. To overcome these issues, one needs to remove the second fluid phase and increase the channel size to avoid channel fouling. In this chapter, a single-phase crystallizer based on the use of capillaries of large diameter (> $1\ \mathrm{mm}$) is designed for avoiding crystal blockage along the channel walls.

6.2 Experimental section

In this section, we describe the experimental setup and procedure employed to run continuous flow sonocrystallization experiments in single phase flow.

6.2.1 Experimental setup and procedure

Figure 6.1 shows the schematic of the single-phase capillary sonocrystallizer used in this work. One syringe with the undersaturated adipic acid solution is placed inside the Perspex enclosure at T_1. The nucleation section at T_2 is identical to the droplet-based setup of Figure 5.1. The sonoprobe ($750\ \mathrm{W}$ ultrasonic processor, frequency = $20\ \mathrm{kHz}$ and amplitude = $21\ \%$) is aligned with and placed $2\ \mathrm{mm}$ above the PFA capillary immediately after the desired supersaturation is reached in the precooling section. This condition is checked by COMSOL simulations (not reported this time) as well as measuring the temperature with a simple thin thermocouple probe inserted in the capillary from the outlet and moved upstream till reaching the precooling section.

The crystal collection stage at T_3 described in section 5.2.3 is no longer needed. Here the carrier fluid is not present in the system and therefore crystals can be directly filtered using $0.3\ \mu\mathrm{m}$ Whatman cellulose nitrate membranes. These membranes are dried for $10\ \mathrm{min}$ on a hot plate at $80\ °\mathrm{C}$ and weighed to determine the mass of the crystals collected. The crystals are subsequently suspended in vegetable oil, in which adipic acid is insoluble, and homogeneously dispersed using an ultrasonic water bath for $10\ \mathrm{min}$[117]. This slurry is used to determine the CSD with the laser diffraction particle size analyzer. Eq. 5.6 is employed to calculate the yield of the process. To check the reproducibility of the experiments performed, each experiment is repeated three times and the CSD is measured. For each case we report the average result based on the three experimental values found. The corresponding representative standard deviations are shown as error bars reported at the peak of each curve.

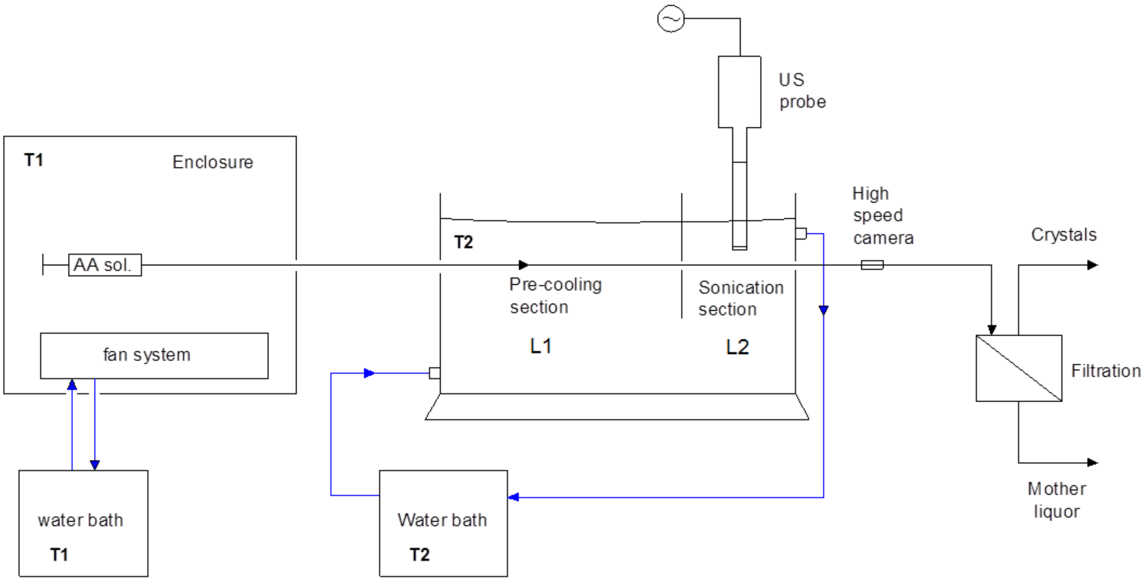

Figure 6.1. Schematic of the single phase capillary sonocrystallizer setup.

The performance of the system is also evaluated by measuring the concentration of the mother liquor solution using a conductivity calibration curve for adipic acid obtained at constant temperature. Hence, a number of experiments are carried out to work out the correlation between electrical conductivity and concentration of dissolved adipic acid at $30\,°\mathrm{C}$. A linear relationship between the two physical quantities is illustrated in Figure 6.2. The amount of adipic acid produced for a given experimental condition can be measured directly by weighing the amount of crystals collected on the filter paper or as a difference between the initial dissolved solute and concentration of adipic acid in the mother liquor at $30\,°\mathrm{C}$.

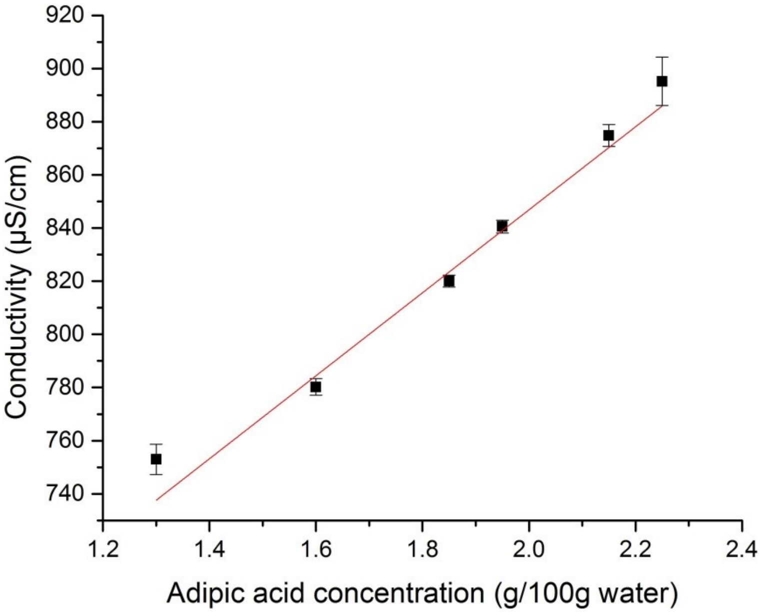

Figure 6.2. Adipic acid concentration in the mother liquor as function of electrical conductivity at 30 °C.

Two different sets of experiments are conducted. In the first set, we investigate the effect of sonicated residence time on CSDs and crystal production. To do this, we keep the sonicated volume constant and we increase the flow rate (refer to section 6.3.2 for details). In the second set, we investigate the effect of volume of the sonicated portion of the fluid on CSDs and crystal production. To do this, we employ larger capillary diameters while increasing the flow rates to keep the sonicated residence time constant (refer to section 6.3.3 for details).

6.3 Results and discussion

6.3.1 Investigation of channel clogging in single phase flow

Different experiments are conducted to find out whether it is possible to run a single-phase continuous sonocrystallization process without clogging at the desired supersaturations. Results show that channel blockage always occurs when using $1\ \mathrm{mm}$ ID PFA capillaries. Regardless of the supersaturation and flow rate adopted, the channel occludes within the capillary at the sonoprobe alignment point, where the immediate crystal production is triggered (Figure 6.3). The time at which the channel clogs is random, from a few seconds up to a minute and does not depend on the specific supersaturation.

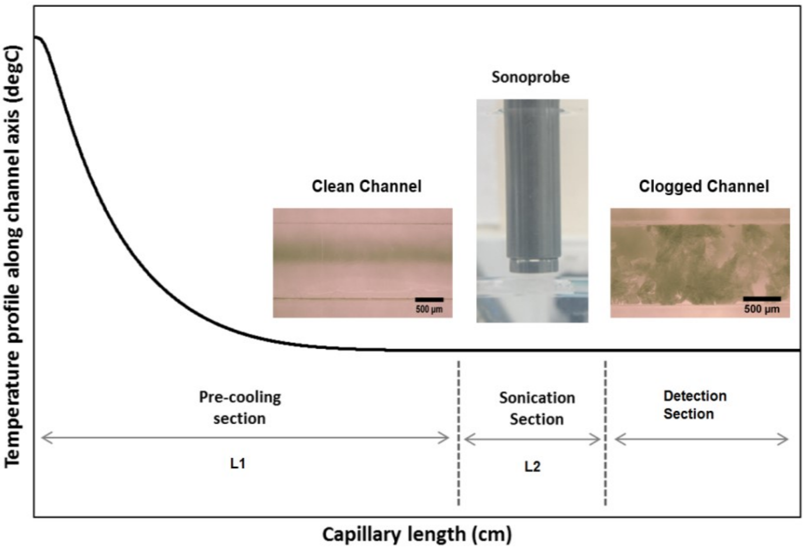

Figure 6.3. Crystal accumulation along the channel.

The dynamics of channel clogging cannot be predicted by using Eq. 2.64, Eq. 2.65 and Eq. 2.66 as they only apply to silent regime, when a channel restriction is present and when the particles have the same diameter and are perfectly spherical. As already observed for the droplet-based system, ultrasound does not promote nucleation below the threshold $S^* = 1.63$. As a result, channel occlusion does not occur below this value. The same experiments conducted in silent conditions do not show any crystal accumulation along the channel. The channel internal surface appears to be clean, as a very short residence time (less than one second) is set beneath the probe and therefore crystal nucleation is almost null or extremely low.

Quite unexpected results are obtained when the capillary internal diameter is larger than $1\ \mathrm{mm}$. For example, the use of capillary tubes with larger diameter ($1.55\ \mathrm{mm}$, $2.4\ \mathrm{mm}$, $3.2\ \mathrm{mm}$, and $4\ \mathrm{mm}$ ID) does not present any clogging issues when ultrasound is turned on. In all these cases, crystals are instantly produced in the sonicated section (the section of the channel beneath the probe) above the supersaturation threshold $S^* = 1.63$ and then collected on the filter paper (Figure 6.4). The same experiments conducted in silent conditions in large capillary tubes do not show any crystal accumulation along the channel. In fact, very short residence time is set beneath the probe and therefore only very few crystals are formed.

Ultrasonic baths operating in the kilohertz regime and piezoceramic actuator have been implemented with lab-on-a-chip geometries to manage the formation of solids in flow chemistry[65]. However, the reasons of such anti-clogging behaviour observed in our process when both US and large capillaries are employed would require a separate study. This would involve complex phenomena interaction between heterogeneous crystal nucleation on the channel walls, crystal growth, crystal breakage and crystal agglomeration on a very small time scale.

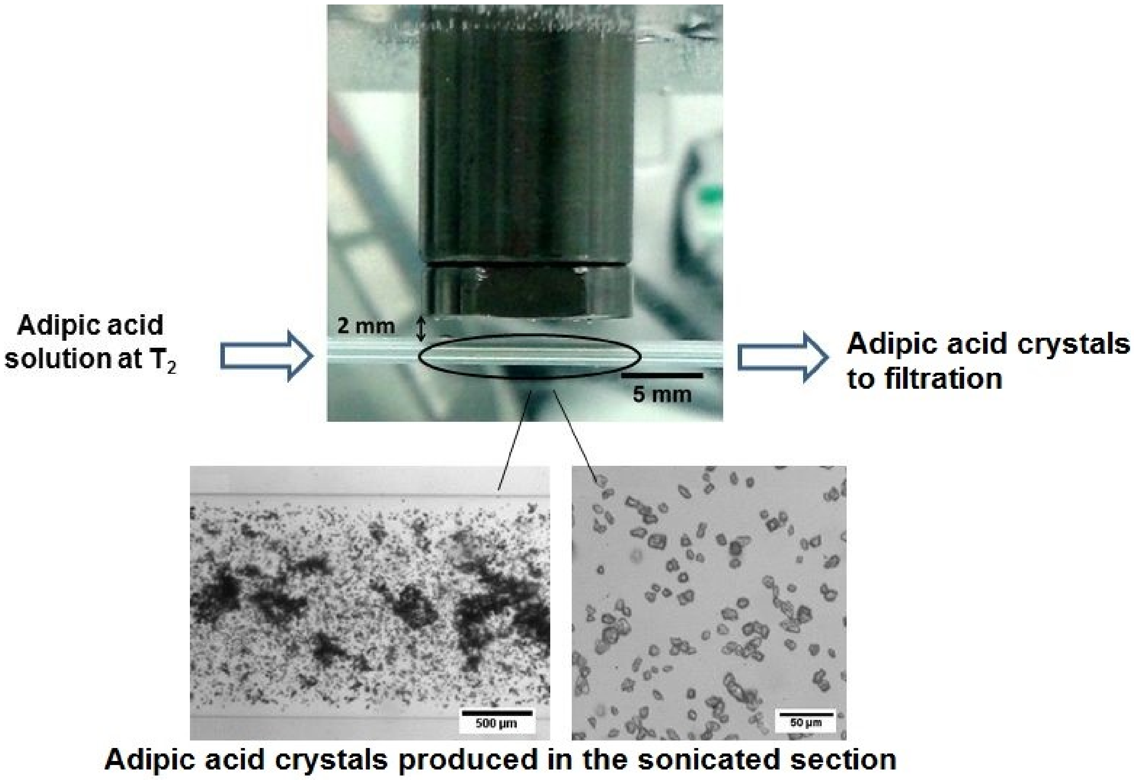

Figure 6.4. Crystal production in the bulk of the sonicated section. S=2.12. 1.55 mm ID capillary.

The distance between the sonoprobe and the capillary outlet is $L_3 = 10\ \mathrm{cm}$. This extra capillary length accounts for the thread length and the space to allocate the refractive index matching device which is implemented in the microscope unit. The capillary is immersed in a plastic box filled with water and fixed by guides that allows movement of the capillary and passing the droplets in front of the microscope lens. Experimental evidence shows that crystal occlusion does not occur in this portion of the capillary.

6.3.2 Effect of sonicated residence time at constant sonicated volume

The sonicated residence time τ_{US} during which the solution is exposed to ultrasound is decreased by increasing the inlet flow rate ($Q_{IN} = 1.5,\ 3,\ 5,\ 10,\ 15\ \mathrm{mL/min}$) in a $1.55\ \mathrm{mm}$ ID capillary tube, which does not present clogging issues. The sonicated residence times τ_{US} are respectively: $1,\ 0.5,\ 0.3,\ 0.15,\ 0.1\ \mathrm{s}$. A supersaturation $S = 2.12$ is chosen. The results of crystal production measured by crystal yield Y (Eq. 5.6) and final mother liquor adipic acid concentration ω_{OUT} as a function of the sonicated residence time are reported in Figure 6.5a and Figure 6.5b, respectively. ω_{OUT} is determined by solving the mass balances in Eq. 6.1 and Eq. 6.2 considering the mass of adipic acid filtered Δm_{filt} for a collection time of $t_{collection} = 30\ s$ and for an initial concentration of adipic acid $\omega_{IN} = \frac{2.12\ \mathrm{g\ AA}}{100\ \mathrm{g\ Water} + 2.12\ \mathrm{g\ AA}} \cdot 100 = 2.076$. The mass balances are written between the inlet and the outlet of the system.

Total mass balance:

$$Q_{IN}\rho_{IN} = Q_{OUT}\rho_{OUT} + \Delta m_{filt}/t_{collection} \qquad \text{Eq. 6.1}$$

Mass balance on the adipic acid:

$$Q_{IN}\rho_{IN\omega_{IN}} = Q_{OUT}\rho_{OUT\omega_{OUT}} + \Delta m_{filt}/t_{collection} \qquad \text{Eq. 6.2}$$

where ρ_{IN} and ρ_{OUT} are respectively the density of the adipic acid solutions at the inlet and at the outlet of the system. We can use the first equation to eliminate $Q_{OUT}\rho_{OUT}$ from the second equation and calculate ω_{OUT}. Due to the very low adipic acid concentration dissolved ρ_{IN} is assumed to be equal to the density of pure water.

The calculated ω_{OUT} values are very similar to those measured using the calibration curve of Figure 6.2. A small difference of about $2-3$ % is observed. The linear trends suggest that crystal production, which can be quantified by Y or ω_{OUT}, is directly proportional to the sonicated residence time τ_{US}. In fact, the sonicated portion of the capillary volume is fixed and the cavitation activity within that volume does not change with the fluid velocity. Therefore, the mass of crystals produced resulting from the complex phenomena of nucleation and growth increases with the time during which ultrasound is applied. As the residence time τ_{US} increases, more crystalline material is generated because of the longer time available for both nucleation and growth processes promoted by the longer cavitation activity. This explains the increase of the crystal yield with τ_{US}. Crystal yield has a minimum of $10\ \%$ at the lowest sonicated residence time and reaches a maximum of $50\ \%$ at the highest residence time.

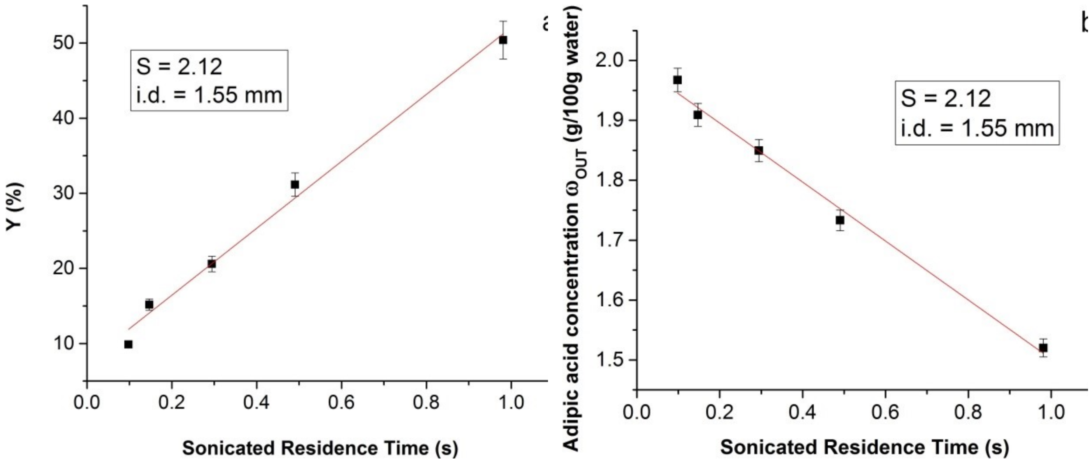

Figure 6.5. Crystal yield (a) and adipic acid final concentration (b) at different sonicated residence times τ_{US}.

The single-phase system has a higher crystal yield compared to the droplet-based system. For a sonicated residence time $\tau_{US} = 0.78\ s$ and supersaturation $S = 2.12$, the droplet-based system has a yield of around $20\ \%$ (Figure 5.12) as compared to the twice higher value provided by the single-phase system (data interpolation of Figure 6.5a). These results are congruent with the fact that bubble cavitation in microchannels is more vigorous at the sidewalls where bubble cavitation is heterogenously triggered by the surface roughness of channel sidewalls that incept and cavitate bubbles in the presence of acoustic waves[136]. The results also agree with the findings of Arora et al.[137], which showed that cavitation occurs in channels of acrylic polymer materials with rough surfaces and does not in smooth ones. The presence of the hexane film in the droplet-based system shields the capillary walls and reduces the overall cavitation activity occurring within the droplets. As a consequence the amount of crystals produced is decreased.

Figure 6.6 and Figure 6.7 show the CDS and the mean size $D_{4,3}$ of crystals for the five sonicated residence times. The system is capable of producing crystals with a mean size of approximately between $10\ \mu\mathrm{m}$ and $30\ \mu\mathrm{m}$ depending on the sonicated residence time τ_{US} (ultrasound cycles), which is quite small compared to the ones produced by other larger-scale continuous sonocrystallization setups[33]. In other words, the current setup gives us the possibility to control the number of ultrasound cycles to which a certain volume of solution is subjected to. Therefore, the mean size of the crystals produced can be controlled by changing the flow rate. Note that, when $\tau_{US} = 1\ \mathrm{s}$, ω_{OUT} is around 0.015. This is value of concentration is below the threshold $S^* = 1.63$ to which corresponds an adipic acid concentration $\omega^* = 0.016$, value at which ultrasound seem to have no longer any effect. Then we may suggest that part of the residence time beneath the probe is ineffective for experiments with $\tau_{US} > 1\ \mathrm{s}$.

Figure 6.6 shows that when the residence time increases, CSDs become broader. The experimental results indicate that the characteristic time of the growth process in presence of ultrasound is similar (in terms of order of magnitude) to the residence time that we considered. Hence, if we increase the residence time by one order of magnitude, the crystals that first nucleated have time to grow significantly. Those, on the other hand, that form later grow less. The CSD thus becomes broader the longer the residence time is.

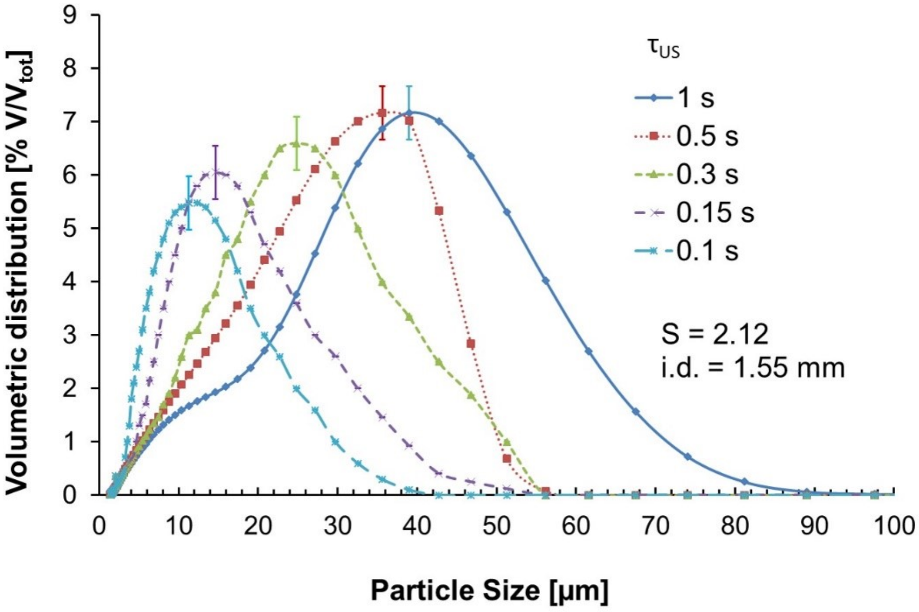

Figure 6.6. CSDs at different sonicated residence times τ_{US}. S=2.12. 1.55 mm ID capillary.

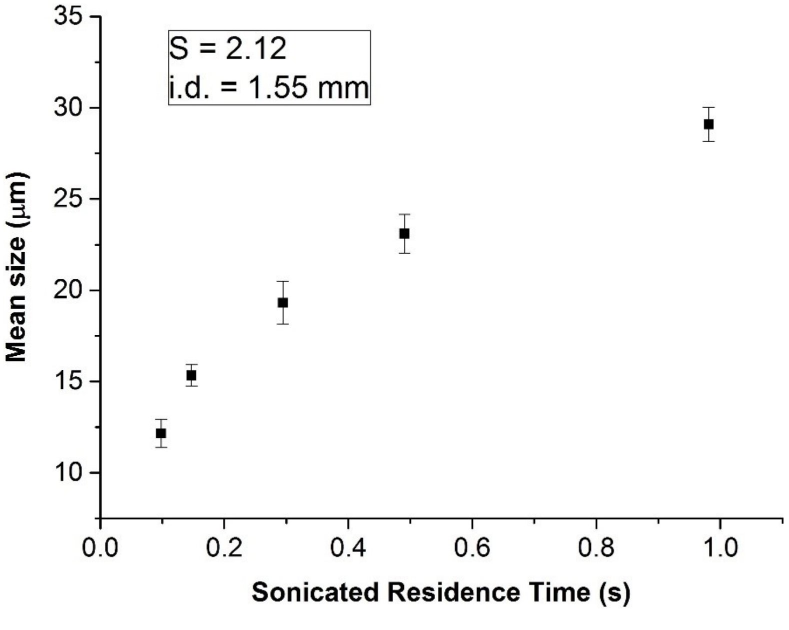

Figure 6.7. Mean crystal size $D_{4,3}$ at different sonicated residence times τ_{US}. S=2.12. 1.55 mm ID capillary.

Figure 6.8 shows crystals obtained from the five different sonication experiments. It can be seen that in presence of ultrasound, crystals have an irregular shape. This might be the consequence of bubbles cavitation which generate microjets and shockwaves promoting surface pitting and crystal erosion[6]. Although it is difficult to distinguish the difference in the shapes of crystals in Figure 6.8a to Figure 6.8e, the snapshots confirm the size trend plotted in Figure 6.7. The lower the residence time τ_{US}, the smaller the crystal size.

The representative standard deviations shown as error bars at the peak of each curve of Figure 6.6 are slightly smaller than the ones obtained in the CSDs of the droplet-based system. In this case, the smaller data variability is probably due to the absence of the carrier fluid and emulsion which makes the filtration process easier, therefore reducing the total experimental error.

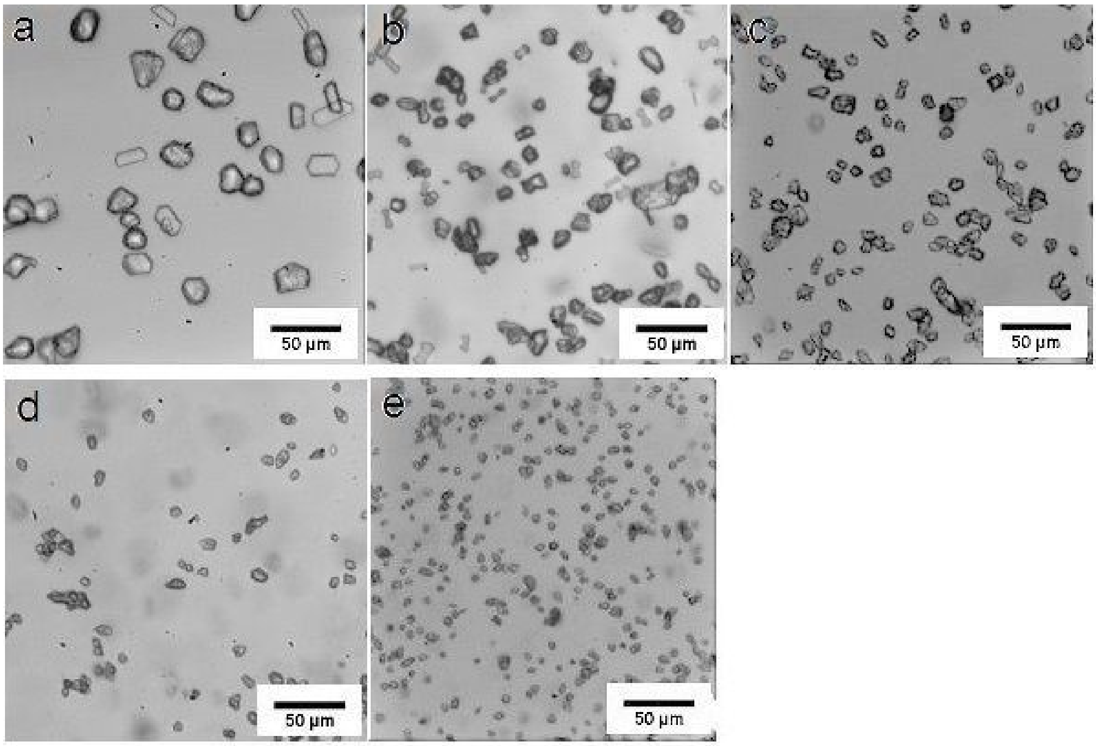

Figure 6.8. Crystal shape at different sonicated residence times τUS (a) 1s, (b) 0.5 s, (c) 0.3 s, (d) 0.15 s, (e) 0.1 s. S=2.12. 1.55 mm ID capillary.

6.3.3 Effect of sonicated volume at constant sonicated residence time

In this section, we increase the volume of the solution that experiences the cavitation activity by increasing the capillary diameter. $1.55,\ 2.4,\ 3.2$ and $4\ \mathrm{mm}$ ID capillary are the selected diameters. To keep the sonicated residence time constant and equal to $1\ s$ the flow rates used are $Q_{IN} = 1.5,\ 3.6,\ 6.4,\ 10\ \mathrm{mL/min}$ respectively. The experiments are performed at the same supersaturations already employed in the droplet-based setup ($S^{*} = 1.63$, $S =$

1.86, $S = 2.12$, $S = 2.39$ and $S = 2.62$). The results of the CSDs are presented in the following figures.

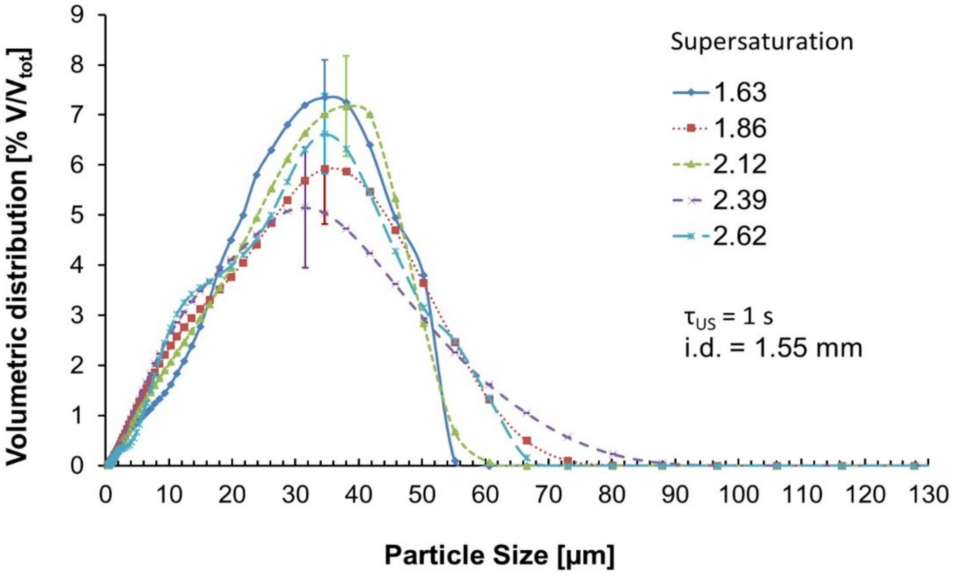

Figure 6.9. CSDs at different supersaturations. τ_{US} = 1 s. 1.55 mm ID capillary.

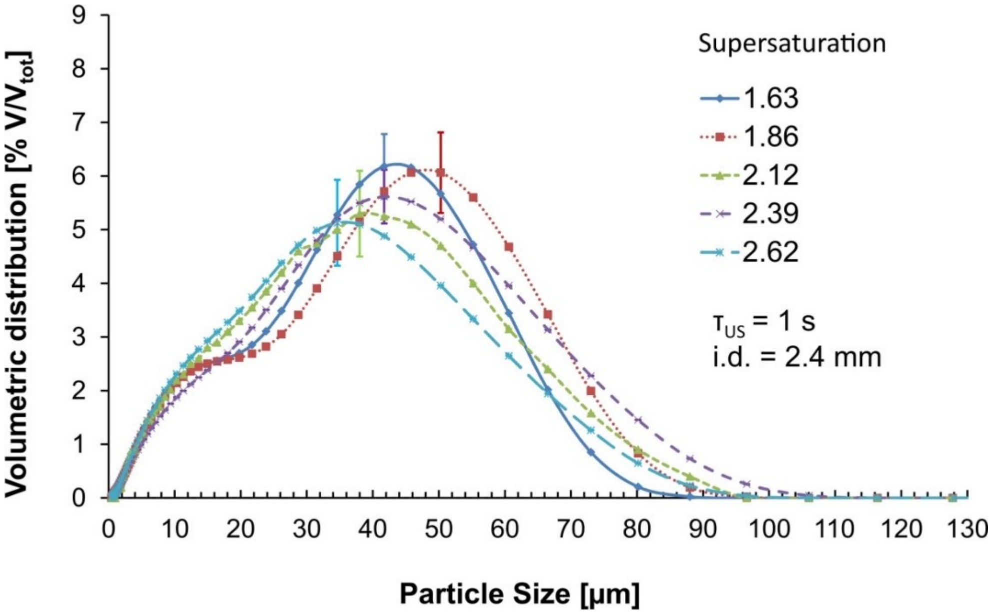

Figure 6.10. CSDs at different supersaturations. τ_{US} = 1 s. 2.4 mm ID capillary.

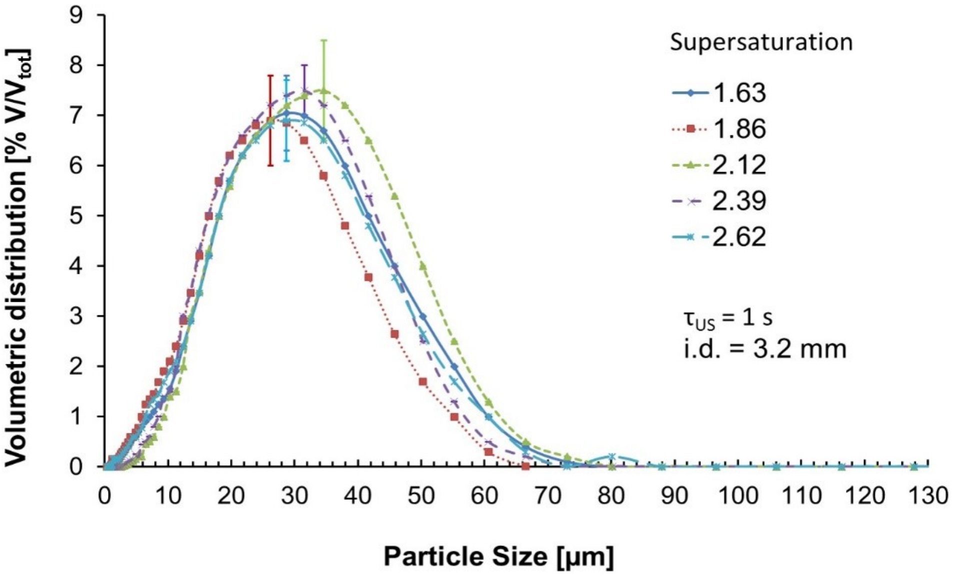

Figure 6.11. CSDs at different supersaturations. τ_{US} = 1 s. 3.2 mm ID capillary.

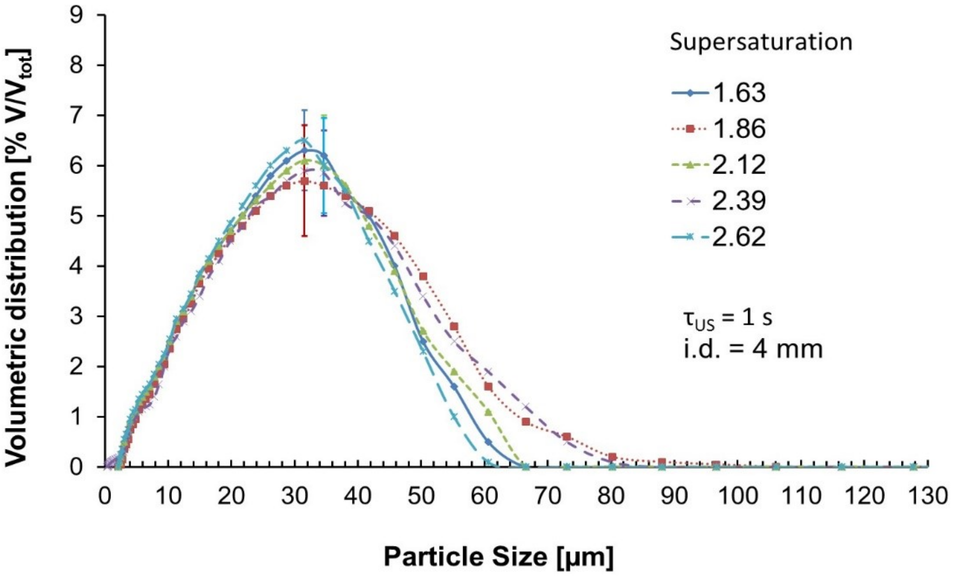

Figure 6.12. CSDs at different supersaturations. τ_{US} = 1 s. 4 mm ID capillary.

The supersaturation level does not have a significant effect on the CSD, and in turn on the resulting mean crystal size (Figure 6.13). This result confirm what has been already observed for the droplet-based system. Regardless of the internal diameter, the mean crystal size remains almost constant and equal to $25 - 30\ \mu\mathrm{m}$, which is in agreement with the size trend reported in Figure 6.7 for a sonicated residence time τ_{US} of $1\ s$. All the CSDs overlap within the experimental error bars for all the supersaturations and internal diameters examined.

Figure 6.14 and Figure 6.15 show respectively the crystal production (yield) and the adipic acid mother liquor concentration. By increasing the supersaturation, crystal yield increases and adipic acid concentration decreases. This is an expected result as the driving force available for crystallization is enhanced. However, the various data do not follow a unique trend but different parallel trends are observed for different capillary internal diameters. Lower crystal yields and higher adipic acid final concentrations are obtained by increasing the capillary diameter. This result can be explained if we consider that the pressure amplitude below the sonoprobe drops rapidly with the distance from the tip (refer to Figure 5.20). As a consequence, the chance of cavitation and sonocrystallization decreases significantly along the sonoprobe axial direction. Sonochemiluminescence experiments of Figure 5.16 show that a change in the capillary position of a few millimetres significantly affects the amount of cavitation activity displayed. It is therefore expected that not the entire volume of the capillary is exposed to the same acoustic pressure. Therefore, the portion that is closer to the sonoprobe experiences higher cavitation activity and more crystal production than the one which is more distant. This is not evident when the capillary diameter increases from $1.55\ \mathrm{mm}$ to $2.4\ \mathrm{mm}$ but becomes relevant when we approach the size of $3.2\ \mathrm{mm}$ and $4\ \mathrm{mm}$. Cavitation activity decreases at those distances and therefore crystal production is reduced. We conclude that the productivity of the single-phase system increases by decreasing the capillary size.

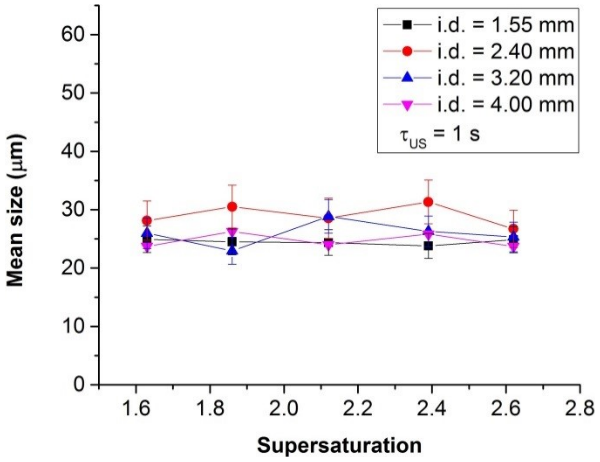

Figure 6.13. Mean crystal size $D_{4,3}$ at different supersaturations and capillary internal diameter. τ_{US} = 1 s.

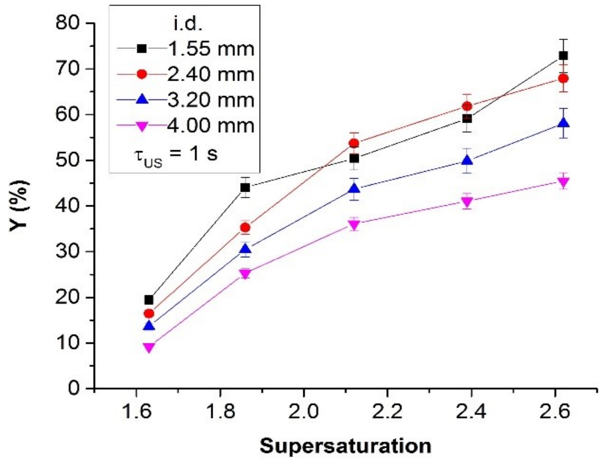

Figure 6.14. Crystal yield at different supersaturations and capillary internal diameter. τ_{US} = 1 s.

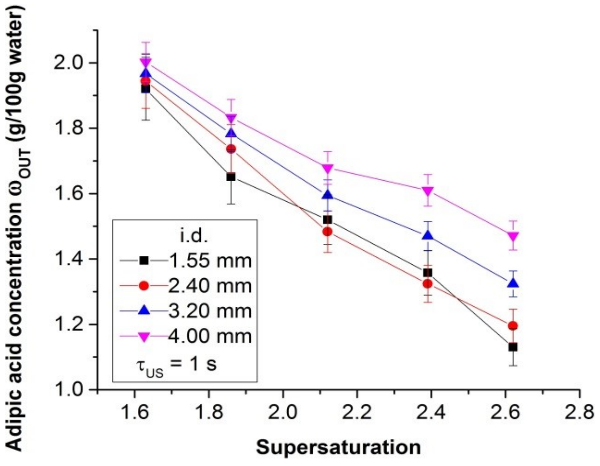

Figure 6.15. Adipic acid outlet concentration at different supersaturations and capillary internal diameter. τ_{US} = 1 s.

Crystal particles suspended in vegetable oil appear to be irregular and fragmented (Figure 6.16). As already mentioned, ultrasound may induce breakage and secondary nucleation by mechanically disrupting crystals or loosely bound agglomerates that have already formed. Solute particles have an increased opportunity to collide with each other because of microstreaming induced by cavitation and high kinetic energy[6,8]. However, this hypothesis will be better examined in the next section.

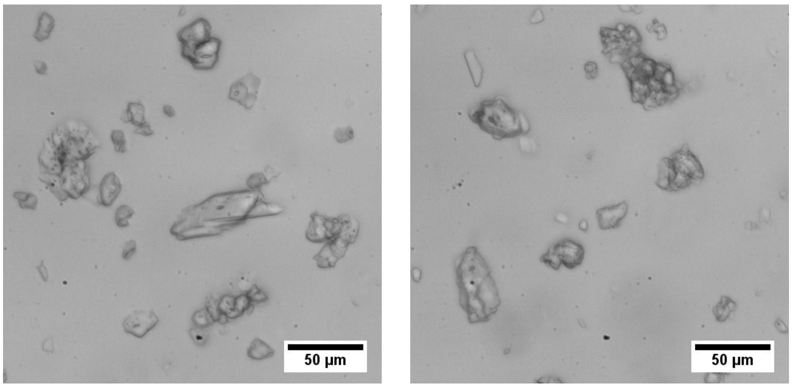

Figure 6.16. Adipic acid crystals after the deagglomeration step suspended in vegetable oil. τ_{US} = 1 s.

6.3.4 Breakage and agglomeration during sonication

To establish whether or not primary particles break up or agglomerate in the capillary during the sonicated residence time τ_{US}, we compare the CSD of the raw adipic acid material (raw particles purchased) with that of the same crystals suspended in a saturated solution and exposed to ultrasound for different τ_{US}. To do so, we ran two experiments with the same experimental setup and conditions described in section 6.3.2 using the upper and lower limits of the range of the sonicated residence times that have been investigated, that are $\tau_{US} = 0.1\ \mathrm{s}$ and $\tau_{US} = 1\ \mathrm{s}$. The CSDs obtained from these experiments are compared to the ones obtained in silent conditions by simply flowing raw crystals suspended in a saturated solution prepared at room temperature ($22\ ^{\circ}\mathrm{C}$). To avoid channel fouling which normally occurs when dealing with particularly large raw crystals in a $1.55\ \mathrm{mm}$ capillary diameter, the raw adipic acid particles are sieved by means of an OCTAGON 200CL Endecotts sieving machine. Only the smallest particles in the size range $45 -$

$53\ \mu m$ are collected and suspended in the saturated solution. The seeds suspension is prepared by adding $2\ g$ of sieved adipic acid crystals to $100\ g$ of saturated solution. The suspension is homogeneously mixed using a magnetic stirrer. A MINIPULS 3 peristaltic pump is used to flow the seeds suspension within the capillary. The seeds are directly filtered and recovered on the filter paper and the same protocol described in section 6.2.1 is then applied to determine the CSD of the final crystalline product (Figure 6.17).

Crystals with size of about $50\ \mu m$ are used because this size is closer to the size of the crystals that the system forms under typical sonicated conditions. Breakage depends on the size of the crystals[1], and so considering in this experiment the right representative size is important.

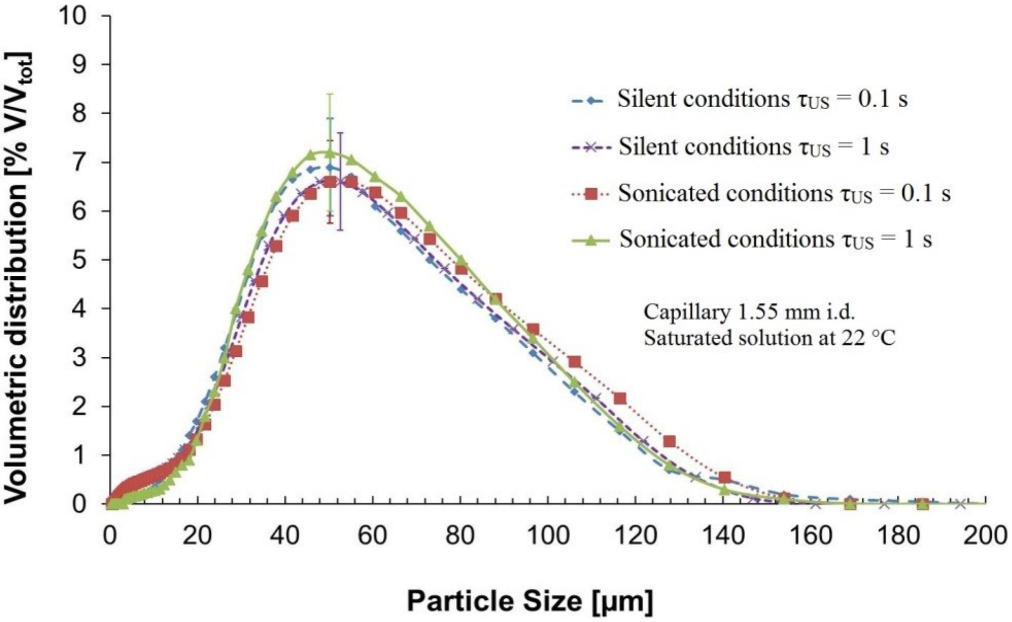

Figure 6.17. CSDs of adipic acid raw crystals exposed to a sonication time τ_{US} = 0.1 s and τ_{US} = 1 s in comparison with the corresponding silent conditions. Crystals suspended in saturated solution at 22 °C. 1.55 mm ID capillary.

The curves clearly overlap, within experimental error, and a constant mean size of around $50\ \mu m$ is measured for each CSD, which is in agreement with the selected range of sieved particles. This result is also confirmed by comparing the crystal pictures of Figure 6.18 that have been captured with a Photron high speed camera (FASTCAM MC1). Crystal snapshots are taken immediately after the sonoprobe within the capillary with the help of the refractive index matching device. The crystal seeds look qualitatively similar and in the size range of about $50\ \mu\mathrm{m}$. The irregular shapes observed are attributed to the milling and grinding processes at which industrial crystals are normally subjected.

As ultrasound does not affect the original particle size distributions at the extreme sonicated residence times employed ($\tau_{US} = 0.1,\ 1\ \mathrm{s}$), it is reasonable to assume that the same applies to the intermediate residence times ($\tau_{US} = 0.5,\ 0.3,\ 0.15\ \mathrm{s}$). As no agglomeration and breakage of primary particles is observed, we can assume that ultrasound is affecting only nucleation and growth in the relatively short residence times of our experiments for the conditions considered.

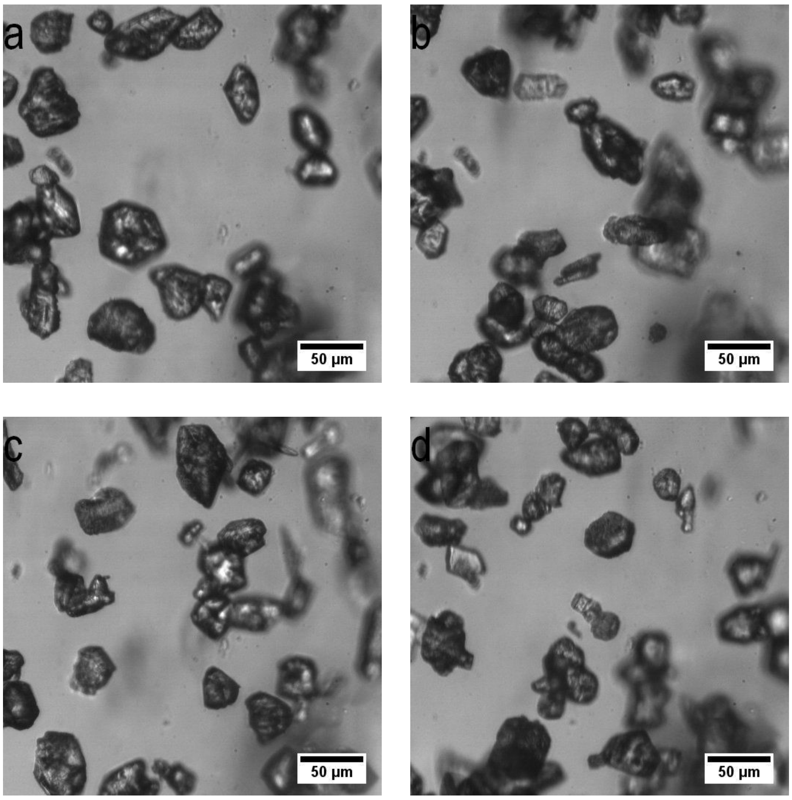

Figure 6.18. Adipic acid raw crystals exposed to different sonication time τ_{US}. (a) silent conditions 0.1 s, (b) silent conditions 1 s, (c) sonicated conditions 0.1 s, (d) sonicated conditions 1 s. 1.55 mm ID capillary. Crystals suspended in saturated solution at 22 °C.

Since the shape of the crystals as well as their surface roughness are not altered by ultrasound, the irregular shape of crystals observed in Figure 6.16 has to be attributed to other mechanisms such as crystal cracking and mother liquor inclusions that likely occur during fast growth processes[1].

6.4 Conclusions

In this chapter, a single-phase microfluidic device for production of adipic acid crystals using ultrasound is presented and investigated experimentally. By exploiting capillary diameters larger than $1\ \mathrm{mm}$, the system developed is able to produce adipic acid crystals without clogging in a reproducible way and with much more flexibility than the droplet-based system. The desired crystal mean size can be easily tailored by changing conveniently the flow rate of the crystallizing solution which is passing through an aligned sonoprobe. Different crystal mean sizes, between 10 and $30\ \mu\mathrm{m}$, can be obtained depending on the fluid flow rates employed. The crystal size distributions and the corresponding mean size of the crystals are independent of the supersaturation level adopted. However, a minimum supersaturation level $S^* = 1.63$ is required to trigger the sonocrystallization process. Crystal yield is improved compared to the droplet-based system due to the removal of the carrier fluid (hexane) that shields the capillary walls and reduces the overall cavitation activity. Crystal yield increases by increasing the supersaturation. The productivity of the process can be further enhanced by using small capillary diameters that can be placed in the zone which experiences the highest cavitation activity (close to the sonoprobe tip). A maximum yield of about $70\ \%$ is obtained at the highest supersaturation employed $S = 2.62$ using the smallest capillary size (ID 1.5 mm).

A set of experiments are finally performed to establish whether ultrasound is also playing a relevant role in breaking or agglomerating the crystals formed within the capillary. Results demonstrate that nucleation and growth appear to be the two main mechanisms that govern sonocrystallization in the single phase crystallizer. Breakage and agglomeration are not affecting the process and therefore the resulting CSDs, crystal shape and crystal production.

7. Towards the development of a growth stage

In this chapter, we focus on the growth stage which is the second fundamental step of the sonocrystallization process. This study represents a preliminary work towards the development and design of the growth stage of the sonocrystallizer.

Part of the material of this chapter has been featured in the following publication:

Rossi, D. et al. Experimental characterization of axial dispersionin coiled flow inverters. ChERD. 120, 159-170 (2017).

7.1 Introduction

In micro and millifluidic devices, the flow behavior is dictated by viscous forces rather than inertial forces, as a result of low operating Reynolds numbers. In devices with simple geometry (such as straight channels), the absence of turbulence makes diffusion the only transport mechanism in the radial direction and, despite the short length scales characterizing the flow, in general this is a rather slow process. A whole branch of microfluidics has been dedicated to the development of complex microstructures capable of achieving faster and effective mixing. Parallel and serial lamination, split and recombination, and flow focusing are examples of passive micromixers designed to shorten mixing times[138,139]. These are effective tools in applications in which fast mixing between different streams is required. However, in many continuous processes what is essential is attaining low fluid dynamic axial dispersion. Approaching plug-flow behavior is required for a wide range of chemical reactions as well as for the synthesis of nano and microparticles[32]. This condition is particularly attractive in this research work for the design of the growth stage. Growth is as much important as nucleation in defining the final size of the crystalline product. In fact, the flow in the channel where crystal growth occurs is expected to be laminar. Hence, due to the parabolic velocity field, the residence time of each fluid element and in turn the crystal growth would vary radially. This would widen the particle size distribution. We need therefore to disrupt the laminar velocity profile while keeping the flow rates and unit dimensions small. Nuclei must be grown under similar conditions for even times. By flattening the velocity profile, one can let crystals reside equal times in the growth unit, thus narrowing down the crystal size distribution. The present chapter deals with the design of a new fluid dynamic strategy to narrow residence time distribution in small channel geometries. The developed fluid dyamic platform could be potentially used to achieve uniform crystal growth in continuous flow processes also offering a potential solution for the design of the sonocrystalizer growth stage (Figure 1.1).

A solution proposed for approaching plug-flow behavior resorts to multiphase segmented flow[140]. Slugs or droplets, behave as small batch reactors travelling through the system, effectively reducing residence time dispersion. However, forming stable slugs or droplets, particularly for cases in which long residence times are needed, can be quite challenging. Furthermore, the introduction of an additional phase requires downstream separation, which may be undesirable in industrial applications. Note that segmented flow has been successfully employed in this work also to overcome the clogging issue when dealing with crystals flowing in milli-channel geometries (see chapter 5). Another solution to reduce hydrodynamic dispersion is employing helically coiled tubes (HCTs), constructed with capillaries on cylindrical supports. These systems have been demonstrated to act positively on the hydrodynamics of tubular systems operating in laminar flow by flattening the velocity profile. Exploiting the action of centrifugal force, one can alter the velocity profile and induce recirculation in the radial direction, resulting in the creation of a secondary flow[141]. Unfortunately, secondary flows are generated predominantly at high flowrates which limits the application of the helically coiled tubes to low residence times.

Oscillatory or pulsed flow offers an effective alternative solution to flatten the characteristic parabolic velocity profile of continuous flow processes reducing the significant hydrodynamic dispersion[142]. To improve the residence time distribution, pulsating flow is normally employed in combination with baffled tubes or furrowed tubular geometries[143]. The basic phenomenon of reducing dispersion is the production of cyclic discrete vortices in the bulk of the fluid. The action of eddy mixing alters the velocity profile and induces recirculation in the radial direction thus narrowing the RTD[144,145,146,147].

Due to the small dimension of the capillaries employed in this work and the absence of baffles that are unsuitable when dealing with crystal particles, we propose to investigate the effect of flow pulsation on the reduction of RTDs in channels with constant cross section (i.e., capillary tubes). This aspect has been poorly addressed in the literature (refer to section 7.2.3) and represents an attractive potential solution for the design of the growth stage of sonocrystallizers.

We present a flexible and reliable experimental procedure to investigate RTD in micro and millifluidic devices that resorts to step input injection and UV-vis inline spectroscopy for the detection of the concentration of a tracer. The procedure is validated using straight tubes and the axial dispersion model developed by Taylor[148].

7.2 Theory

7.2.1 Axial dispersion model

The axial dispersion model (ADM) is an extension of the plug flow reactor (PFR) model that accounts for the longitudinal dispersion of a tracer flowing in the axial direction in straight tubes. The tracer concentration is assumed to be radially uniform. The model is based on the following equation[148]:

$$\frac{\partial C}{\partial t} = -u\frac{\partial C}{\partial z} + D_{ax}\frac{\partial^2 C}{\partial z^2} \qquad \text{Eq. 7.1}$$

where C is the tracer concentration, dependent on the time t and on the axial coordinate z, D_{ax} is the axial dispersion coefficient and u is the mean axial fluid velocity, assumed to be constant. The axial dispersion coefficient is assumed to be independent of both the axial position and the tracer concentration. It relates to the axial dispersion rate in the vessel. To characterize the axial dispersion process under different conditions, one usually adopts dimensionless numbers. In dimensionless form, Eq. 7.1 reads:

$$\frac{\partial \bar{C}}{\partial \tau} = -\frac{\partial \bar{C}}{\partial \xi} + \frac{1}{Pe_L}\frac{\partial^2 \bar{C}}{\partial \xi^2} \qquad \text{Eq. 7.2}$$

where $\tau \equiv tu/L$ and $\xi \equiv z/L$, L being the length of the vessel. $\bar{C}$ denotes the dimensionless tracer concentration (the scaling factor can be chosen arbitrarily, as the equation is linear in the concentration; usually it is chosen to be equal to the inlet concentration). The model features a single parameter known as the Peclet number, $Pe_L \equiv uL/D_{ax}$.

The inverse of Pe_L is the vessel dispersion number N_L. This is a measure of the spread of tracer in the whole vessel. N_L can be regarded as the ratio of the convection time L/u to the dispersion time L^2/D_{ax}; thus, the larger the vessel dispersion number, the broader the RTD is. N_L is widely used to characterize fluid dynamic dispersion and to compare dispersion performance of vessels of different lengths or operated in different fluid dynamic conditions.

Often, a similar group is employed in the literature, defined by using the pipe diameter d_t as characteristic length:

$$N_d \equiv \frac{D_{ax}}{ud_t} \qquad \text{Eq. 7.3}$$

N_d has been widely used to characterize dispersion in dimensionless flow regime maps as a function of the Reynolds number Re[149].

The axial dispersion model can be applied to both turbulent and laminar flows. However, while in the first case there are no limitations to its applicability, for laminar flows the model holds only under certain conditions. These are reported in Figure 7.1, where the system is characterized in terms of the Bodenstein number:

$$Bo \equiv ReSc \equiv \frac{\rho_L u d_t}{\mu_L}\frac{\mu_L}{\rho_L D_m} = \frac{ud_t}{D_m} \qquad \text{Eq. 7.4}$$

(D_m is the molecular diffusion of the tracer) and of the ratio L/d_t. ρ_L and μ_L are respectively the density and the viscosity of the solution. If the point identified by these two coordinates falls within the region of validity of the axial dispersion model, the latter is applicable. The figure also reports the analytical expressions (derived theoretically by Aris (1956)[150] and Taylor (1953)[151] for straight channels) needed to calculate the axial dispersion coefficient. In particular, it is:

$$Bo < 100:\ D_{ax} = D_m + \frac{u^2 {d_t}^2}{192 D_m} \qquad \text{Eq. 7.5}$$

and

$$Bo > 100:\ D_{ax} = \frac{u^2 {d_t}^2}{192 D_m} \qquad \text{Eq. 7.6}$$

These theoretical expressions can be verified experimentally, as described in the following section, by resorting to RTD experiments.

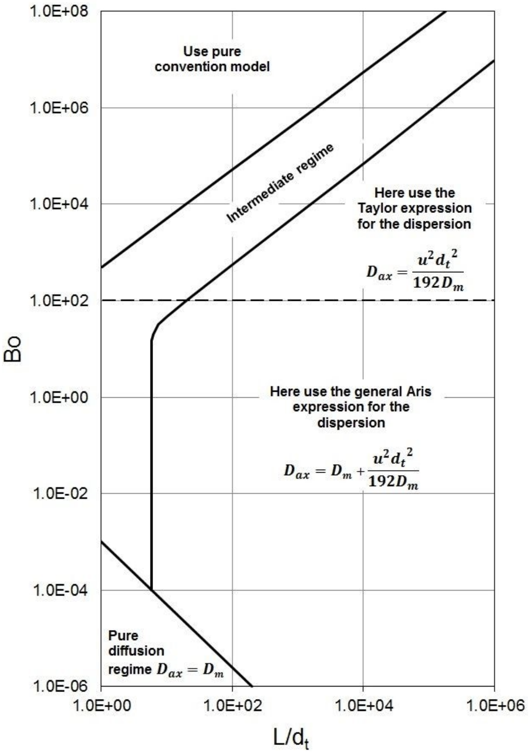

Figure 7.1. Map reporting which flow model to adopt for straight pipes. The operational point can be found on the map knowing the aspect ratio of the pipe and Bo[149].

7.2.2 Calculation of the axial dispersion coefficient

The axial dispersion coefficient D_{ax} cannot be measured directly from experiments; however, it is possible to fit experimental data to the solution of the axial dispersion model (Eq. 7.1). Two different methods of fitting experimental data exist based on the extent of axial dispersion in the system, small ($N_L < 0.01$) and large ($N_L > 0.01$).

For small extents of dispersion, the shape of the RTD curve varies little on passing through the outlet of the vessel (and in particular through the tracer detection system). This means that the resultant experimental RTD curve is close to a Gaussian distribution. In this case, the experimental RTD curve can be fitted with the analytical solution suggested by Levenspiel (1999)[148]:

$$E_{t,ADM} = \sqrt{\frac{u^3}{4\pi D_{ax} L}} \exp\left[-\frac{u(L-ut)^2}{4D_{ax}L}\right] \qquad \text{Eq. 7.7}$$

For large extents of dispersion, the RTD curve changes substantially on passing through the vessel outlet, becoming largely skewed and asymmetrical. In this case, it is fitted to the following curve[148]:

$$E_{t,ADM} = \frac{u}{\sqrt{4\pi D_{ax} t}} \exp\left[-\frac{(L-ut)^2}{4D_{ax}t}\right] \qquad \text{Eq. 7.8}$$

The experimental RTD curves are fitted to Eq. 7.7 or Eq. 7.8 so that the only unknown parameter, D_{ax}, can be calculated.

Note that what happens right at the entrance and exit of the vessel strongly affects the shape of the tracer curve and therefore the values of the fitted D_{ax} parameter. Two types of boundary conditions (b.c.) can be considered: either the flow is undisturbed as it passes the entrance and exit boundaries (open b.c.), or we have plug flow outside the vessel up to the boundaries (closed b.c.). This leads to four combinations of boundary conditions, closed-closed, open-open, and mixed. Analytic expression for the E curve is not available for closed vessels and E curves can be only derived by numerical methods. Conversely, open vessel represents a convenient and commonly used experimental device. It is the only physical situation (besides $N_L < 0.01$) where the analytical expression for the E curve is not too complex (Eq. 7.8)[148].

This study focuses on unsteady oscillatory flows and HCTs, not on straight pipes; therefore, there is no guarantee that the axial dispersion model holds and that an axial dispersion coefficient can be used to quantify the axial dispersion in these systems. This needs to be verified.

The analytical solution (either Eq. 7.7 or Eq. 7.8) to use depends on the vessel dispersion number N_L, which is unknown before performing the fitting. As a consequence, the fitting is carried out using both solutions and then selecting the correct one. The fitting is based on the least squares method and the residual error ε of the solution is used to judge the quality of the fitting. The error ε is so calculated:

$$\varepsilon = \sum_i \left[\left(E_{t,ADM}(D_{ax}, t_i) - E_{t,exp}\right)\right]^2 \qquad \text{Eq. 7.9}$$

where $E_{t,ADM}(D_{ax}, t_i)$ is the value of analytical RTD curve at any time t_i and $E_{t,exp}$ is the corresponding value of the experimental RTD curve.

This parameter is used to propose a criterion for the applicability of the ADM in apparatus different from straight channels and/or in unsteady flow conditions (see section 7.4.2), for which flow maps, such as that reported in Figure 7.1, are not available.

7.2.3 Unsteady oscillatory flow

In oscillatory flows, the velocity of the fluid changes periodically in time; it can vary, for instance, sinusoidally or with a step-like pattern. Oscillatory flows in channels are in general characterized by three dimensionless parameters: the Reynolds number Re, the amplitude ratio α and the Strouhal number St. The Strouhal number is a measure of the ratio of inertial forces due to the unsteadiness of the flow, or local acceleration, to the inertial forces due to changes in velocity from one point to another in the flow field. It can be also regarded as the ratio between the time that characterizes convection d_t/u, where u is the average velocity of the fluid across the cross section of the tube and d_t is the diameter of the tube, and the pulse period T (inverse of the pulsation frequency f). d_t denotes the length scale that characterizes the velocity gradients which is the length over which the velocity changes significantly. The amplitude ratio α is defined as the ratio between the volume flow rate step increment $Q_{max} - Q$ due to the oscillations and the average volume flow rate Q. These dimensionless numbers are given by the equations below:

$$Re = \frac{\rho_L u d_t}{\mu} \quad ; \quad St = \frac{f d_t}{u} \quad ; \quad \alpha = \frac{Q_{max} - Q}{Q} = \frac{Q - Q_{min}}{Q} \qquad \text{Eq. 7.10}$$

A typical step-like pulsation pattern is pictured in Figure 7.2. When $\alpha = 0$, $Q_{max} = Q_{min} = Q$ and no pulsation occurs. For $0 < \alpha < 1$, $Q_{max} > 0$, $Q_{min} > 0$ and the fluid flow is unidirectional. When $\alpha = 1$, $Q_{max} = 2Q$ and $Q_{min} = 0$. When $\alpha > 1$, $Q_{max} > 2Q$, $Q_{min} < 0$ and flow reversal occurs during the negative cycle of the pulsation.

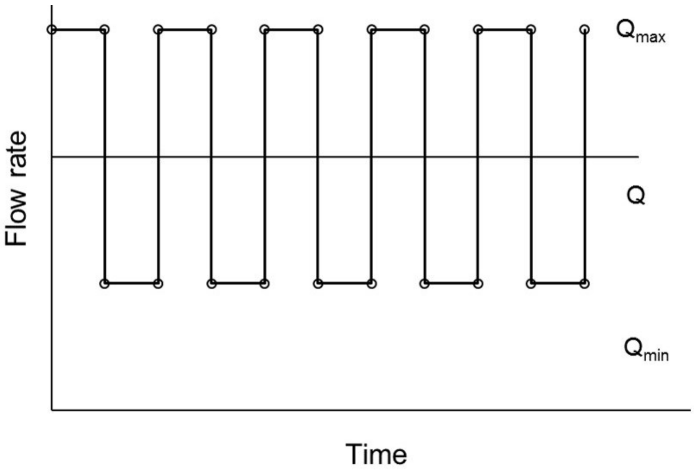

Figure 7.2. Step-like flow pulsation pattern.

The dimensionless numbers defined in Eq. 7.10 are useful in characterizing the dynamic behavior of unsteady flows; by changing pulsation frequency, average flow rate and amplitude ratio, we will be able to change their values and correlate them to a specific velocity profile and RTD. Particularly, at low Reynolds numbers *O*(1), where *O* indicates the order of magnitude, viscosity dominates the flow and oscillation does not have effect. At medium Reynolds number *O*(10) inertia plays a role causing collective oscillating movement of the fluid. In this condition if the Strouhal number is *O*(1) the fluid velocity changes generate vortices at the channel walls that enhance radial mixing. Hence, flat velocity profiles are achieved and consequently narrow RTDs and small axial dispersion. If Strouhal number is $O(10^{-4})$, a quasi-steady-state flow establishes, the effect of oscillations diminishes and almost parabolic Poiseuille velocity profiles and large axial dispersion ensue[152,153].

One of the first researchers to look into the effects of pulsating flow on solute dispersion in the axial direction was Aris (1960)[154]. A mathematical model was developed showing that oscillatory flow only took notable effect when fluctuations of the pressure gradient were larger than that of the mean pressure gradient. However, this was not proved experimentally. Chatwin (1975) next looked into the effects of oscillatory flow on fluid dispersion[155]. The paper examines theoretically how a passive contaminant disperses along the axis of a tube in which the flow is driven by a longitudinal pressure gradient varying harmonically with time. The ADM discussed in section 7.2.1 does not account for a fluid velocity which fluctuates with time. Eq. 7.1 describes the tracer mass balance in steady flow whereby the velocity is constant and, consequently, so is D_{ax}. It was found by Chatwin (1975) that if for oscillatory cases, u and D_{ax} are periodic functions of time, the harmonic terms in $D_{ax}(t)$ have a noticeable effect on the dispersion of the contaminant and in particular on the rate at which it is spreading axially. The size of the effect depends on both the frequency and the Schmidt number and is particularly large at low frequencies. Mukherjee et al. (1988) analyzed theoretically the effect of D_{ax} in oscillatory laminar flow, which was in turn consistent with Chatwin's work[156]. The authors found that the oscillation amplitude of $D_{ax}(t)$ increased with wave amplitude but decreased with wave frequency. It was also found that the value of $D_{ax}(t)$ could fluctuate between negative and positive values depending on its oscillation amplitude, much like the fluid velocity. In oscillatory flow, Mukherjee et al. (1988) found that the time-averaged dispersion fluid rate increased with time until a specific dimensionless time was reached. Thereon after, the time-average rate of dispersion was constant[156]. Vedel et al. (2012) continued the work of Mukherjee et al. (1988) reiterating the fact that $D_{ax}(t)$ oscillates around the time-averaged D_{ax} (where the time averaged value are for times tending to infinity)[157]. However, Vedel et al. (2012) have taken this work a step further. They found that for small oscillation amplitudes ($\alpha < 1$), $D_{ax}(t)$ oscillates around the steady flow value of D_{ax}. This indicates that the extent of fluid dispersion is relatively unchanged in comparison to steady laminar flow. This is consistent with Aris (1960)'s mathematical model and may give rise to the possibility of oscillatory flow RTD experimental data being fitted to the ADM for small oscillation amplitude. Some authors investigated experimentally the conditions where oscillating baffled tubes can operate in a near plug flow mode also providing evidence of flow visualization of radial and axial eddy mixing: Zheng et al. (2008)[144], Dickens et al. (1989)[145], Olayiwola et al. (2011)[146] and Brunold et al. (1989)[147] have studied the effect of dimensionless parameters on RTD and axial dispersion coefficient for different baffled reactors. The authors reported improved fluid dynamics and proposed a correlation for the axial dispersion coefficient as a function of reactor geometry, baffles position, Re, α and St. However, the authors did not consider whether the axial dispersion model could be applied to non-straight channels and unsteady flows.

In the present work we study the effect of the dimensionless parameters on the reduction of the axial dispersion coefficient. To assess the performance of the pulsation pattern and the corresponding residence time distribution, we present stimulus-response analyses. This allows us to identify the optimal experimental conditions that minimize RTD spread and D_{ax}. Large amplitude ratios and flow reversal are also examined and a criterion of applicability of the axial dispersion model is established when dealing with non-straight tubes and unsteady flows.

7.3 Experimental section

In this section, we describe the experimental setup and procedure employed for the generation of the pulsating flow.

7.3.1 Experimental setup

The experimental setup is shown in Figure 7.3. $100\ \mathrm{mL}$ SGE glass syringes are filled with carrier fluid (deionized water) and tracer fluid (aqueous solution of Basic Blue 3). This is an organic dye highly soluble in water and it has been used in the past for RTD characterization. Bošković and Loebbecke (2008) found that Basic Blue interacts poorly with the surface of Teflon tubing, such as PFA, as compared to other tracers[158]. Using a syringe pump (Harvard PHD 2000 programmable), the fluids are simultaneously pumped to a six-way injection HPLC valve which allows switching between the tracer and the carrier fluid flowing within the channel; one fluid is disposed as waste, while the other is fed to the channel. Different step-like pulsation patterns are induced by means of an additional syringe pump mounted with a $100\ \mathrm{mL}$ SGE glass syringe filled with deionized water and connected to a PEEK T-junction ($1\ \mathrm{mm}$ ID) using 20 cm PFA tube ($1\ \mathrm{mm}$ ID) filled with water as well. This pump can generate an oscillatory flow rate with a chosen amplitude ratio α and pulsation frequency f delivering the pulsating pressure to the connected main channel. This is an alternative and easy method of generating an oscillatory motion to the most common methods such as scotch yoke mechanisms generally employed with baffled tubes[142,143]. The inlet of the main channel is directly connected to the T-junction which is very close to the HPLC valve so as to achieve a sharp step input directly at the inlet boundary (Figure 7.4). This makes RTD deconvolution not necessary for our system. Note that we never observed the tracer spreading into the pulsating syringe.

Initially the carrier fluid flows through the channel; at a time t_0, the feed is abruptly switched to tracer fluid, generating a step in tracer concentration. At the channel outlet, an optical fiber, connected to a light source (Ocean Optics DH-2000-BAL), shines light through the channel (PFA capillary), which passes through a flow cell. The light that passes through the fluid reaches, via another optical fiber, a spectrophotometer (Ocean Optics USB2000+UV-VIS-ES) whereby light intensity is measured at small regular time intervals.

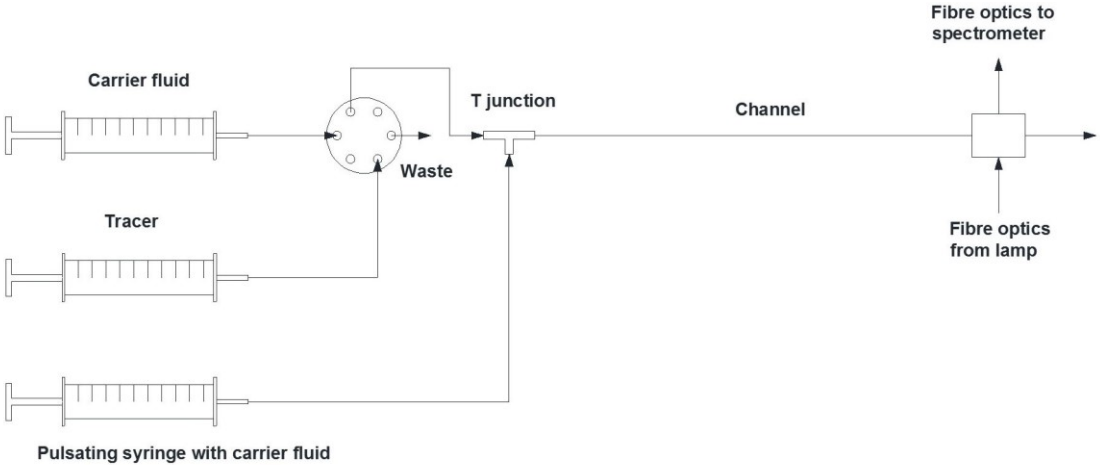

Figure 7.3. Experimental setup schematic to investigate RTDs in micro and millifluidic channels using pulsating flow.

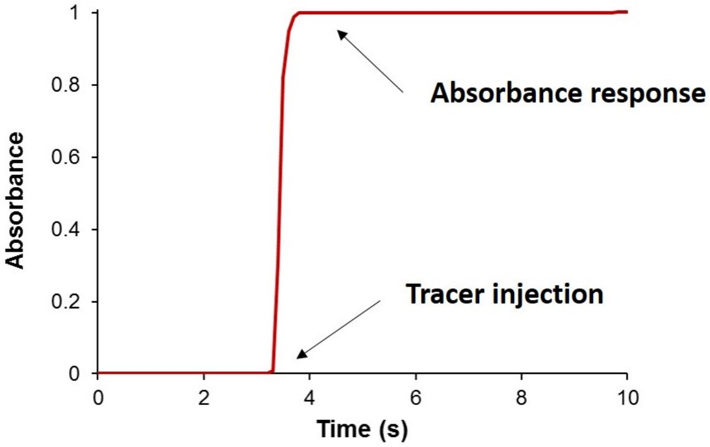

Figure 7.4. Step tracer injection immediately after the T-junction. Straight tube. Amplitude ratio = 9, Strouhal number = 0.188, capillary length = 5 m, capillary internal diameter = 1 mm, average flow rate = 1 mL/min.

7.3.2 Effluent tracer and RTD measurement

The tracer concentration is measured at the channel outlet to determine the RTD. To do so, the Lambert-Beer law (Eq. 7.11) is used. This is a linear equation, valid at low tracer concentrations, that relates concentration to light absorption. Tests are conducted at different tracer concentrations to check the validity of the law. PFA capillaries with $\mathrm{ID}\ = 1\ \mathrm{mm}$ and $\mathrm{OD}\ = 1.58\ \mathrm{mm}$ are used for calibration. The absorbance is measured in stagnant conditions and three readings are taken. A deviation from linearity is observed at tracer concentrations greater than $200\ \mathrm{mg/L}$ (Figure 7.5). We therefore set the tracer concentration at the channel inlet equal to $100\ \mathrm{mg/L}$.

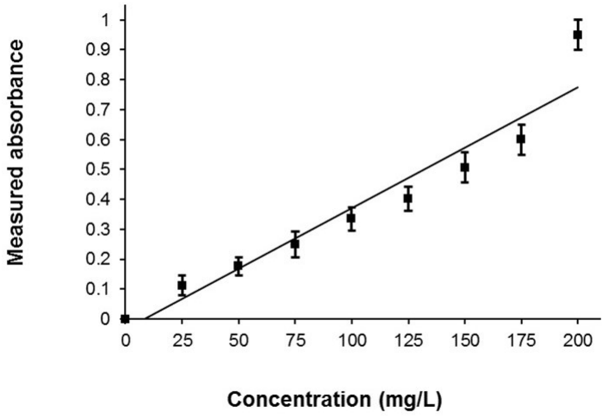

Figure 7.5. Absorbance calibration in 1 mm ID PFA tube at different tracer concentrations.

The Lambert-Beer law reads:

$$\mathrm{A} = -\log\left(\frac{I}{I_0}\right) = \varphi l C \qquad \text{Eq. 7.11}$$

where I is the intensity of the light detected by the receiving sensor and I_0 is the intensity of the light emitted, φ is the extinction coefficient (a property of the medium), l is the distance between the emitting light and the receiving sensor and C is the concentration of the tracer. The absorbance A is found as described below.

As described in the previous section, the optical detection takes place in a non-intrusive flow cell made of a rectangular aluminum block with four holes, one at the centre of each lateral side (Figure 7.6). Two of them allow fitting the channel passing through the cell, while the other two accommodate the optical fibers. With this configuration the channel and the optical fibers are perpendicularly aligned to each other. The light beam leaving the channel via the optical fiber reached the spectrophotometer that measured its mean intensity (Figure 7.7). The light intensity depended entirely on the tracer concentration of the fluid present at the reactor outlet, because the carrier fluid and the tracer absorb light at different wavelengths. The highest absorbance peak is around $650\ \mathrm{nm}$ as showed in the absorbance spectrum in Figure 7.8. To obtain smoother absorbance readings, the absorbance is averaged over a narrow range of wavelengths around the peak ($645 - 660\ \mathrm{nm}$). The mean intensity measurements in the spectrophotometer are converted into absorbance values by using Eq. 7.11.

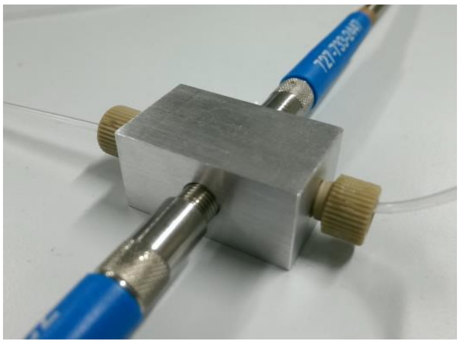

Figure 7.6. Custom designed non-intrusive flow cell.

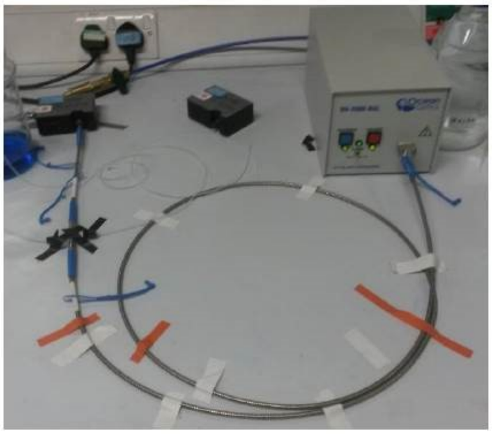

Figure 7.7. Flow through cell, optical fibers, spectrometer and light source setup.

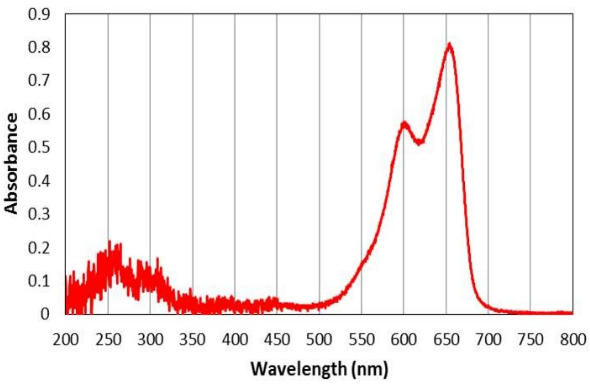

Figure 7.8. Absorbance spectrum of 100 mg/L Basic Blue 3 solution detected with in-line UV-VIS spectrometers.

For *t*<*t₀*, only the carrier fluid occupied the channel; this intensity value is taken and used as reference value. In Eq. 7.11, this value is I_0. For *t*>*t₀*, the light intensity I is measured. If the tracer concentration in the fluid that passes through the reactor outlet were zero, the intensity measurement would be approximately equal to I_0, the absorbance vanishing. For nonzero tracer concentrations, the light intensity decreases due to absorption at the $645 - 660\ \mathrm{nm}$ wavelengths, thus increasing the absorbance. Intensity measurements are taken at very small time intervals, thus enabling the absorbance to be plotted against time. Measurements are recorded using the Ocean Optics Spectra Suite software.

A MATLAB script is written (see Appendix) to normalize and smooth the collected tracer concentration data $C(t)$ in order to reduce the noise in the measurements. Another data processing code (see Appendix) is used to differentiate the cumulative RTD data from the first code. The RTD curve is thus produced. The transformation of the experimental concentration curve $C(t)$ to the cumulative RTD curve $F(t)$ is achieved by normalizing the tracer concentration over the time:

$$F(t) = \frac{C(t)}{C_{max}(t)} \qquad \text{Eq. 7.12}$$

where $C_{max}(t)$ is the maximum asymptotic tracer concentration at the channel outlet.

A final MATLAB script (see Appendix) is used to differentiate the data from the first code. The RTD curve is thus produced. Differentiating Eq. 7.12 gives the experimental RTD curve:

$$E(t) = \frac{dF(t)}{dt} \qquad \text{Eq. 7.13}$$

In the general case of velocity and concentration dependent on the radial position, the quantity that one needs to use to obtain $E(t)$ must be the mixing-cup concentration $C_{mix}(t)$[148]. Accordingly, the analytical instruments used for detecting the concentration of tracer in residence time distribution experiments should measure the mixing-cup concentration $C_{mix}(t)$. The concentration that most instruments measure is the through-the-wall average concentration $C_{tw}(t)$. However, when the spread of tracer in the radial direction due to fluctuations of different flow velocities and molecular and turbulent diffusion takes place in a time much smaller than the vessel mean residence time, the gradient of radial concentration is flattened. If this is the case the concentration does not depend on the radial position; therefore, we can assume that $C_{tw}(t)$ = $C_{mix}(t)$ = $C(t)$. As a result, when the concentration is evenly distributed over the cross section where the detection takes place, both mixing-cup and through-the-wall concentrations lead to the same result. As reported in literature this condition is easily to obtain in very small channel geometries such as micro and millli channels[148]. As a result, the RTDs calculated using Eq. 7.13 are correct.

Note that, the same RTD curves obtained using a step tracer fluid injection could be derived using a pulse tracer fluid injection. This would obviously require a different mathematical formulation to get $E(t)$ from $C(t)$. However, when performing pulse input experiments, often one needs to employ concentrations of tracer quite large to get an appreciable signal at the detection point. This is particularly encountered when dealing with significantly dispersive vessels. If the RTD system is characterized by two detection points, the one closest to the injection point may experience non-linear effects as a result of the high concentration adopted. Furthermore, even when working with a single detector, the effect of the tracer flowing properties may be detrimental on the measured RTDs. Conversely, in step input experiments the maximum tracer solution is continuously injected into the vessel, as opposed to a single shot in pulse experiments. This makes it possible to adopt much smaller concentrations; thus, step input experiments are more reliable when one resorts to absorbance-based detectors.

7.3.3 Design of helically coiled tubes

The HCT is constructed using a PVC straight tube as supporting frame. PFA capillary with different internal diameters are coiled on the PVC frame. The capillary is firmly secured on the supporting frame using cable ties (Figure 7.9).

Before presenting the design of the HCT in this work, the following dimensionless numbers need to be introduced.

- *Coil-to-tube diameter ratio*, λ. This number is related to the effect of centrifugal force on the flow.

  $$\lambda \equiv \left(D_s + \frac{d_e}{2}\right)\frac{1}{d_t} \qquad \text{Eq. 7.14}$$

  where D_s is the diameter of the cylindrical support and d_e is the external diameter of the tube (i.e., the channel). Decreasing λ results in stronger centrifugal force; this is consequence of the increased curvature of the tube. The coil-to-tube diameter ratio is a crucial design parameter. However, few studies have been devoted to its effect on the fluid dynamics[159,160].

- *Dean number, De*. This number relates to the balance among inertial, centrifugal and viscous forces.

  $$De \equiv Re\lambda^{-0.5} \qquad \text{Eq. 7.15}$$

  As De becomes small (less than unity), viscous forces become dominant and the effect of the centrifugal force vanishes. There exists a critical value of De (for any fixed value of λ and Re) above which the effect of secondary flow enhances the reduction of axial dispersion. However, data in the literature do not identify univocally this value for different Re and λ[160]. Saxena et al. (1984) mentioned that in practice at least two turns around the coil are required for developing a secondary flow in the cross-sectional plane in laminar flow[141].

Our focus in this work is on the effect of the pulsation on straight and helically coiled tubes. To do so, we compare the performance of a $L = 5\ \mathrm{m}$ straight capillary ($\mathrm{ID}\ = 1\ \mathrm{mm}$ and $\mathrm{OD}\ = 1.58\ \mathrm{mm}$) with the same capillary arranged in a coil structure having an external diameter $D_s = 17\ \mathrm{mm}$ and 80 turns. A coil-to-tube diameter ratio $\lambda = 17.8$ is then fixed for our HCT. The inlet of the HCT is directly connected to the T-junction, so as to achieve a sharp step input directly at the inlet boundary. Its outlet is directly connected to the flow through cell. Note that, the $5\ \mathrm{m}$ straight tube is kept perfectly on a straight line by placing it on the horizontal laboratory bench to avoid any bending and twisting. These random changes of direction might promote the occurrence of secondary flow and chaotic mixing thus altering the comparison between the straight and the HCT configurations.

Figure 7.9. HCT constructed. PFA capillary 1 mm ID and 1.58 mm OD. External diameter of the coil structure = 17 mm. Number of turns = 80. λ=17.8.

7.4 Results and discussion

7.4.1 Determination of the molecular diffusion of the tracer

In this section, we report how we determine the molecular diffusion coefficient D_m in the tracer of the carrier fluid employed. The exact value of D_m for Basic Blue 3 is not known as only a range of values for D_m is available in the literature[161].

As discussed in section 7.2, when Bo is greater than 100, the molecular diffusion coefficient D_m in Eq. 7.5 can be neglected and therefore Eq. 7.5 reduces to Eq. 7.6, which can be rearranged as:

$$D_m = \frac{u^2 {d_t}^2}{192 D_{ax}} \qquad \text{Eq. 7.16}$$

This equation can be used to determine the molecular diffusion coefficient from RTD experiments in straight tubes according to the following procedure:

- RTDs are measured in a straight capillary with aspect ratio $L/d_t = 5000$ $(L = 5\ \mathrm{m}, d_t = 1\ \mathrm{mm})$ under different values of the Reynolds number by varying the fluid flow rate from $0.025\ \mathrm{mL/min}$ to $1\ \mathrm{mL/min}$. A step tracer injection is used. According to Eq. 7.4, $Bo \equiv Re \cdot Sc$; therefore, when changing Re, the point representing the fluid dynamic condition of our system in the flow map regime of Figure 7.1 follows a vertical line.
- The experimental RTD curves are fitted with the analytical solutions of the ADM to obtain the axial dispersion coefficients D_{ax} using the method outlined in section 7.2.1.
- The values of the molecular diffusion coefficient D_m are calculated using Eq. 7.16 and plotted against Re in Figure 7.10.

We observe that when $Re < 2$ the calculated axial diffusion coefficient D_m is constant, equal to $6.4 \cdot 10^{-10}\ \mathrm{m}^2/s$, while for larger values of Re it increases. The increase does not have physical basis: being an intrinsic transport property of the water-tracer system, D_m can not be a function of Re. We conclude that the correct value of D_m is $6.4 \cdot 10^{-10}\ \mathrm{m}^2/s$. This value lies within the measured range of values ($3.78 \cdot 10^{-10}$ – $6.63 \cdot 10^{-10}\ \mathrm{m}^2/s$) of the molecular diffusivity of Basic Blue 3 in water available in the literature[161].

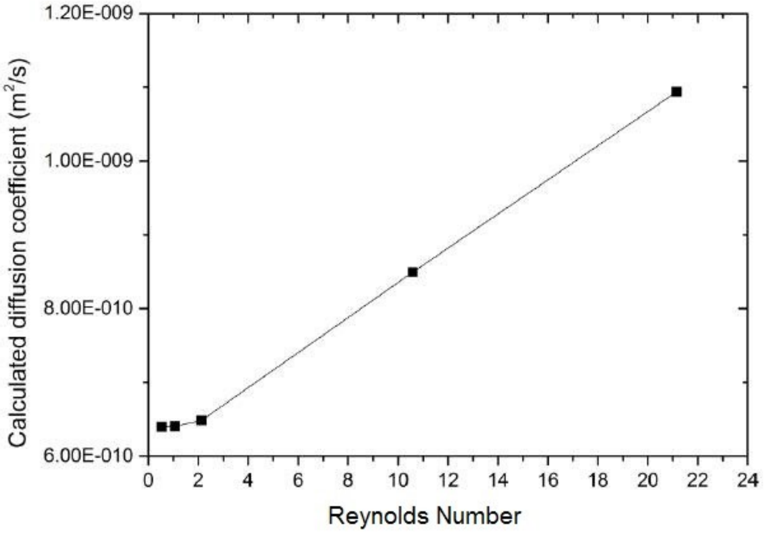

Figure 7.10. Calculated diffusion coefficient of Basic Blue 3 in water as a function of Re.

Once the correct value of the coefficient of molecular diffusion is established, we can calculate the Bodenstein numbers for the experiments carried out and plot the operating points on the flow regime map (see Figure 7.11). It can be clearly observed that the experimental operating point obtained at the lowest flow rate of $0.025\ \mathrm{ml/min}$ (Re=0.5) is positioned in the centre of the region of full applicability of the ADM. Here $\mathrm{Bo}=829 > 100$ and therefore Eq. 7.16 is valid. Increasing the flow rate, the operating point moves on the vertical line L/d_t=5000 to higher values of the Bodenstein number. In particular, for a flow rate of $0.1\ \mathrm{mL/min}$, Re=2 and $\mathrm{Bo}=3320$. This value of Re, beyond which the coefficient of molecular diffusion is no longer constant, identifies the threshold in Figure 7.11. The incorrect values of D_m obtained for Reynolds numbers above this threshold value are due to the fact that the operating point is near the line separating the intermediate region from the zone of full applicability of the model, so that Eq. 7.16 does not hold perfectly. At the highest flow rate $1\ \mathrm{mL/min}$ (Re=21.1) the operating point meets the line separating the intermediate region from the zone of full applicability of the model ($\mathrm{Bo}=3.32\cdot10^4$) and Eq. 7.16 overestimates D_m.

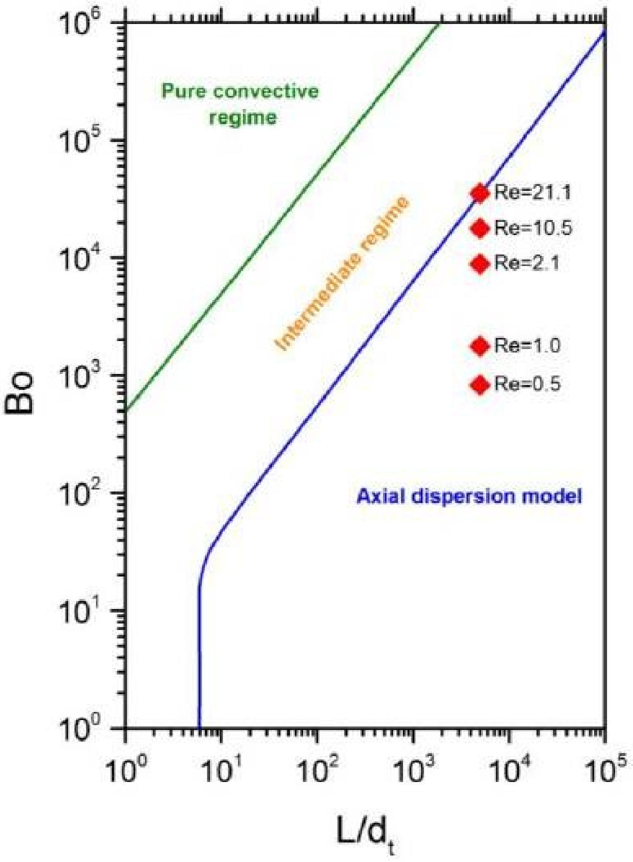

Figure 7.11. Operating points on the flow regime map. Range of applicability of the ADM.

7.4.2 Criterion for applicability of the axial dispersion model in non-straight tubes and unsteady flow

In this section we introduce a general criterion for judging whether the ADM is applicable or not in geometries different to straight pipes and/or unsteady flow.

As discussed in the previous section, to use Eq. 7.16, one must perform experiments under full applicability of the dispersion model, the validity of which depends on the value of Bo (see Figure 7.1). The ADM developed by Aris and Taylor is derived for straight pipes and steady flow, and therefore it might be invalid for other channel geometries and fluid dynamic conditions. In this regard, a procedure to gather information on the applicability of the axial dispersion model is described below.

We calculate the fitting errors ε at the different flow rates employed (0.025 to 1 $\mathrm{ml/min}$) and we reported the values of ε as a function of the Reynolds number investigated (Figure 7.12). From the plot one can clearly observe that the residual error increases with Re. This is because the higher the value of Re is, the greater the value of Bo becomes (see Figure 7.11). At high values of Bo, the system operates near the limit beyond which the ADM is no longer valid. As a result, the error ε increases while the system approaches this limit.

The experiments close to the boundary with the intermediate regime (Re=21.1) generate the greatest error, while the residual error, and in turn the quality of the fitting, improves as Re decreases. For this reason, we identify $\varepsilon_{cr}=10^{-3}$ as the critical value of the residual error that one should use in judging the applicability of the model.

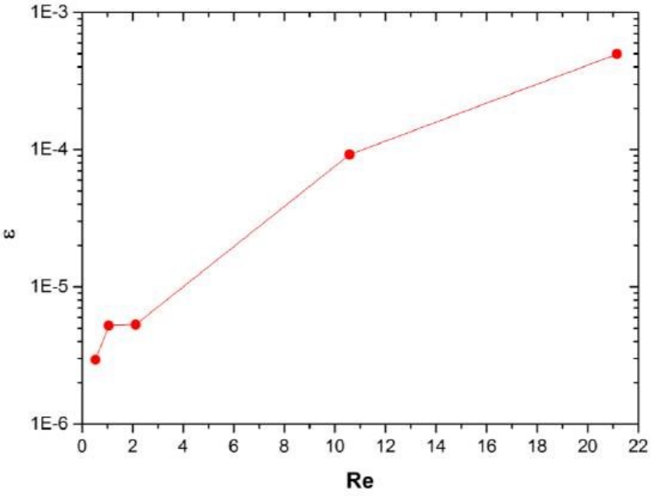

Figure 7.12. Residual error of the fitting of RTD experiments in a straight capillary with solutions of the ADM as a function of Re. Analytical solution of the ADM used: Eq. 7.7 for N_L<0.01; Eq. 7.8 for N_L>0.01. The fitting is based on the least squares method and is carried out using both equations and then, based on the value of the solutions, selecting the correct one.

7.4.3 Axial dispersion in straight capillary and helically coiled tubes

The adoption of the dispersion number Nd is convenient because it allows comparison of the extent of dispersion measured in pulsating flow or in HCT structure with that in straight tubes predicted by the Taylor-Aris equation for dispersion, Eq. 7.5. Written in terms of dispersion number, the equation becomes:

$$N_{d,TA} = \frac{1}{ReSc} + \frac{ReSc}{192} \qquad \text{Eq. 7.17}$$

The first term on the right-hand side of Eq. 7.17 can be neglected, because it is significant only for $Bo<100$ and in this work the Bodenstein number ranged between 10^4 and 10^5. Also, the Schmidt number is kept constant as deionized water and aqueous solutions of Basic Blue 3 are used as carrier fluid and tracer, respectively. The properties of the fluid are assumed to be those of water at room temperature ($\rho = 997\ \mathrm{kg/m^3}$, $\mu = 0.001\ \mathrm{Pas}$) and the diffusion coefficient of the tracer in water, measured experimentally in a straight capillary (see section 7.4.1) is $6.4{\cdot}10^{-10}\ \mathrm{m^2/s}$, leading to $Sc = 1677$. Eq. 7.17 can then be written as follows:

$$N_{d,TA} = (Sc/192)Re = 8.7Re \qquad \text{Eq. 7.18}$$

Eq. 7.18 expresses the relationship between dispersion and Reynolds numbers for straight pipes for our system. $N_{d,TA}$ is an increasing linear function of Re for any given value of Sc.

A constant flow rate $Q = 1\ \mathrm{mL/min}$ is used for the non-pulsating syringe pump for all the experiments conducted. A step-like pulsation is superimposed using the dedicated pulsating syringe pump. Two series of experiments are performed. In the first series we keep the Strouhal number constant while changing the amplitude ratio and vice versa in the second series. The values of N_d reported are averaged over three experiments for each set of parameters. The standard deviation is shown as error bars on the data points.

In the first series of experiments, we increase the amplitude ratio α by increasing the pulsating flow rate Q_{max}. Six different values of amplitude ratio are investigated, α=0, 0.5, 1, 3, 5, 9, that correspond respectively to $Q_{max} = 1$, 1.5, 2, 4, 6, 10 mL/min. To maintain the Strouhal number constant, the frequency f has to remain constant. To do so, a pulsation frequency is fixed and equal to 1 Hz. The results are presented in Figure 7.13 which shows the vessel dispersion number N_d of straight and HCT structures as function of the amplitude ratio α for a given Strouhal number $St = \frac{1\mathrm{Hz}\cdot 1\mathrm{mm}}{\left(1\frac{\mathrm{mL}}{\mathrm{min}}\right)/(\pi 0.5^2\mathrm{mm})} = 0.047$.

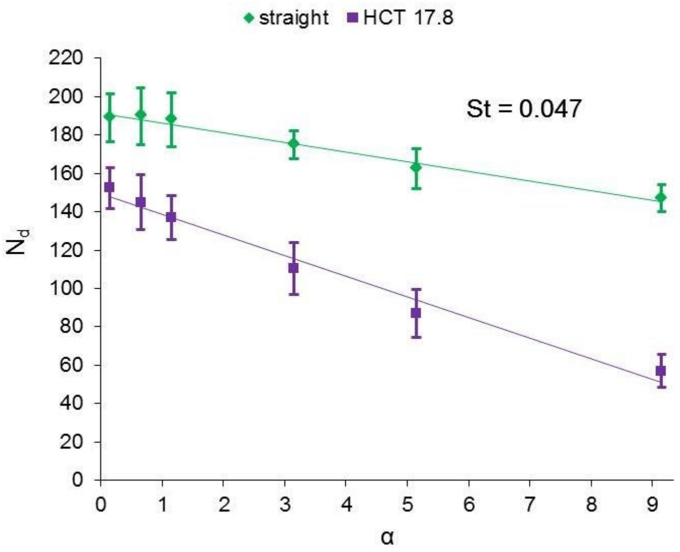

Figure 7.13. Vessel dispersion number as a function of amplitude ratio in helically coiled tube λ=17.8 and straight tube. Strouhal number = 0.047, capillary length = 5 m, capillary internal diameter = 1 mm, average flow rate = 1 mL/min.

The condition of $\alpha = 0$ corresponds to the amplitude ratio of zero and fully developed parabolic profile ($Re = 21.2$). This experiment provides the blank experimental condition and works as a reference for the other experiments in which the pulsation is applied. In this condition, the vessel dispersion number for the straight tube is $N_d = 180 - 200$ which is in the range of the theoretical value that can be calculated by Eq. 7.18 ($N_{d,TA} = 8.7 \cdot 21.2 = 184$). By increasing the pulsation amplitude α from 0 to 9, the vessel dispersion number N_d decreases down to $140 - 150$. The axial dispersion is therefore reduced due to pulsation. The same experiments repeated using the HCT device lead to a better performance. For any value of the amplitude ratio, the HCT shows less dispersion than straight tubes (from $N_d = 145 - 160$ to $N_d = 50 - 60$), confirming that also the secondary flow plays an important role in determining the dispersion behaviour. This is expected because the intensity of secondary flow, quantified by De, depends on the fluid velocity (Eq. 7.15) and by increasing the pulsation amplitude the local velocity of the fluid increases (Q_{max} increases). The Dean number increases with the amplitude ratio: from $De = 5$ when $\alpha = 0$ to $De = 55.2$ when $\alpha = 9$. To conclude, the axial dispersion can be improved combining the effects of pulsation and secondary flow obtained in HCT. At the highest amplitude ratio the vessel dispersion number is reduced by $70\ \%$ compared to the straight pulseless conditions.

In the second series of experiments, we increase the Strouhal number St by increasing the pulsation frequency f. Six different values of Strouhal number are investigated, $St = 0,\ 0.012,\ 0.016,\ 0.047,\ 0.094,\ 0.188$, that correspond respectively to $f = 0,\ 0.25,\ 0.333,\ 1,\ 2,\ 4\ \mathrm{s}^{-1}$. To maintain the amplitude ratio constant, the pulsating flow rate Q_{max} has to remain constant. To do so, a pulsating flow rate Q_{max} is fixed and equal to $10\ \mathrm{mL/min}$. This is the maximum flow rate adopted in the previous series of experiments which provides the maximum amplitude ratio and the lowest fluid dispersion. The results are presented in Figure 7.14 which shows the vessel dispersion number N_d of straight and HCT structures as function of the Strouhal number St for a given amplitude ratio $\alpha = \frac{(10-1)\mathrm{ml/min}}{1\mathrm{ml/min}} = 9$.

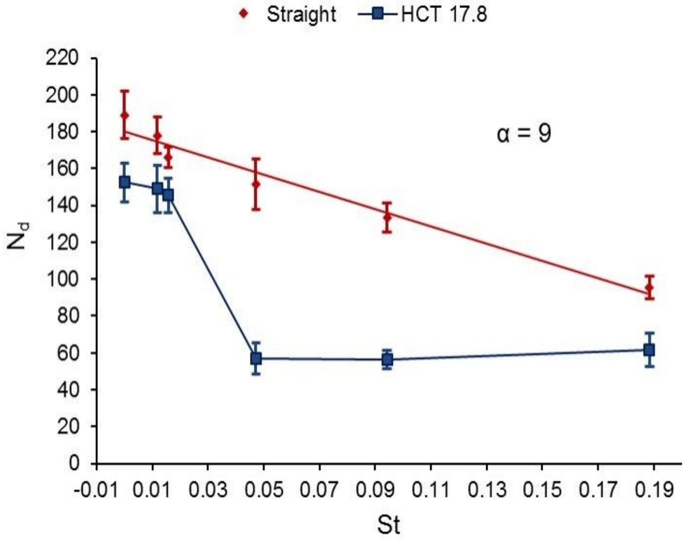

Figure 7.14. Vessel dispersion number as a function of Strouhal number in helically coiled tube λ=17.8 and straight tube. Amplitude ratio = 9, capillary length = 5 m, capillary internal diameter = 1 mm, average flow rate = 1 mL/min.

The condition $St = 0$ and $N_{d,TA} = 184$, provides again the same blank pulseless experimental condition for straight tube to be compared with the following pulsating conditions in which the pulsation frequency is changed ($St > 0$). By increasing the Strouhal number from 0 to 0.188, the vessel dispersion number N_d decreases down to $90 - 100$. This value is below the one obtained in the first series of experiment ($N_d = 140 - 150$) which was achieved using the same amplitude ratio $\alpha = 9$ but with a lower St. This result proves that fluid dispersion can be further improved by increasing the Strouhal number. In conclusion both parameters α and St play a role in the reduction of the vessel dispersion number in straight milli-channel geometries.

In the same way as we have done in the first series, the experiments are then repeated using the HCT structure. Also in this second series, the HCT shows less dispersion than straight tubes (in Figure 7.14 the N_d points are all positioned below the ones obtained using the straight channel). Here N_d decreases from $N_d = 145 - 160$ when $St = 0$ to $N_d = 50 - 60$ when $St = 0.047$ and then remains constant. Larger values of St do not lead to a further reduction of the axial dispersion and $N_d = 50 - 60$ represents the lowest axial dispersion achievable with the HCT system. The vessel dispersion number is reduced by $70\ \%$ compared to the straight pulseless conditions. Note that, now with the HCT only the increasing pulsation frequency contributes to the reduction of the axial dispersion. The Dean number remains constant ($De = 55.2$) as the local velocity of the fluid Q_{max} is fixed for all the experiments.

According to the literature in laminar regime, a Strouhal number of *O*(1) is particularly desirable to reduce axial dispersion in laminar flow[152,153]. It would be interesting to see whether the axial dispersion can be further improved by operating at larger values of either the amplitude ratio or of the Strouhal number than those reported in Figure 7.13 and Figure 7.14 respectively. Unfortunately, the pump is limited to a maximum flow rate of $10\ \mathrm{mL/min}$ and a frequency of $4\ \mathrm{s}^{-1}$. As a result, amplitude ratio and Strouhal numbers higher than 10 and 0.188 respectively cannot be investigated with the current setup.

A study in which fluid pulsation is applied to a helically coiled capillary structure has never been reported in the literature. The experimental results obtained here represents an explorative work that would need further investigation. However, some important information can be deduced from the present work: the pulsating platform designed is able to reduce fluid dispersion in small capillary tubes (both straight or helically coiled). The performance obtained is still quite distant from what can be achieved using oscillatory baffled tubes in which fluid dispersion is lowered by 10-15 times[144,145,146]. The latter systems incorporate anular baffles and staggered fins. These elements create eddies when liquid is pushed up through the tube. Eddy generation on both sides of the baffles creates very effective mixing while still maintaining plug flow. Our system is more simple and particularly suitable when dealing with particles. For this reason a comparison between the two systems based on the St and α values at which we obtain a significant reduction of fluid dispersion is not feasible. However, we reported for our conditions a certain threshold beyond which axial dispersion cannot be further improved for increasing St and α at given λ in HCT.

In Figure 7.15a and Figure 7.15b are reported two representative RTD data fittings. The data points in red refer to the experimental RTDs data, while the thin red and blue curves refer to the analytical solutions of the ADM (Eq. 7.7 or Eq. 7.8, respectively). Figure 7.15a shows the data fitting related to the straight capillary without pulsation while Figure 7.15b shows the data fitting related to the HCT device using the highest Strouhal and amplitude ratio ($\alpha = 9$, $St = 0.188$). In the former figure a good fitting ($\varepsilon = 4.45 \cdot 10^{-4}$) is achieved while in the latter a worse fitting and a larger residual error ($\varepsilon = 10^{-3}$) are obtained due to the pulsation applied (refer to section 7.4.4 for more details).

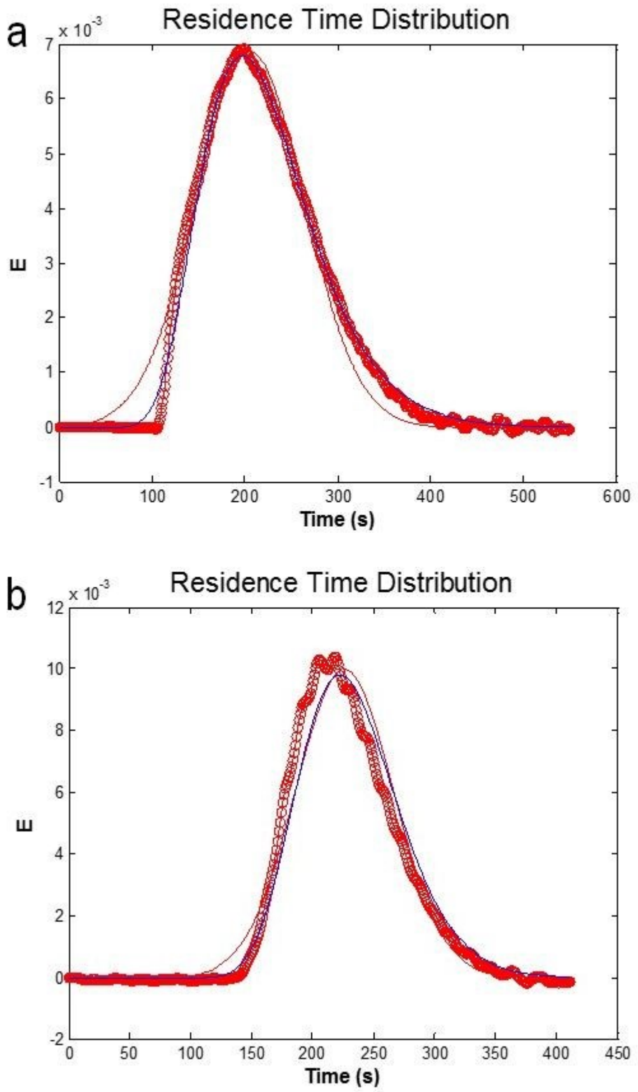

Figure 7.15. RTD data fitting (a) in straight capillary without pulsation (N_d = 180-200) and (b) in HCT with pulsation α = 9 and St = 0.188 (N_d = 50-60).

7.4.4 Applicability of the axial dispersion model in non-straight tubes and unsteady flow

In this section, we investigate the applicability of the axial dispersion model for unsteady pulsating flow in straight and HCT devices.

Figure 7.16 and Figure 7.17 show the residual error of the ADM curves used to fit the experimental results as a function of amplitude ratio and Strouhal number, respectively, for both straight and HCT structures. The criterion that we proposed to judge the applicability of the ADM requires that the residual error should be lower than $\varepsilon_{cr} = 10^{-3}$. We considered only experiments fulfilling this criterion, as Figure 7.16 and Figure 7.17 confirm.

Figure 7.16 shows that the residual error ε increases with the amplitude ratio α. At low amplitude ratio ($\alpha < 1$), the analytical solutions of the ADM (either Eq. 7.7 or Eq. 7.8) fit very well the experimental RTD curves giving small residual error (in the order of 10^{-4}). This error then becomes in the order of 10^{-3} for larger values of α. This result shows that as long as we are close to the conditions for which the ADM is formulated (low amplitude ratio), the error produced is small. This error increases at high amplitude ratio when approaching high pulsating fluid dynamic conditions. Here the deviation from pulseless flow becomes significant, and therefore the ADM is no longer fully valid and the residual error calculated applying the ADM is larger. The error generated with the straight capillary is generally smaller than the one obtained using the HCT structure as in the latter the deviation from pulseless flow is more dominant due to the occurrence of both flow pulsation and secondary flow.

A similar trend and considerations arise from Figure 7.17, which shows an increasing residual error ε with the increasing pulsation frequency f or St. Low values of pulsation frequency results in a good fitting of the ADM and a small residual error is therefore obtained. This error increases with the pulsation frequency as a result of the increased deviation from the pulseless flow. Both the straight and the HCT structures provide more or less the same residual error.

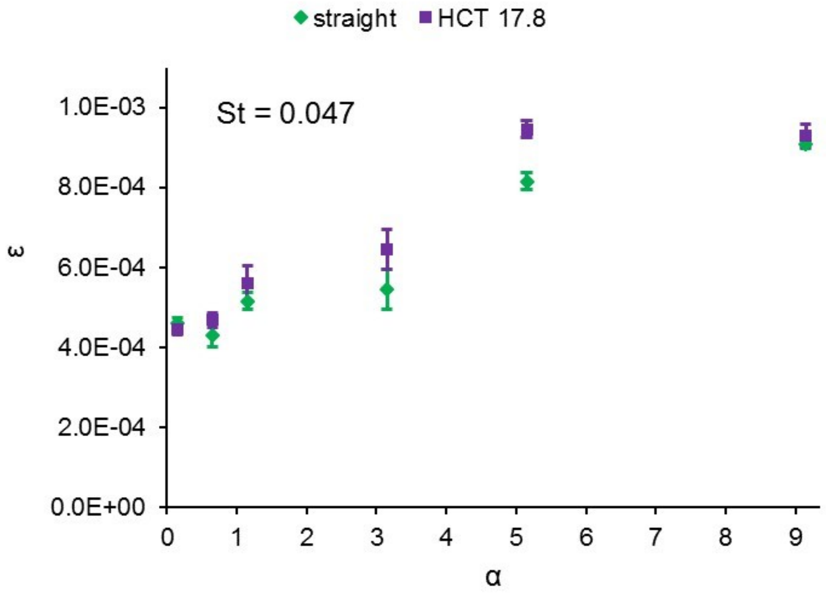

Figure 7.16. Residual error of the fitting of RTD experiments performed in helically coiled tube λ=17.8 and straight tube as a function of amplitude ratio. Strouhal number = 0.047, capillary length = 5 m, capillary internal diameter = 1 mm, average flow rate = 1 mL/min.

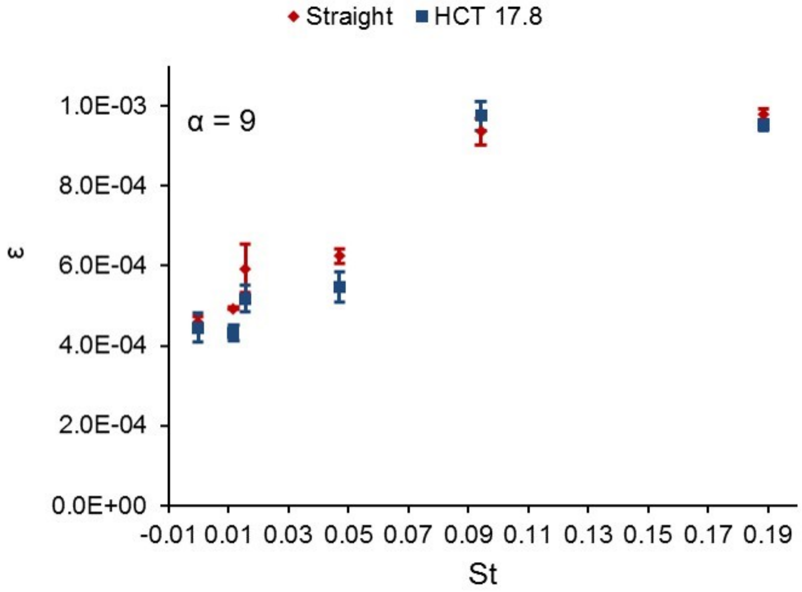

Figure 7.17. Residual error of the fitting of RTD experiments performed in helically coiled tube λ=17.8 and straight tube as a function of Strouhal number. Amplitude ratio = 9, capillary length = 5 m, capillary internal diameter = 1 mm, average flow rate = 1 mL/min.

7.5 Conclusions

Fluid flow is mostly laminar in microchannels due to their small hydraulic diameters. This causes a lack of uniformity in residence time and velocity distributions across the cross-section of the microchannel as a result of the parabolic velocity profile. Improving these distributions is very attractive for our purpose to obtain a uniform growth of crystalline structures.

It is believed that by inducing oscillatory flow the residence time distributions can be improved. Experiments are carried out to investigate the effects of step-like pulsation amplitude and Strouhal number on the RTD in microchannels and identify conditions under which the RTD is improved. Flow pulsation is applied in both straight and helically coiled tubes. The latter device is identified to be particularly suitable to improve radial mixing and reduced axial fluid dynamic dispersion. The Aris-Taylor axial dispersion model is used to quantify the axial dispersion coefficients.

A setup is designed to measure reliably RTDs in the helically coiled tube and, more in general, in different milli and microfluidic devices. Experiments in straight capillaries are also conducted to measure the molecular diffusion coefficient of the tracer in water and to generate a criterion for the applicability of the axial dispersion model in systems different than straight tubes and for unsteady pulsating flow. Results show that increasing pulsation amplitude and Strouhal number lead to a reduction of the axial dispersion. Moreover, lower values of axial dispersion are obtained in the helically coiled tube compared to the straight tube. Using the helically coiled tube, the vessel dispersion number can be reduced by $70\ \%$ compared to the straight pulseless conditions. Helically coiled tubes can be potentially employed with flow pulsation as high-performance and compact systems alternative to oscillatory baffled reactors to reduce axial dispersion in continuous processes involving, for instance, particle formation and particle growth.

8. Summary and general remarks

8.1 General conclusions

The major objective of this thesis was to advance knowledge into the development and design of a nucleation unit which constitutes the first part of a novel continuous microfluidic sonocrystallizer. Crystallization of adipic acid from supersaturated solution was the selected case of study. The device combines in a single compact unit three different technologies: continuous flow, small channel reactor technology and ultrasound engineering. Continuous flow guarantees a constant crystal production that would otherwise be impossible to obtain in milli-geometries using a batch approach. Small channel technology offers improved heat and mass transfer therefore achieving easily the desired supersaturation level for crystal nucleation. Ultrasound enhances nucleation rates, lowers the induction time also provides smaller crystals and narrower size distributions as compared to silent conditions.

In chapter 4 we introduced a novel capillary crystallizer that allows performing nucleation studies in different fluid dynamic conditions. The crystallizing solution was partitioned into small immiscible droplets and nucleation kinetics was determined using a stochastic approach by measuring the frequency of crystal appearance in stagnant (montionless droplets) and flow (moving droplets) conditions. The results showed that that nucleation of adipic acid solution occurs mainly via a heterogeneous mechanism in both cases. The mixing patterns achieved inside the moving droplets accelerate the nucleation rates by about 30 % increasing the kinetics of the process without changing the nucleation energy barrier (which is not related to flow). The change in the kinetics of nucleation was explained with the enhancement of the attachment frequency by the increase of the flux of monomers towards the nucleus surface by convection. The developed microfluidic system offered the opportunity to investigate the nucleation phenomenon in silent regime and appreciate the effect of flow and mixing on nucleation rate.

In chapter 5 the droplet-based flow system was modified to be coupled with an ultrasound source for the continuous production of crystals. The system represents a powerful nucleation unit which is able to provide crystals with a very small mean size at very high nucleation rates. The effect of supersaturation and ultrasound power on nucleation was investigated and a sharp threshold of immediate crystal generation (sonocrystallization) was identified. Sonochemiluminesence and sonoemulsification experiments as well as numerical simulations were employed to map the cavitation zones within the capillary crystallizer. A direct link between the cavitation areas and the crystal appearance was observed and it was concluded that transient cavitation of bubbles is a significant mechanism for enhancing nucleation of crystals among several proposed in the literature. Furthermore, a stochastic analysis of crystal primary nucleation under the presence of ultrasound was performed to calculate the adipic acid nucleation kinetics. Results showed a step-like trend in the cumulative probability function which leads to nucleation rates of at least four orders of magnitude higher than the corresponding silent ones.

In chapter 6 we introduced an alternative nucleation unit which only uses single-phase flow to produce fine crystals in a reproducible way. Channel occlusion was avoided employing large capillary diameters. By changing the flow rates we could regulate the time during which the crystallizing solution experiences ultrasound and therefore control the desired crystal mean size. Moreover, crystal production was found to increase linearly with supersaturation while crystal production increases by decreasing the capillary size. Crystal breakage and crystal agglomeration are not playing a dominant role under the experimental conditions and therefore the resulting CSDs, crystal shape and crystal production are the result of only nucleation and growth processes that are the two main mechanisms that govern the sonocrystallization in the single phase crystallizer.

In chapter 7 we performed a preliminary work towards the development and design of the growth stage. To this end, we used flow pulsation as a potential method to flatten the velocity profile and narrow the RTD. Helically coiled tube structures are identified as a promising solution to further improve fluid dynamic axial dispersion in a single compact unit where long residence times are desired. In recent years, particle formation and particle growth, traditionally conducted in batch reactors, have been performed in continuous milli and microfluidic systems in an effort to achieve improved controllability, specifically on the particle size distribution of the product. The experimental work conducted in this last chapter provides additional evidence that helically coiled tubes are promising solutions for such operations.

8.2 Areas of future research

Although some important achievements in the development and design of the nucleation unit, there are several challenges that still need to be addressed:

1. The continuous droplet-based system represents the first nucleation unit designed which is particularly suitable to be used is small capillaries (ID < 1.55 mm). The system offers good performance in terms of small mean crystal size and high nucleation rate without channel fouling. However, as the nuclei are produced within droplets flowing in hexane carrier fluid, an additional separation process is required at the end of the crystallization process (ideally after the growth or disruption stage) to recover crystals. The presence of the carrier fluid (hexane) represents a potential source of contamination for the crystalline compound and an additional cost for the process. Alternative methods of aqueous solution-hexane separation such as spatially selective surface modification could be implemented in the system before the final filtration[162].
2. The continuous single-phase system overcomes the limitation of the droplet-based system as the carrier fluid is no longer present. However, the system does not allow to produce nuclei in narrow capillary geometry. Particularly large capillary diameters are required to avoid clogging (ID ≥ 1.55 mm). However, these dimensions are found to be particularly suitable and easy to implement with the following growth stage where large diameters are desired to achieve crystal growth.

Although the design of the growth stage is still a problem under investigation and not a specific subject of the current thesis, if the pulsating flow approach was selected as the best method to flatten the velocity profiles and achieve uniform growth, then the problem of connecting a steady continuous nucleation stage with a pulsating unsteady growth stage would pose the technical problem of promoting the fluid oscillation in between the two stages. In this regard, fluid pulsation could be obtained by a piston-driven diaphragm fixed after the nucleation unit. These mechanisms are normally employed in the oscillating baffle reactors to control RTDs with very low axial dispersion[144,145,146,147].

3. The ultrasonic probe is the device used in this work as a source of ultrasonic power. The probe is aligned orthogonally to the capillary crystallizer external wall and the distance between the two elements can be controlled using an adjustable stage holder. This system is an easy method to set the relative distance between the capillary and the probe but it is not very accurate due to the not very precise manual control. To better monitor the vertical and lateral distance between the two elements an XYZ electronic stage would be more suitable. As a result the experimental error would be smaller with better data reproducibility.
4. Ultrasound is the main technology which is used in this work to enhance the nucleation performance. Although the sonoprobe is a simple device to be implemented and aligned with the capillary sonocrystallizer, the system does not offer a good flexibility in terms of frequency variation. The sonoprobe is too big and heavy and the ultrasonic power employed too high and not properly focused on the capillary volume. This ultrasonic energy is therefore dissipated into heat and transferred to the cooling water contained inside the nucleation enclosure where the same capillary is aligned. A design of a more compact and efficient unit would be an attractive solution to miniaturize the entire nucleation stage. The unit might consist of a channel where one side is attached

to a piezoelectric material that acts as an ultrasonic generator, while the other side will be coupled to a heat removal surface (*e.g.* a flat Peltier cooler). A potential realization of the unit would be a layered arrangement of glass plates with etched channels. The channel for nucleation would be contained in a sort of “sandwich” between the heat-exchange channel and the ultrasonic source[19]. This configuration is also ideal for numbering up strategies of microfluidic units. The use of piezoelectric actuators is energetically favoured and allows the connection of multiple units with a single power generator and amplifier.

Appendix

This section contains MATLAB scripts used for post-processing of step input experiments with UV-VIS spectroscopy.

Fcurve.m

```
%% Main m-file to read *.csv files exported by
Spectrasuite and write F
%% curve to new MatLab matrix file. It works in the
general case of multiple
%% injections
clear all
%% Variable input
%
% Filename used to create .csv file
filename = ['exp1'];
% Name of folder where .csv files are located. (
foldername_read = ['Data'];
% Name of subfolder where to write the data matrix
created in the working
% directory. The name may refer to the parameter
investigated (e.g. flow
% rate). In this folder a subfolder must be created named
as 'filename' %
foldername_write = ['1mLmin'];
% Injection times/end: insert below the sequence of
elapsed times from
% starting of acquisition after each single injection as
well as the final
% elapsed time
inj_time = [10.0 100.0];
%
%% Import files recalling ImportFile.m
%
[time,Abs] = ImportFile([foldername_read '\' filename
'.csv']);
%
%% Separate data of multiple injection
%
N_inj = length(inj_time)-1;
%
for i=1:length(inj_time)-1
i_start(i) = find(time >= inj_time(i),1,'first');
i_end(i) = find(time <= inj_time(i+1),1,'last');
end
%
```

```
%% For loop to write to new matrix Abs_data
%
POS=0; NEG=0;
for i=1:N_inj
%
if ceil(i/2)-i/2 > 0
%%Write to variable positive steps
% First column: time
% Second column: absorbance
% Third column: normailized absorbance (F curve)
Abs_data(:,1) = time(i_start(i):i_end(i))-
time(i_start(i));
Abs_data(:,2) = Abs(i_start(i):i_end(i));

Abs_data(:,3) = (Abs_data(:,2)-
min(Abs_data(:,2)))/max(Abs_data(:,2));
% Save Abs_data matrix to folder with the same filename
created in
% the working directory
POS = POS+1;
save([foldername_write '\' filename '\' 'Abs_data_POS_'
num2str(POS)],'Abs_data','inj_time')
clear Abs_data
else
%%Write to variable negative steps
% First column: time
% Second column: absorbance
% Third column: normailized absorbance (W curve)
% Fourth column: F = 1-W
Abs_data(:,1) = time(i_start(i):i_end(i))-
time(i_start(i));
Abs_data(:,2) = Abs(i_start(i):i_end(i));
Abs_data(:,3) = (Abs_data(:,2))/max(Abs_data(:,2));
Abs_data(:,4) = 1-Abs_data(:,3);
% Save Abs_data matrix to folder with the same filename
created in
% the working directory
NEG = NEG + 1;
save([foldername_write '\' filename '\' 'Abs_data_NEG_'
num2str(NEG)],'Abs_data','inj_time')
clear Abs_data
end
end
%%%%%%%%%%%%%%%%%%%%%%%%%%%%%%%%%%%%%%%%%%%%%%%%%%%%%%%%%%%
```

Ecurve.m

```
%% Main m-file to anlyse RTD experimental data from F curve
clear all
%% Variable input
% Name of the folder where Fcurve_POS1.m is located
folder_name = '1mLmin';
% Original name of the .csv file
file_name = 'Exp1_POS_1';
% Input 1 for positive injectios. Input 0 for negative injections
POS = 1;
% Span: number of data points for smoothing
span = 20;
%% Open Fcurve_POS1.m
load([folder_name '\' file_name '\Fcurve_' file_name],'Abs_data')
%
%% Allocate imported array to column variable names
Time = Abs_data(:,1);
if POS==1
Abs = Abs_data(:,3);
else
Abs = Abs_data(:,4);
end
%
%% Smooth F curve
%
Abs_smooth = smooth(Time,Abs,span);
n = ceil(length(Abs_data(:,1))/2000);
Time = downsample(Time,n);
dt=diff(Time);
Abs_smooth = downsample(Abs_smooth,n);
%
%% Differentiate the concentration and normalize
%
dAbs = diff(Abs_smooth)./dt;

dTime = Time(1:end-1)+dt./2;

E_t = dAbs_/sum(dAbs.*dt);
% Normalization accounting for drifting of signal
slope=(mean(E_t(end-50:end))-mean(E_t(1:50)))/dTime(end);
E_t = E_t - slope.*dTime;
%
%% Plot E_t
%
disp_name= file_name;
```

```
plot_name = 'Residence Time Distribution';
x_label = 'Time (s)';
y_label='E';
%
CreateFigure(dTime,E_t,plot_name,x_label,y_label,folder_n
ame,disp_name)
clearvars plot_name x_label y_label disp_name
%
%% Calculations:mean residence time and variance
% Calculate mean residence time
t_mean= trapz(dTime,E_t.*dTime)
% Calculate variance
sigma = trapz(dTime,E_t.*(dTime-t_mean).^2)
%
%% Calculation of RTD in dimensionless domain
%
theta = dTime/t_mean;
E_theta = E_t*t_mean;
%
%% Write to RTD data and save
% RTD_data
% First column: time (s)
RTD_data(:,1) = dTime;
% Second column: E_t (1/s)
RTD_data(:,2) = E_t;
% Third column: theta (dimensionless)
RTD_data(:,3) = theta;
% Fourth column: E_theta (dimensionless)
RTD_data(:,4) = E_theta;
%
save([folder_name '\RTD_data_'
file_name],'RTD_data','F_data','t_mean','sigma')

%%%%%%%%%%%%%%%%%%%%%%%%%%%%%%%%%%%%%%%%%%%%%%%%%%%%%%%%%%%
```

ADMfitting.m

```
%% This is the main m-file to perform fitting of RTD data
with ADM
%
clear all
%% Variable input
%
% Name of the folder where Ecurve_POS1.m is located
folder_name = 'mLmin';
% Original name of the .csv file
file_name = 'run1';
% Flowrate used for experiment
flowrate = 1;
% Internal diameter of tubular vessel [mm]
d_t = 1;
% Length of tubular vessel investigated [m]
L = 5;
% Molecular diffusivity of tracer in carrier fluid
Dm = 6.4E-10; %[m2/s]
%
%% Import data and preliminary calculations
load([folder_name '\' file_name '\RTD_data_' file_name])
time = RTD_data(:,1); Et_exp = RTD_data(:,2);
% Calculate mean internal velocity
d_t = d_t*10^-3; A = pi*d_t^2/4;
flowrate = flowrate*10^(-6)/60;
u = flowrate/A;
% Calculate axial dispersion coefficient with Taylor-Aris
eq. as first
% value for fitting
Dax_0 = u^2*d_t^2/(192*Dm);
% Estimate vessel dispersion number
Nl_0 = Dax_0 / (u*L)
%
%% Calculate Dax through least square fitting
%
%% RTD curve - t domain - small deviation - N_d < 0.01
open open
options = optimset('TolFun',1e-12,'TolX',1e-
12,'Diagnostics','on','Display','iter');
% Function handling
fun_sd = @(Dax_sd_fit,time)
sqrt(u.^3./(4*pi*Dax_sd_fit*L))*exp(-(L-
u*time).^2./(4*Dax_sd_fit*L./u));
% Dax fitting
[Dax_sd,RESNORM_sd,RESIDUAL_sd,exitflag_sd] =
lsqcurvefit(fun_sd,Dax_0,time,Et_exp,0,Inf,options);
% Vessel dispersion number
```

```
NL_sd = Dax_sd/(L*u);
% Dispersion number
Nd_sd = Dax_sd/(d_t*u);
% Re-calculate curve and plot
Et_ADMsd = sqrt(u.^3./(4*pi*Dax_sd*L))*exp(-(L-
u*time).^2./(4*Dax_sd*L./u));
plot4 = plot(time,Et_ADMsd,'r');
set(plot4(1),'DisplayName','Small deviations - fitted');
% RTD curve - t domain - large deviation - N_d > 0.01
open open
options = optimset('TolFun',1e-12,'TolX',1e-
12,'Diagnostics','on','Display','iter');
% Function handling
fun_ld = @(Dax_ld_fit,time)
u./sqrt((4*pi*Dax_ld_fit*time)).*exp(-(L-
u*time).^2./(4*Dax_ld_fit*time));
%
[Dax_ld,RESNORM_ld,RESIDUAL_ld,exitflag_ld] =
lsqcurvefit(fun_ld,Dax_0,time,Et_exp,0,Inf,options); %
% Vessel dispersion number
NL_ld = Dax_ld/(L*u);
% Dispersion number
Nd_ld = Dax_ld/(d_t*u);
% Re-calculate curve and plot
Et_ADMld_oo = u./sqrt((4*pi*Dax_ld*time)).*exp(-(L-
u*time).^2./(4*Dax_ld*time));
plot5 = plot(time,Et_ADMld_oo,'b');
set(plot5(1),'DisplayName','Large deviations - fitted');
%
Re=997*u*d_t/0.001;
%% Save data
%
save([folder_name '\RTD_fitted_ADM_' file_name])
%%%%%%%%%%%%%%%%%%%%%%%%%%%%%%%%%%%%%%%%%%%%%%%%%%%%%%%%%%
```

ImportFile.m

```
%% Auxiliary function to import absorbance-time data from
.csv files
function [Time,Abs] = importfile(filename, startRow,
endRow)
%IMPORTFILE Import numeric data from a text file as
column vectors.
% [ELAPSEDTIME,ABSORBANCEABSORBANCE] =
IMPORTFILE(FILENAME) Reads
% data from text file FILENAME for the default selection.

[ELAPSEDTIME,ABSORBANCEABSORBANCE] = IMPORTFILE(FILENAME,
% STARTROW,ENDROW) Reads data from rows STARTROW through
ENDROW of
% text file FILENAME.
%
% Example:
% [ElapsedTime,AbsorbanceAbsorbance] =
% importfile('L500cm_005mlmin_BB.csv',6, 8280);
%
% See also TEXTSCAN.
%% Initialize variables.
delimiter = '\t';
if nargin<=2
startRow = 6;
endRow = inf;
end
%% Format string for each line of text:
% column2: double (%f)
% column3: double (%f)
% For more information, see the TEXTSCAN documentation.
formatSpec = '%*s%f%f%[^\n\r]';
%% Open the text file.
fileID = fopen(filename,'r');
%% Read columns of data according to format string.
% This call is based on the structure of the file used to
generate
% this code. If an error occurs for a different file, try
% regenerating the code from the Import Tool.
dataArray = textscan(fileID, formatSpec, endRow(1)-
startRow(1)+1, 'Delimiter', delimiter, 'EmptyValue'
,NaN,'HeaderLines', startRow(1)-1, 'ReturnOnError',
false);
for block=2:length(startRow)
frewind(fileID);
dataArrayBlock = textscan(fileID, formatSpec,
endRow(block)-startRow(block)+1, 'Delimiter', delimiter,
```

```
'EmptyValue' ,NaN,'HeaderLines', startRow(block)-1,
'ReturnOnError', false);
for col=1:length(dataArray)
dataArray{col} = [dataArray{col};dataArrayBlock{col}];
end
end
%% Close the text file.
fclose(fileID);
%% Allocate imported array to column variable names
Time = dataArray{:, 1};
Abs = dataArray{:, 2};
%%%%%%%%%%%%%%%%%%%%%%%%%%%%%%%%%%%%%%%%%%%%%%%%%%%%%%%%%%%
```

CreateFigure.m

```
%% Auxiliary function to plot data
function CreateFigure(X_1,Y_1,
plot_name,x_label,y_label,filename,disp_name)
%CREATEFIGURE(X1,YMATRIX1)
% X1: vector of x data
% YMATRIX1: matrix of y data
% Create figure
figure1 = figure('Name',[plot_name ' - '
filename],'NumberTitle','off');
% Create axes
axes1 = axes('Parent',figure1,...
'Position',[0.101850809289233 0.11 0.775 0.815]);

box(axes1,'on');
hold(axes1,'all');
% Create multiple lines using matrix input to plot
plot1 = plot(X_1, Y_1,'Marker','o');
set(plot1(1),'Color',[1 0 0],'DisplayName',disp_name);
% Create xlabel
xlabel(x_label,'FontWeight','bold','FontSize',12,'FontNam
e','Arial');
% Create ylabel
ylabel(y_label,'FontWeight','bold','FontSize',12,...
'FontName','Arial');
% Create title
title(plot_name,'FontSize',16,'FontName','Arial');
%%%%%%%%%%%%%%%%%%%%%%%%%%%%%%%%%%%%%%%%%%%%%%%%%%%%%%%%%%%
```

Example of data fitting for the determination of axial dispersion in straight capillary

Capillary length 5 m

Average flow rate 1 mL/min

Capillary internal diameter 1 mm

No Pulsation applied

RTD derived from the Ecurve.m script without smoothing

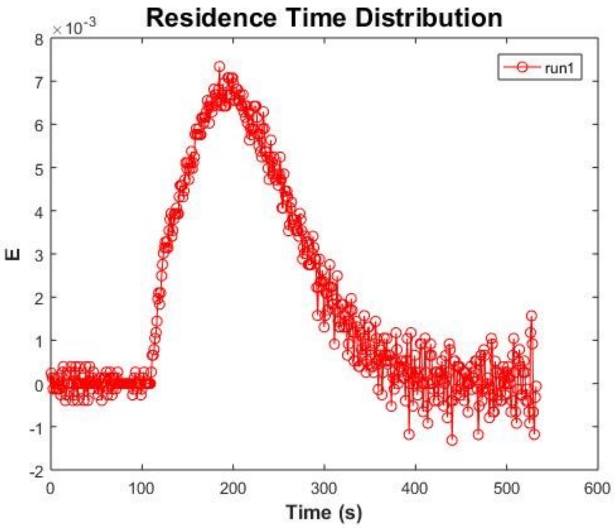

RTD derived from the Ecurve.m script with span = 20

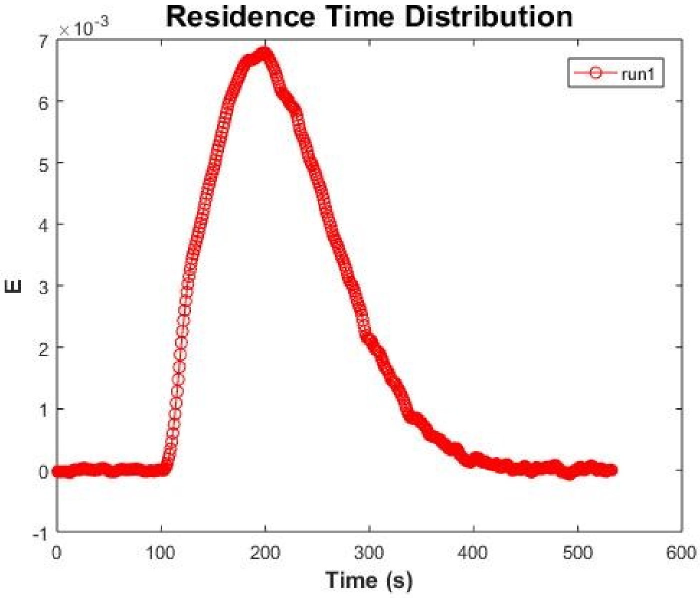

RTD fittings derived from the ADMfitting.m script

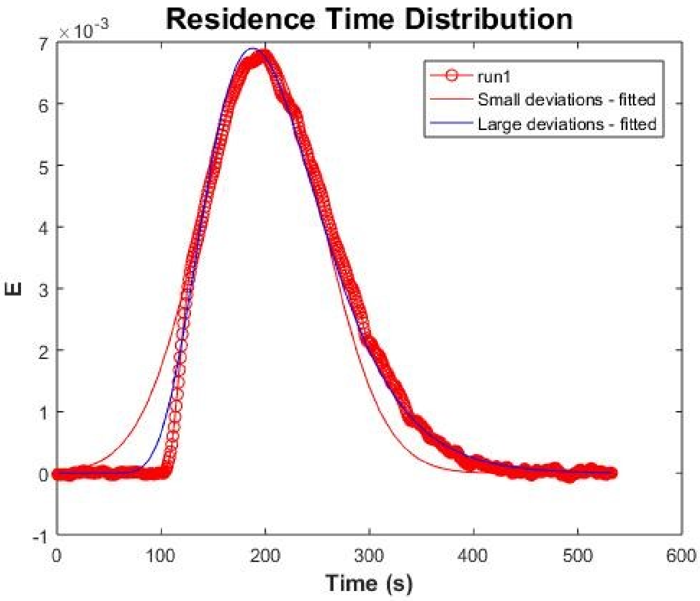

Nd_ld = 197.2, RESNORM_ld = 4.45-04 (Nl_ld = 0.048)

Nd_sd = 185.3, RESNORM_sd = 4.71e-04 (Nl_sd = 0.04)

Both fittings provide a residual error which is below the threshold ε_{cr} = 1e-03. However, we considered the vessel dispersion number Nd_ld as the fitting is carried out using the correct solution valid for large deviation (0.048 > 0.01).

Notation

Latin letters

a	Actual activity of molecules in solution
a_e	Equilibrium activity of molecules in solution
A or A'	Kinetics pre-exponential factor / Absorbance
A_C	Growing crystal face
A_{HEN}	Kinetics pre-exponential factor of HEN
A_{HON}	Kinetics pre-exponential factor of HON
A_C	Cluster-solution interface
A^*	Critical nucleus-solution interface
A_{tip}	Area of the sonoprobe tip
B	Thermodynamics exponential factor
Bo	Bodenstein number
B_{HEN}	Thermodynamics exponential factor of HEN
B_{HON}	Thermodynamics exponential factor of HON
c	Crystal shape factor
c_p	Water heat capacity
C	Actual concentration of molecules in solution / Tracer concentration
C_e or C^*	Equilibrium concentration of molecules in solution
Ca	Capillary number
C_i	Solute concentration in the solution at the crystal-solution interface
C_0	Concentration of active nucleation sites in solution

C^*	Equilibrium concentration of cluster in solution
d_0	Molecule diameter
d	Crystal/Particle diameter
d^*	Crystal diameter at detectable size
d_t	Pipe internal diameter
d_e	Pipe external diameter
De	Dean number
D	Monomer diffusion coefficient
D_{ax}	Axial dispersion coefficient
D_m	Molecular diffusion coefficient
D_s	Diameter of the HCT cylindrical support
E	Residence time distribution function
F	Cumulative distribution function
f	Attachment frequency / Flow pulsation frequency / Ultrasound frequency
f_0	Resonance frequency
f^*	Attachment frequency at equilibrium concentration of cluster in solution
g	Detachment frequency
g_i	Order of the overall crystal growth process
G	Growth rate
h	Microchannel height
h_w	Wetting film thickness
I	Intensity of the light detected
I_0	Intensity of the light emitted

j^*	Diffusion flux of monomers
J	Primary nucleation rate
J_d	Homogeneous primary nucleation rate controlled by diffusion
J_t	Homogeneous primary nucleation rate controlled by interface transfer
J_{HEN}	Heterogeneous primary nucleation rate
J_{HON}	Homogeneous primary nucleation rate
k_d	Coefficient of mass transfer by diffusion
k_r	Reaction rate constant for the surface integration process
K	Boltzmann constant
K_G	Overall crystal growth coefficient
l	Path length of the beam of light through the material sample
L	Length
m	Mass
M	Overall number of droplets
M^+	Number of droplets with at least one crystal
M_W	Molecular weight of the crystal
n	*n*-sized cluster
n_c	Number of crystals
n^*	Critical nucleus size
N	Expected average number of crystals
N^*	Average number of particles that can pass through a fabricated microchannel before clogging
N_a	Nucleation-active centers
N_A	Avogadro number

N_L or N_d	Vessel dispersion number
P_a	Pressure amplitude at the tip of the sonoprobe
P_0	Ambient pressure
P_E	Experimental probability function
Pe_L	Peclet Number
P_T	Theoretical probability function
P_{US}	Power transferred to the liquid
Q	Flow rate
Q_{max}	Maximum flow rate
r_i	Order integration reaction within the boundary reaction layer
R	Droplet radius
R^*	Radius of critical nucleus
R_0	Bubble radius
R_c	Channel radius
$R_{c,in}$	Inlet channel radius of dispersed phase
Re	Reynolds number
s	Slip velocity
S	Supersaturation
S^*	Supersaturation in the growth stage
Sc	Schmidt number
St	Stokes number
t	Time
t^*	Clogging time
t_{d^*}	Growth time

T	Temperature / Pulsation period
$\bar{v}$ or u	Average fluid velocity
u_{max}	Maximum fluid velocity
v_D	Velocity of the droplet
v_L	Fluid velocity
v_0	Molecular volume of the solid crystal
v_{sound}	Speed of sound
V	Volume
V_{Plug}	Plug velocity
V_p	Particle volume
V_m	Crystal volume at detectable size
w	Microchannel characteristic cross-section
w_c	Microchannel constriction width
W	Work associated cluster formation
W_S	Free energy loss due to the creation of an interface associated with cluster formation
W_V	Free energy gain related to the cluster volume associated with cluster formation
X_V	Volume distribution percentage
z	Zeldovich factor / Axial coordinate

Greek letters

α	Volume shape factor / Amplitude ratio
α_V	Crystal volume at detectable size and parent phase volume ratio
β	Surface shape factor
γ	Specific crystal-liquid surface energy
γ_p	Interfacial tension between two fluid phases
γ_{CS}	Specific crystal-substrate surface energy
γ_{SL}	Specific substrate-liquid surface energy
γ_L	Surface tension of the liquid
γ_{CL} or γ_{ef}	Effective specific crystal-liquid surface energy
ε	Particle-wall sticking distance / residual error
ε_{cr}	Critical residual error
ε_w	Holdup of water droplet
θ	Contact angle
λ	Coil-to-tube diameter ratio
μ_S	Chemical potentials of a molecule in the solution
μ_C	Chemical potentials of a molecule in the bulk of solid crystal phase
μ_{cp}	Viscosity of the continuous phase
μ_L	Viscosity of the fluid
ρ	Density of the crystal
ρ_L	Density of the liquid
ρ_D	Density of the particle
τ	Induction time

τ_{US}	Sonicated residence time
κ	Polytropic index
τ_{mean}	Mean time of formation of the first nucleus
τ_n	Time required to reach nuclei of critical size
τ_g	Time needed for nuclei to grow till a detectable size
χ	Particle volume fraction
φ	Extinction coefficient
ψ	Volmer factor
ω	Ratio of the particle sticking distance
ω_{OUT}	Mother liquor adipic acid concentration

Bibliography

1. Mullin, J. W. *Crystallization*. (Butterworth-Heinemann, Oxford, 2001).
2. Shekunov, B. Y. & York, P. Crystallization processes in pharmaceutical technology and drug delivery design. *J. Cryst. Growth* **211,** 122–136 (2000).
3. Variankaval, N., Cote, A. S. & Doherty, M. F. From Form to Function: Crystallization of Active Pharmaceutical Ingredients. *AIChE J.* **54,** 1682–1688 (2008).
4. Chen, J., Sarma, B., Evans, J. M. B. & Myerson, A. S. Pharmaceutical Crystallization Published as part of the Crystal Growth & Design 10th Anniversary Perspective. *Cryst. Growth Des.* **11,** 887–895 (2011).
5. Jones, A. G. *Crystallization Process Systems*. (Butterworth-Heinemann, London, 2002).
6. Ruecroft, G., Hipkiss, D. & Ly, T. Sonocrystallization: the use of ultrasound for improved industrial crystallization. *Org. Process Res. Dev.* **9,** 923–932 (2005).
7. McCausland, L. J., Cains, P. W. & Martin, P. D. Use the power of sonocrystallization for improved properties. *Chem. Eng. Prog.* **97,** 56 (2011).
8. Luque de Castro, M. D. & Priego-Capote, F. Ultrasound-assisted crystallization (sonocrystallization). *Ultrason. Sonochem.* **14,** 717–724 (2007).
9. Wohlgemuth, K., Ruether, F. & Schembecker, G. Sonocrystallization and crystallization with gassing of adipic acid. *Chem. Eng. Sci.* **65,** 1016–1027 (2010).
10. Guo, Z., Jones, a. G. & Li, N. The effect of ultrasound on the homogeneous nucleation of during reactive crystallization. *Chem. Eng. Sci.* **61,** 1617–1626 (2006).
11. Lyczko, N., Espitalier, F., Louisnard, O. & Schwartzentruber, J. Effect of ultrasound on the induction time and the metastable zone widths of potassium sulphate. *Chem. Eng. J.* **86,** 233–241 (2002).
12. Miyasaka, E., Kato, Y., Hagisawa, M. & Hirasawa, I. Effect of ultrasonic irradiation on the number of acetylsalicylic acid crystals produced under the supersaturated condition and the ability of controlling the final crystal size via primary nucleation. *J. Cryst. Growth.* **289,** 324–330 (2006).
13. Miyasaka, E., Ebihara, S. & Hirasawa, I. Investigation of primary nucleation phenomena of acetylsalicylic acid crystals induced by ultrasonic irradiation-ultrasonic energy needed to activate primary nucleation. *J. Cryst. Growth* **295,** 97–101 (2006).
14. Kordylla, A., Koch, S., Tumakaka, F. & Schembecker, G. Towards an optimized crystallization with ultrasound: Effect of solvent properties and

ultrasonic process parameters. *J. Cryst. Growth.* **310,** 4177–4184 (2008).

15. Llinàs, A. & Goodman, J. M. Polymorph control: past, present and future. *Drug Discov. Today* **13,** 198–210 (2008).
16. Narducci, O., Jones, a. G. & Kougoulos, E. Crystal Product Engineering in the Seeded Cooling Crystallization of Adipic Acid from Aqueous Solution. *Org. Process Res. Dev.* **15,** 974–980 (2011).
17. Narducci, O. & Jones, A. G. Seeding in Situ the Cooling Crystallization of Adipic Acid using Ultrasound. *Cryst. Growth Des.* **12,** 1727–1735 (2012).
18. Jiang, M. *et al.* Indirect Ultrasonication in Continuous Slug-Flow Crystallization. *Cryst. Growth Des.* **15,** 2486–2492 (2015).
19. Kuhn, S., Noël, T., Gu, L., Heider, P. L. & Jensen, K. F. A Teflon microreactor with integrated piezoelectric actuator to handle solid forming reactions. *Lab Chip* **11,** 2488–92 (2011).
20. Flowers, B. S. & Hartman, R. L. Particle Handling Techniques in Microchemical Processes. *Challenges* **3,** 194–211 (2012).
21. Mason, T. J. Ultrasound in synthetic organic chemistry. *Chem. Soc. Rev.* **26,** 443–451 (1997).
22. Cains, P. W., Martin, P. D. & Price, C. J. ReViews The Use of Ultrasound in Industrial Chemical Synthesis and Crystallization . 1 . Applications to Synthetic Chemistry Abstract : *Org. Process Res. Dev.* **2,** 34–38 (1998).
23. Hem, S. L. The effect of ultrasonic vibrations on crystallization processes. *Ultrasonics.* **5,** 202–207 (1967).
24. Virone, C., Kramer, H. J. M., van Rosmalen, G. M., Stoop, A. H. & Bakker, T. W. Primary nucleation induced by ultrasonic cavitation. *J. Cryst. Growth.* **294,** 9–15 (2006).
25. Cogné, C. *et al.* Theoretical model of ice nucleation induced by acoustic cavitation. Part 1: Pressure and temperature profiles around a single bubble. *Ultrason. Sonochem.* **29,** 447–454 (2016).
26. Cogné, C. *et al.* Theoretical model of ice nucleation induced by inertial acoustic cavitation. Part 2: Number of ice nuclei generated by a single bubble. *Ultrason. Sonochem.* **28,** 185–191 (2016).
27. Gavriilidis, A., Angeli, P., Cao, E., Yeong, K. K. & Wan, Y. S. S. Technology and applications of microengineered reactors. *Inst. Chem. Eng.* **80,** 3–30 (2002).
28. Jensen, K. F. Microreaction engineering - is small better? *Chem. Eng. Sci.* **56,** 293–303 (2001).
29. Leng, J. & Salmon, J. B. Microfluidic crystallization. *Lab Chip* **9,** 24–34 (2009).
30. Gerdts, C. J. *et al.* Time-controlled microfluidic seeding in nL-volume droplets to separate nucleation and growth stages of protein

crystallization. *Angew. Chemie - Int. Ed.* **45,** 8156–8160 (2006).

31. Elvira, K. S., Casadevall i Solvas, X., Wootton, R. C. R. & de Mello, A. J. The past, present and potential for microfluidic reactor technology in chemical synthesis. *Nat. Chem.* **5,** 905–15 (2013).
32. Marre, S. & Jensen, K. F. Synthesis of micro and nanostructures in microfluidic systems. *Chem. Soc. Rev.* **39,** 1183–1202 (2010).
33. Narducci, O., Jones, a. G. & Kougoulos, E. Continuous crystallization of adipic acid with ultrasound. *Chem. Eng. Sci.* **66,** 1069–1076 (2011).
34. Musser, M. T. Adipic Acid. *Ullmann's Encyclopedia of Industrial Chemistry* (2005).
35. Davey, R. J., Schroeder, S. L. M. & ter Horst, J. H. Nucleation of organic crystals a molecular perspective. *Angew. Chem. Int. Ed. Engl.* **52,** 2166–79 (2013).
36. Vehkamäki, H. *Classical nucleation theory in multicomponent systems*. *Classical Nucleation Theory in Multicomponent Systems* (Springer-Berlin, 2006).
37. Kashchiev, D. *Nucleation: Basic Theory with Applications*. (Butterworth-Heinemann, Oxford, 2000).
38. Mersmann, A. *Crystallization Technology Handbook*. (Marcel Dekker, Inc. New York, 2001).
39. Sullivan, R. a. *et al.* Revealing the roles of desolvation and molecular self-assembly in crystal nucleation from solution: Benzoic and p - aminobenzoic acids. *Cryst. Growth Des.* **14,** 2689–2696 (2014).
40. Kashchiev, D. & van Rosmalen, G. M. Review: Nucleation in solutions revisited. *Cryst. Res. Technol.* **38,** 555–574 (2003).
41. García-Ruiz, J. M. Nucleation of protein crystals. *J. Struct. Biol.* **142,** 22–31 (2003).
42. Mullin, J. W. Influence of mechanical agitation on the nucleation of some aqueous salt solutions. *Nat. Publ. Gr.* **195,** 35–38 (1962).
43. Galkin, O. & Vekilov, P. G. Direct Determination of the Nucleation Rates of Protein Crystals. *J. Phys. Chem. B* **103,** 10965–10971 (1999).
44. Lee, A. Y., Lee, I. S., Dette, S. S., Boerner, J. & Myerson, A. S. Crystallization on confined engineered surfaces: a method to control crystal size and generate different polymorphs. *J. Am. Chem. Soc.* **127,** 14982–14983 (2005).
45. Keller, D. M., Massey, R. E. & Hileman Jr., O. E. Studies on nucleation phenomena occurring in aqueous solutions supersaturated with calcium sulfate. III. The cation:anion ratio. *Can. J. Chem.* **56,** 831–838 (1978).
46. Dombrowski, R. D., Litster, J. D., Wagner, N. J. & He, Y. Crystallization of alpha-lactose monohydrate in a drop-based microfluidic crystallizer. *Chem. Eng. Sci.* **62,** 4802–4810 (2007).
47. Teychené, S. & Biscans, B. Crystal nucleation in a droplet based

microfluidic crystallizer. *Chem. Eng. Sci.* **77,** 242–248 (2012).

48. Laval, P., Salmon, J. B. & Joanicot, M. A microfluidic device for investigating crystal nucleation kinetics. *J. Cryst. Growth* **303,** 622–628 (2007).

49. Revalor, E. *et al.* Usual and unusual crystallization from solution. *J. Cryst. Growth* **312,** 939–946 (2010).

50. Kulkarni, S. A., Kadam, S. S., Meekes, H., Stankiewicz, A. I. & ter Horst, J. H. Crystal Nucleation Kinetics from Induction Times and Metastable Zone Widths. *Cryst. Growth Des.* **13,** 2435–2440 (2013).

51. Kadam, S. S. *et al.* A new view on the metastable zone width during cooling crystallization. *Chem. Eng. Sci.* **72,** 10–19 (2012).

52. Goh, L. *et al.* A Stochastic Model for Nucleation Kinetics Determination in Droplet-Based Microfluidic Systems. *Cryst. Growth Des.* **10,** 2515–2521 (2010).

53. Ramkrishna, D. *Population Balances - Theory and Applications to Particulate Systems in Engineering*. (Academic Press, London, 2000).

54. Toschev, S., Milchev, a & Stoyanov, S. On some probabilistic aspects of the nucleation process. *J. Cryst. Growth* **123,** 123–127 (1972).

55. Jiang, S. & ter Horst, J. H. Crystal Nucleation Rates from Probability Distributions of Induction Times. *Cryst. Growth Des.* **11,** 256–261 (2011).

56. Jiang, S. PhD Thesis - Crystallization Kinetics in Polymorphic Organic Compounds. Delft Univeristy of Technology. (Delft Univeristy of Technology, 2009).

57. Ildefonso, M. *et al.* Nucleation and polymorphism explored via an easy-to-use microfluidic tool. *J. Cryst. Growth* **342,** 9–12 (2012).

58. Hammadi, Z. *et al.* Small-volume nucleation. *Comptes Rendus Phys.* **14,** 192–198 (2013).

59. Randolph, A. D. & Larson, M. A. *Theory of Particulate Processes*. (Academic Press, London, 1988).

60. Mersmann, a., Braun, B. & Löffelmann, M. Prediction of crystallization coefficients of the population balance. *Chem. Eng. Sci.* **57,** 4267–4275 (2002).

61. Narducci, O., Jones, A. G. & Kougoulos, E. An Assessment of the Use of Ultrasound in the Particle Engineering of Micrometer-Scale Adipic Acid Crystals. *Cryst. Growth Org. Mater.* **11,** 1742–1749 (2011).

62. Narducci, O. & Jones, A. Seeding in Situ the Cooling Crystallization of Adipic Acid using Ultrasound. *Cryst. Growth Des.* **12,** 1727–1735 (2012).

63. Zarkadas, D. M. & Sirkar, K. K. Cooling Crystallization of Paracetamol in Hollow Fiber Devices. *Ind. Eng. Chem. Res.* **46,** 2928–2935 (2007).

64. Li, D. *Encyclopedia of Microfluidics and Nanofluidics*. (Springer, 2008).

65. Hartman, R. L. Managing Solids in Microreactors for the Upstream

Continuous Processing of Fine Chemicals. *Org. Process Res. Dev.* **16,** 870–887 (2012).

66. W. B. Russel, D. A. S. & W. R. S. *Colloidal dispersions*. (Cambridge University Press, Cambridge, 1989).
67. Wyss, H. M., Blair, D. L., Morris, J. F., Stone, H. a. & Weitz, D. a. Mechanism for clogging of microchannels. *Phys. Rev. E - Stat. Nonlinear, Soft Matter Phys.* **74,** 1–4 (2006).
68. Derksen, J. J. & Eskin, D. Potential of Microchannel Flow for Agglomerate Breakage. *Ind. Eng. Chem. Res.* **49,** 10633–10640 (2010).
69. Pamme, N. Continuous flow separations in microfluidic devices. *Lab Chip* **7,** 1644–1659 (2007).
70. Brunsteiner, M., Jones, A. G., Pratola, F., Price, S. L. & Simons, S. J. R. Toward a Molecular Understanding of Crystal Agglomeration. *Cryst. Growth Des.* **5,** 3–16 (2005).
71. Thorsen, T., Roberts, R. W., Arnold, F. H. & Quake, S. R. Dynamic Pattern Formation in a Vesicle-Generating Microfluidic Device. *Phys. Rev. Lett.* **86,** 4163–4166 (2001).
72. Anna, S. L., Bontoux, N. & Stone, H. a. Formation of dispersions using ‘flow focusing’ in microchannels. *Appl. Phys. Lett.* **82,** 364–366 (2003).
73. Poe, S. L., Cummings, M. a, Haaf, M. P. & McQuade, D. T. Solving the clogging problem: precipitate-forming reactions in flow. *Angew. Chem. Int. Ed. Engl.* **45,** 1544–8 (2006).
74. Tice, J. D., Song, H., Lyon, A. D. & Ismagilov, R. F. Formation of Droplets and Mixing in Multiphase Microfluidics at Low Values of the Reynolds and the Capillary Numbers. *Langmuir* **19,** 9127–9133 (2003).
75. Garstecki, P., Fuerstman, M. J., Stone, H. a & Whitesides, G. M. Formation of droplets and bubbles in a microfluidic T-junction-scaling and mechanism of break-up. *Lab Chip* **6,** 437–46 (2006).
76. Bretherton, F. P. The motion of long bubbles in tubes. *J. Fluid Mech.* **10,** 166 (1961).
77. Baroud, C. N., Gallaire, F. & Dangla, R. Dynamics of microfluidic droplets. *Lab Chip* **10,** 2032–2045 (2010).
78. Dreyfus, R., Tabeling, P. & Willaime, H. Ordered and Disordered Patterns in Two-Phase Flows in Microchannels. *Phys. Rev. Lett.* **90,** 144505 (2003).
79. Xu, J. H., Li, S. W., Tan, J., Wang, Y. J. & Luo, G. S. Controllable preparation of monodisperse O/W and W/O emulsions in the same microfluidic device. *Langmuir* **22,** 7943–7946 (2006).
80. Xu, J. H., Li, S. W., Tan, J., Wang, Y. J. & Luo, G. S. Preparation of Highly Monodisperse Droplet in a T-Junction Microfluidic Device. **52,** 3005–3010 (2006).
81. Cristini, V. & Tan, Y.-C. Theory and numerical simulation of droplet

dynamics in complex flows-a review. *Lab Chip* **4,** 257–64 (2004).

82. Kashid, M. N. *et al.* Internal circulation within the liquid slugs of a liquid-liquid slug-flow capillary microreactor. *Ind. Eng. Chem. Res.* **44,** 5003–5010 (2005).

83. Urs A. Peuker, Ulrich Hoffmann, Ulrich Wietelmann, Stefan Bandelin, R. J. *Sonochemistry*. *Ullmann's Encyclopedia of Industrial Chemistry* (Wiley-VCH Verlag GmbH & Co, 2006).

84. Bang, J. H. & Suslick, K. S. Applications of Ultrasound to the Synthesis of Nanostructured Materials. *Adv. Mater.* **22,** 1039–1059 (2010).

85. McCausland, L. J., Cains, P. W. & Martin, P. D. Use the Power of Sonocrystallization for Improved Properties. *Chem. Eng. Prog.* 56–61 (2001).

86. Louisnard, O. & González-García, J. in *Ultrasound Technologies for Food and Bioprocessing* (Springer, 2011).

87. Noltingk, B. E. Cavitation Produced by Ultrasonics: Theoretical Conditions for the Onset of Cavitation. *Proc. Phys. Soc. Sect. B* **64,** 1032–1038 (1951).

88. Suslick, S. & Fang, M. Acoustic cavitation and its chemical consequences. *Phil. Trans. R. Soc. Lond. A* **357,** 335–353 (1999).

89. Mason, T. J. Sonochemistry and sonoprocessing: The link, the trends and (probably) the future. *Ultrason. Sonochem.* **10,** 175–179 (2003).

90. Boluriaan, S. & Morris, P. J. Acoustic streaming: from Rayleigh to today. *Int. J. Aeroacoustics* **2,** 255–292 (2009).

91. Mason T. J. *Sonochemistry*. (Oxford University Press, 1999).

92. Margulis, M. A. & Margulis, I. M. Calorimetric method for measurement of acoustic power absorbed in a volume of a liquid. *Ultrason. Sonochem.* **10,** 343–345 (2003).

93. Sleutel, M., Lutsko, J., Van Driessche, A. E. S., Durán-Olivencia, M. a. & Maes, D. Observing classical nucleation theory at work by monitoring phase transitions with molecular precision. *Nat. Commun.* **5,** 5598 (2014).

94. Wang, G. C., Wang, Q., Li, S. L., Ai, X. G. & Fan, C. G. Evidence of Multi-step Nucleation Leading to Various Crystallization Pathways from an Fe-O-Al Melt. *Sci. Rep.* **4,** 5082 (2014).

95. G. W. Greenwood, A. L. Greer, Kelton, D. M. H. and K. F. Nulceation control. *Phil. Trans. R. Soc. Lond. A* **3,** 405–407 (2003).

96. Vekilov, P. G. Nucleation. *Cryst. Growth Des.* **10,** 5007–5019 (2010).

97. Salvalaglio, M., Perego, C., Giberti, F., Mazzotti, M. & Parrinello, M. Molecular-dynamics simulations of urea nucleation from aqueous solution. *Proc. Natl. Acad. Sci.* **112,** E6–E14 (2015).

98. Wohlgemuth, K., Kordylla, A., Ruether, F. & Schembecker, G. Experimental study of the effect of bubbles on nucleation during batch

cooling crystallization. *Chem. Eng. Sci.* **64,** 4155–4163 (2009).

99. Li, H., Li H. R., Guo, Z. & Liu, Y. The application of power ultrasound to reaction crystallization. *Ultrason. Sonochem.* **13,** 359–363 (2006).

100. Kurotani M, Miyasaka E, Ebihara S, H. I. Effect of ultrasonic irradiation on the behavior of primary nucleation of amino acids in supersaturated solutions. *J. Cryst. Growth* **311,** 2714–2721 (2009).

101. Dodds, J. *et al.* The effect of ultrasound on crystallisation-precipitation processes: Some examples and a new segregation model. *Part. Part. Syst. Charact.* **24,** 18–28 (2007).

102. Grossier, R., Louisnard, O. & Vargas, Y. Mixture segregation by an inertial cavitation bubble. *Ultrason. Sonochem.* **14,** 431–7 (2007).

103. Harzali, H., Baillon, F., Louisnard, O., Espitalier, F. & Mgaidi, a. Experimental study of sono-crystallisation of ZnSO4·7H2O, and interpretation by the segregation theory. *Ultrason. Sonochem.* **18,** 1097–106 (2011).

104. Hickling, R. Nucleation of Freezing by Cavity Collapse and its Relation to Cavitation Damage. *Nature* **4987,** (1965).

105. Chow, R., Blindt, R., Chivers, R. & Povey, M. The sonocrystallisation of ice in sucrose solutions: primary and secondary nucleation. *Ultrasonics* **41,** 595–604 (2003).

106. Chow, R., Blindt, R., Chivers, R. & Povey, M. A study on the primary and secondary nucleation of ice by power ultrasound. *Ultrasonics* **43,** 227–30 (2005).

107. Chow, R., Blindt, R., Kamp, A., Grocutt, P. & Chivers, R. The microscopic visualisation of the sonocrystallisation of ice using a novel ultrasonic cold stage. *Ultrason. Sonochem.* **11,** 245–50 (2004).

108. Arakelyan, V. Effect of ultrasound on crystal growth from melt and solution. *Acta Phys. Hungarica* **61,** 185–187 (1987).

109. Arakelyan, V. Periodic structures in crystals grown in ultrasonic field. *J. Cryst. Growth* **85,** 357–362 (1987).

110. Guo, Z., Jones, A. G., Li, N. & Germana, S. High-speed observation of the effects of ultrasound on liquid mixing and agglomerated crystal breakage processes. *Powder Technol.* **171,** 146–153 (2007).

111. Zeiger, B. W. & Suslick, K. S. Sonofragmentation of molecular crystals. *J. Am. Chem. Soc.* **133,** 14530–3 (2011).

112. Castro, F. *et al.* Continuous-flow precipitation of hydroxyapatite in ultrasonic microsystems. **216,** 979–987 (2013).

113. Gracin, S., Uusi-Penttilä, M. & Rasmuson, A. C. Influence of ultrasound on the nucleation of polymorphs of p-aminobenzoic acid. *Cryst. Growth Des.* **5,** 1787–1794 (2005).

114. Gracin, S. & Rasmuson, A. C. Polymorphism and Crystallization of p-Aminobenzoic Acid. *Cryst. Growth Des.* **5,** 1013–102 (2004).

115. Louhi-Kultanen, M., Karjalainen M, J, R., M, H. & J., K. Crystallization of glycine with ultrasound. *Int. J. Pharm* **320,** 23–29 (2006).

116. Clydesdale, G. *et al.* A Molecular Modeling Study of the Crystal Morphology of Adipic Acid and Its Habit Modification by Homologous Impurities. *Cryst. Growth Des.* **5,** 2151–2163 (2005).

117. Stojanovic, Z. Determination of particle size distributions by laser diffraction. *Tech. New Mater.* **21,** 11–20 (2012).

118. Volpatti, L. R. & Yetisen, A. K. Commercialization of microfluidic devices. *Trends Biotechnol.* **32,** 347–350 (2014).

119. Dore, V., Tsaoulidis, D. & Angeli, P. Mixing patterns in water plugs during water/ionic liquid segmented flow in microchannels. *Chem. Eng. Sci.* **80,** 334–341 (2012).

120. Liu, H., Vandu, C. O. & Krishna, R. Hydrodynamics of taylor flow in vertical capillaries: Flow regimes, bubble rise velocity, liquid slug length, and pressure drop. *Ind. Eng. Chem. Res.* **44,** 4884–4897 (2005).

121. Comsol 4.3. Comsol Multiphysics User's Guide. *Comsol Modul.* 1–1292 (2012).

122. Narducci O. PhD Thesis - Particle engineering via sonocrystallization: the aqueous adipic acid system. *Univerity College London - Department of Chemical Engineering* (College London, 2012).

123. Dummann, G. *et al.* The capillary-microreactor: a new reactor concept for the intensification of heat and mass transfer in liquid–liquid reactions. *Catal. Today* **79–80,** 433–439 (2003).

124. Thulasidas, T. C., Abraham, M. A. & Cerro, R. L. Bubble-train flow in capillaries of circular and square cross section. *Chem. Eng. Sci.* **50,** 183–199 (1995).

125. van Baten, J. M. & Krishna, R. CFD simulations of mass transfer from Taylor bubbles rising in circular capillaries. *Chem. Eng. Sci.* **59,** 2535–2545 (2004).

126. Kashchiev, D., Verdoes, D. & van Rosmalen, G. M. Induction time and metastability limit in new phase formation. *J. Cryst. Growth* **110,** 373–380 (1991).

127. Eder, R. J. P. *et al.* Continuous Sonocrystallization of Acetylsalicylic Acid (ASA): Control of Crystal Size. *Cryst. Growth Des.* **12,** 4733–4738 (2012).

128. Cucheval, A. & Chow, R. C. Y. A study on the emulsification of oil by power ultrasound. *Ultrason. Sonochem.* **15,** 916–20 (2008).

129. Ashokkumar, M. *et al.* Spatial distribution of acoustic cavitation bubbles at different ultrasound frequencies. *Chemphyschem* **11,** 1680–4 (2010).

130. Henglein, A., Ulrich, R. & Lilie, J. Luminescence and Chemical Action by Pulsed Ultrasound. *J. Am. Chem. Soc.* **111,** 1974–1979 (1989).

131. Tandiono *et al.* Sonochemistry and sonoluminescence in microfluidics.

Proc. Natl. Acad. Sci. U. S. A. **108,** 5996–5998 (2011).

132. Fernandez Rivas, D. *et al.* Sonoluminescence and sonochemiluminescence from a microreactor. *Ultrason. Sonochem.* **19,** 1252–1259 (2012).

133. Rooze, J., Rebrov, E. V, Schouten, J. C. & Keurentjes, J. T. F. Effect of resonance frequency, power input, and saturation gas type on the oxidation efficiency of an ultrasound horn. *Ultrason. Sonochem.* **18,** 209–15 (2011).

134. Jamshidi, R., Pohl, B., Peuker, U. a. & Brenner, G. Numerical investigation of sonochemical reactors considering the effect of inhomogeneous bubble clouds on ultrasonic wave propagation. *Chem. Eng. J.* **189–190,** 364–375 (2012).

135. Moussatov, A., Granger, C. & Dubus, B. Cone-like bubble formation in ultrasonic cavitation field. *Ultrason. Sonochem.* **10,** 191–195 (2003).

136. Ozcelik, A. *et al.* An acoustofluidic micromixer via bubble inception and cavitation from microchannel sidewalls. *Anal. Chem.* **86,** 5083–5088 (2014).

137. Arora, M., Ohl, C. D. & Mørch, K. A. Cavitation inception on microparticles: A self-propelled particle accelerator. *Phys. Rev. Lett.* **92,** 174501–1 (2004).

138. Hessel, V., Löwe, H. & Schönfeld, F. Micromixers - A review on passive and active mixing principles. *Chem. Eng. Sci.* **60,** 2479–2501 (2005).

139. Nguyen, N.-T. & Wu, Z. Micromixers - a review. *J. Micromechanics Microengineering* **15,** R1–R16 (2005).

140. Taylor, G. I. Deposition of a viscous fluid on a plane surface. *J. Fluid Mech.* **9,** 218 (1961).

141. Saxena, A. K. & Nigam, K. D. P. Coiled configuration for flow inversion and its effect on residence time distribution. *AIChE J.* **30,** 363–368 (1984).

142. Ni, X. *et al.* Mixing Through Oscillations and Pulsations - A Guide to Achieve Process Enhancement in the Chemical and Process Industries. *Trans IChemE* **81,** 373–383 (2003).

143. McDonough, J. R., Phan, A. N. & Harvey, A. P. Rapid process development using oscillatory baffled mesoreactors - A state of the art review. *Chem. Eng. J.* **265,** 110–121 (2015).

144. Zheng, M. & Mackley, M. The axial dispersion performance of an oscillatory flow meso-reactor with relevance to continuous flow operation. *Chem. Eng. Sci.* **63,** 1788–1799 (2008).

145. Dickens, A. W., Mackley, M. R. & Williams, H. R. Experimental Residence Time Distribution Measurments For Unsteady Flow In Baffled Tubes. *Chem. Eng. Sci.* **44,** 1471–1479 (1989).

146. Olayiwola, B. O., Schaldach, G. & Walzel, P. Residence Time Distribution of Steady and Pulsed Flow in a Parallel-Plate Channel with

Staggered Fins. *Chem. Eng. Technol.* **34,** 937–945 (2011).

147. Brunold, C. R., Hunns, J. C. B., MACKLEY, M. R. & THOMPSON, J. W. Experimental observations on flow patterns and energy losses for oscillatory flow in ducts containing sharp edges. *Chem. Eng. Sci.* **44,** 1227–1244 (1989).
148. Levenspiel, O. *Chemical reaction engineering*. (John Wiley & Sons, New York, 1999).
149. Ananthakrishnan, V., Gill, W. N. & Barduhn, A. J. Laminar dispersion in capillaries: Part I. Mathematical analysis. *AIChE J.* **11,** 1063–1072 (1965).
150. Aris, R. On the Dispersion of a Solute in a Fluid Flowing through a Tube. *Proc. R. Soc. London Ser. A, Math. Phys. Sci.* **235,** 67–77 (1956).
151. Taylor, G. Dispersion of Soluble Matter in Solvent Flowing Slowly through a Tube. *Proc. R. Soc. London Ser. A, Math. Phys. Sci.* **219,** 186–203 (1953).
152. Sobey, I. J. The occurrence of separation in oscillatory flow. *J. Fluid Mech.* **134,** 247–257 (1983).
153. Sobey, I. J. Observation of Waves During Oscillatory Channel Flow. *J. Fluid Mech.* **151,** 395–426 (1984).
154. Aris, R. On the Dispersion of a Solute in Pulsating Flow Through a Tube. *Proc. R. Soc. A Math. Phys. Eng. Sci.* **259,** 370–376 (1960).
155. Chatwin, P. C. On the longitudinal dispersion of passive contaminant in oscillatory flows in tubes. *J. Fluid Mech.* **71,** 513–527 (1975).
156. Mukherjee, A. & Mazumder, B. S. Dispersion of contaminant in oscillatory flows. *Acta Mech.* **74,** 107–122 (1988).
157. Vedel, S. & Bruus, H. Transient Taylor–Aris dispersion for time-dependent flows in straight channels. *J. Fluid Mech.* **691,** 95–122 (2012).
158. Bošković, D. & Loebbecke, S. Modelling of the residence time distribution in micromixers. *Chem. Eng. J.* **135,** 138–146 (2007).
159. Trivedi, R. N. & Vasudeva, K. Axial dispersion in laminar flow in helical coils. *Chem. Eng. Sci.* **30,** 317–325 (1975).
160. Klutz, S., Kurt, S. K., Lobedann, M. & Kockmann, N. Narrow residence time distribution in tubular reactor concept for Reynolds number range of 10–100. *Chem. Eng. Res. Des.* **95,** 22–33 (2015).
161. McKay, Otterburn, M. S. & Sweeney, A. G. Surface mass transfer processes during colour removal from effluent using silica. *Water Res.* **15,** 327–331 (1981).
162. Logtenberg, H., Lopez-Martinez, M. J., Feringa, B. L., Browne, W. R. & Verpoorte, E. Multiple flow profiles for two-phase flow in single microfluidic channels through site-selective channel coating. *Lab Chip* **11,** 2030–2034 (2011).

Publications

- Rossi, D. et al. Adipic acid primary nucleation kinetics from probability distributions in droplet-based systems under stagnant and flow conditions. Cryst. Growth Des. 15, 1784 - 1791 (2015).

- Rossi, D. et al. Continuous-Flow sonocrystallization in droplet-based microfluidics. Cryst. Growth Des. 15, 5519 - 5529 (2015).

- Jamshidi R., Rossi, D. et al. Investigation of the effect of ultrasound parameters on continuous sonocrystallization in a millifluidic device. To be submitted to Cryst. Growth Des. 16, 4607- 4619 (2016).

- Rossi, D. et al. Adipic acid nucleation kinetics from probability distributions in drop-based systems. ISIC19 Toulouse. Conference Proceedings. (2014).

- Jamshidi R., Rossi, D. et al. Experimental and numerical investigation of continuous sonocrystallization of adipic acid in a straight milli channel. ECCE10 Nice. Conference Proceedings. (2015).

- Rossi, D. et al. Adipic acid primary nucleation kinetics from probability distributions in droplet-based systems under stagnant and flow conditions. BACG2016 Leeds. Conference Proceedings. (2016).

- Rossi, D. et al. Experimental characterization of axial dispersionin coiled flow inverters. ChERD. 120, 159-170 (2017).